A Subject-Specific Multiscale Model of Transcranial Magnetic Stimulation

Brian Daniel Goodwin
Marquette University

A SUBJECT-SPECIFIC MULTISCALE MODEL OF TRANSCRANIAL MAGNETIC STIMULATION

by

Brian D. Goodwin, B.S.

A Dissertation submitted to the Faculty of the Graduate School, Marquette University, in Partial Fulfillment of the Requirements for the Degree of Doctor of Philosophy

Milwaukee, Wisconsin

December 2014

ABSTRACT
A SUBJECT-SPECIFIC MULTISCALE MODEL OF TRANSCRANIAL MAGNETIC STIMULATION

Brian D. Goodwin, B.S.

Marquette University, 2014

Transcranial magnetic stimulation (TMS) is a neuromodulation technique used to treat a variety of neurological disorders. While many types of neuromodulation therapy are invasive, TMS is an attractive alternative because it is noninvasive and has a very strong safety record. However, clinical use of TMS has preceded a thorough scientific understanding: its mechanisms of action remain elusive, and the spatial extent of modulation is not well understood.

We created a subject-specific, multiscale computational model to gain insights into the physiological response during motor cortex TMS. Specifically, we developed an approach that integrates three main components: 1) a high-resolution anatomical MR image of the whole head with diffusion weighted MRI data; 2) a subject-specific, electromagnetic, non-homogeneous, anisotropic, finite element model of the whole head with a novel time-dependent solver; 3) a population of multicompartmental pyramidal cell neuron models. We validated the model predictions by comparing them to motor evoked potentials (MEPs) immediately following single-pulse TMS of the human motor cortex. This modeling approach contains several novel components, which in turn allowed us to gain greater insights into the interactions of TMS with the brain.

Using this approach we found that electric field magnitudes within gray matter and white matter vary substantially with coil orientation. Our results suggest that 1) without a time-dependent, subject-specific, non-homogeneous, anisotropic model, loci of stimulation cannot be accurately predicted; 2) loci of stimulation depend upon biophysical properties and morphologies of pyramidal cells in both gray and white matter relative to the induced electric field.

These results indicate that the extent of neuromodulation is more widespread than originally thought. Through medical imaging and computational modeling, we provide insights into the effects of TMS at a multiscale level, which would be unachievable by either method alone. Finally, our approach is amenable to clinical implementation. As a result, it could provide the means by which TMS parameters can be prescribed for treatment and a foundation for improving coil design.

ACKNOWLEDGMENTS

Brian D. Goodwin, B.S.

I would like to express my immense gratitude to my mentors and committee members Dr. Christopher Butson, Dr. Scott Beardsley, Dr. Manoj Raghavan, Dr. Thomas Prieto, and Dr. Brian Schmit for their invaluable guidance, wisdom, and support. I would like to thank Klaus Driesslein, Yagna Pathak, and Dr. Xuefeng Wei for their help, participation, and advice throughout my time at Marquette University.

I would like to offer most special thanks to the Shirk family for their prayers and to my friends at Word of Grace Bible Church whose prayers were equally felt. I thank my faithful friend Aaron Dan Lewis who, while working outside of my scientific field, volunteered to endure a most painful endeavor and read through this dissertation in its entirety.

None of this would be possible had my parents not provided the love, motivation, encouragement, and means to complete undergraduate work and graduate work. I thank them, Barry and Linda, for their sacrificial love and support through all these years.

Finally, I thank my wife for her love, sacrifice, support, and long-suffering attitude toward me as I completed this chapter in my life. I praise God for you, Melissa.

I praise my God and Savior, Jesus Christ who, through the word of His mouth, gave meaning and purpose to life, which makes life and labor worthwhile. Without His death and resurrection for my sins, I would be without hope in the midst of a world subjected to pain, war, and death.

PREFACE

The overall goal of this research is to better understand the nature of TMS and its interactions with neural elements in the cerebrum. This dissertation examines the effects of TMS at the interface between the brain and imposed magnetic fields through computational modeling and *in vivo* experiments. Studying the effects at this interface necessitates the use of time-dependent electromagnetic field modeling and nonlinear dynamic system modeling of neurons.

In this study, we applied magnetic resonance imaging (MRI), finite element methods, and computational neuroscience methods to quantify the immediate response of neural elements to TMS, with a focus on the response of pyramidal cells in motor cortex and adjacent regions. Pyramidal cells have been previously shown to be direct (and indirect) targets of TMS (Di Lazzaro et al., 2008).

Though TMS has been shown to be an effective therapeutic treatment, the physiological response both among and within subjects is highly variable (Di Lazzaro et al., 2013). In an attempt to uncover reasons for the variability during TMS, we measured the amplitude of the motor evoked potential (MEP) from muscle electromyography (EMG) of the first dorsal interosseous (FDI) elicited from stimulation of the hand-knob in motor cortex. The MEP is not a direct measure of the effects in the cortex but has been employed as a general quantification of motor neuron recruitment during stimulation of the hand-knob in M1 (Vaalto et al., 2010).

TABLE OF CONTENTS

LIST OF TABLES

LIST OF FIGURES

GLOSSARY

$\mathbf{A}$; A-field	Magnetic vector potential
$A_{\nu<\bar{\nu}}$	Surface area of cortex having a threshold stimulus below $\bar{\nu}$
AP	Anterior-to-posterior (electric current flow)
$\mathbf{B}$; B-field	Magnetic field
BOLD	Blood-oxygen-level dependence
CSF	Cerebrospinal fluid
CNS	Central nervous system
DBS	Deep brain stimulation
DFT	Discrete Fourier transform
dlPFC	Dorsolateral prefrontal cortex
DTI	Diffusion tensor image
DWI	Diffusion-weighted MRI
$\mathbf{E}$; E-field	Electric field
ECS	Electrical cortical stimulation (by implanted electrodes)
EEG	Electroencephalography
EMG	Electromyography
EMF	Electromotive force
$\mathcal{F}(\boldsymbol{\nu}, \bar{\nu})$	Model prediction of motor response robustness
FA	Fractional anisotropy
FDA	Food and Drug Administration
FDI	First dorsal interosseous
FEM	Finite element model
FFT	Fast Fourier transform
fMRI	Functional magnetic resonance imaging
GM	Gray matter
HPC	High-performance computing
M1	Primary motor cortex
MEG	Magnetoencephalography
MEP	Motor evoked potential
MRI	Magnetic resonance imaging
NMR	Nuclear magnetic resonance
$\boldsymbol{\nu}$	Threshold stimulus vector array of all neurons within a population
ν	Threshold stimulus of a neuron
$\bar{\nu}$	Cut-off threshold for activation
PA	Posterior-to-anterior (electric current flow)
PD	Parkinson's disease
PET	Positron emission tomography
ppTMS	Paired-pulse TMS
RMT	Resting motor threshold
rTMS	Repetitive TMS
SPECT	Single photon emission computed tomography
tDCS	Transcranial direct current stimulation
TES	Transcranial electrical stimulation
TMS	Transcranial magnetic stimulation
WM	White matter

HYPOTHESIS AND SPECIFIC AIMS

The *objective* of this doctoral dissertation is to use multiscale computational modeling to quantify the degree, type, and location of neuromodulation during TMS. The *central hypothesis* is that the modulatory effects of TMS depend on the stimulation waveform and amplitude as well as the placement of the TMS coil relative to excitable neural elements in cortex. The *rationale* for this approach is that information from computational models can inform physiological studies of TMS and provide insights that would be difficult to obtain using either method alone.

The general assumption is that activation from TMS can be estimated by action potential initiation in pyramidal cells in the cortex.

Specific Aims

Specific Aim 1: Create a multiscale, biophysically-based computational model of TMS

Specific Aim 1 includes the definition, description, and model of the physical and biophysical parameters at the interface of the neuron and a magnetic stimulus. Two main components were integrated to make up this model: 1) a time-dependent characterization of the electromagnetic sources from the TMS coil and 2) a detailed, multicompartmental pyramidal cell neuron model with Hodgkin-Huxley ion channel kinetics. *We hypothesized that a multiscale computational model with biophysically based properties can simulate the neural response to TMS.*

Specific Aim 2: Quantify the modulatory effects of TMS on the hand-knob of the motor cortex

Using the model from Specific Aim 1, Specific Aim 2 attempts to 1) quantitatively describe the response of pyramidal cells surrounding the hand-knob area of the motor

cortex to the induced electric field determined by TMS parameters and 2) quantify the sensitivity of the neural response to TMS coil orientation. *We hypothesized that the neural response to TMS is a function of the time-dependent electric field characteristics induced in the brain relative to the orientation of neural elements in cortex and white matter.*

Specific Aim 3: Quantify physiological response to motor cortex TMS

Specific Aim 3 corroborates the model from Specific Aims 1 and 2 by performing TMS over the motor cortex of a healthy subject while recording the physiological response. We applied the computational model to quantify the activation in the hand-knob of M1 and compared this quantity to physiological responses. *We hypothesized that a subject-specific multiscale model can quantify the physiological response to TMS.*

SYNOPSIS

The order of the chapters describes the chronological progression of the research and the development of the central hypothesis. This dissertation work was funded by the Clinical & Translational Science Institute of Southeast Wisconsin; Department of Neurology, Medical College of Wisconsin; Department of Biomedical Engineering, Marquette University via Falk Foundation grant: “Collaborative Research Integrating Neuroimaging and Neurorehabilitation.”

Chapter 1 describes the effect of magnetic stimulation on neural elements. We developed a biophysically based neuron model to assess the neural response to E-fields produced by TMS by applying electromagnetism theory and Ampere’s law of charge conservation. Using this model and a novel time-dependent solver, we demonstrated that the transient characteristics of the induced E-field could be computed. **Such a model is capable of simulating the neural response to a time-varying magnetic stimulus.**

Chapter 2 builds upon the model developed in the study described in Chapter 1 by incorporating a subject-specific finite element model (FEM) to assess the effect of rotating the TMS coil on the induced E-field. In addition, the immediate response of biophysically based models of pyramidal cells and their axons was simulated using a novel multiscale approach. Changing the coil orientation resulted in distinct changes in the induced E-field and the response of neural elements in cortex. I found that **the neural response depends upon the time-dependent electric field characteristics induced in the brain relative to the orientation of neural elements.**

The subject-specific multiscale approach is further developed in Chapter 3 with the addition of anisotropic material properties and formation of pyramidal cell axons

derived from a diffusion tensor image volume. Changing the coil orientation significantly influenced the depth of neural activation over the targeted area of cortex. Our subject-specific multiscale model was corroborated by the amplitude of the motor evoked potential (MEP) elicited from TMS of the human motor cortex. The MEP amplitude from TMS was measured using EMG on the FDI muscle in the hand. The response variability from TMS can be explained by minor changes in stimulation parameters and by variations in the transmembrane potential of excitable elements in the cortex during stimulation. In support of the hypothesis, the findings suggested that **a subject-specific multiscale model is capable of quantifying the physiological response to TMS.**

BACKGROUND AND SIGNIFICANCE

Historical Perspective in Neuromodulation

Neuromodulation, a subfield of biomedicine, is formally defined as "technology impacting on the neural interface" (Krames et al., 2009) with the intention to change the course of recurrent brain activity by electrical, chemical, or mechanical stimulation to achieve improvement in neurological function and, thus, quality of life. Its methodologies are employed in a wide range of disciplines from psychiatry to kinesiology, and it incorporates the use of both implantable and non-implantable devices. Neuromodulation research has two primary objectives: 1) scientific investigation of brain function and 2) discovery of medicine or therapy for treatment (normally long-term) of neurological conditions. Techniques in neuromodulation have advanced to provide innovative means to interface with the brain via biomedical instrumentation, which has been shown to be especially relevant in studies pertaining to functional brain mapping. With technological advancements, neuromodulation research has gained momentum through demonstrations of improved quality of life for individuals suffering from neurological diseases or psychiatric illnesses.

Today, neuromodulation almost always refers to innovations in electrical[1] brain stimulation. The beginning of neuromodulation dates to Ancient Egypt where the common torpedo fish had inadvertently shocked a freed slave of Emperor Tiberius, who had subsequently experienced relief from painful gout (Krames et al., 2009; Stillings, 1971).

---

[1] Unless otherwise mentioned, electrical stimulation refers to the stimulation of neural elements through the use of macro electrodes.

Present day advancements in neuromodulation are derived from an arguably unsophisticated history. Therapeutic neuromodulation has progressed from resection surgeries for psychiatric (e.g. lobotomy) or neurological (e.g. pallidotomy) purposes to less invasive and lower risk options through brain stimulation. Current neuromodulation techniques are based on principles originating from patient outcomes following neural tissue resection. In fact, the original hypothesis about the mechanisms of modern deep brain stimulation (DBS)[2] alluded to the pallidotomy purpose through the notion that DBS acts as a functional lesion since its clinical responses were indistinguishable from those from the pallidotomy (Krames et al., 2009, p. 531).

Most scientific theories and validation experiments in neuromodulation result from new developments in methodological tools that drive research. The evolution of tools for electrophysiology has been integral to theory and hypothesis formulation in neuromodulation since Guillaume Duchenne de Boulogne (1806-75) used two electrodes on wet skin to stimulate muscle (Walsh & Pascual-Leone, 2005).

Neuromodulation and Magnetism

Effective tools for magnetic brain stimulation have come on the historical scene fairly recently, and have opened the door to new developments in our understanding of the nervous system. Magnetism was employed earlier in healthcare history than electricity. During the Middle Ages, magnets were believed to possess outlandish medicinal powers[3]. Magnetism for neuromodulation gained popularity much later in history, primarily through the contributions of Michael Faraday.

---

[2] DBS is an effective mode of neuromodulation whereby an electrode array is surgically implanted into the brain near deep structures such as the subthalamic nucleus with the intent to electrically stimulate nearby neural elements via current injection (Recoskie et al., 2009).

[3] Even today, those looking for the “silver bullet” will turn to magnetism to improve health.

The science of magnetic induction began with Michael Faraday (1791-1867), who was the first to generate a magnetic field from electric current flowing through a metal coil. Scientists were unable to produce an observable response by stimulating neural tissue with magnetic induction until the beginning of the 20th century. Arséne d'Arsonval reported "phosphenes" and vertigo when an electric current of 30A at 42Hz flows through a large metal coil surrounding the head (Walsh & Pascual-Leone, 2005). Magnetic neuromodulation research consisted of eliciting visual sensations or phosphenes until Anthony Barker constructed a refined magnetic stimulation coil in 1985.

Before Barker, painless noninvasive neuromodulation of the brain was unachievable in a safe and robust way. The closest antecedent to Barker's achievement was in 1980 when (Merton & Morton, 1980) invented transcranial electrical stimulation (TES), which delivers a (painful) high-voltage electric shock to the scalp to activate neurons in the brain (Hallett, 2000). Barker's transcranial magnetic stimulation (TMS)[4] was painless and capable of eliciting responses similar to those from TES. By 1987, TMS had already been proposed as a treatment for depression (Bickford et al., 1987; Krames et al., 2009).

Modern well-established modes of long-term neuromodulation for chronic illnesses are normally highly invasive. Compared to TMS, invasive devices have been shown to effectively elicit reproducible physiological responses. DBS for Parkinson's disease (PD) is perhaps the most well-known and reputable application of invasive neuromodulation. The DBS device is a biocompatible electrode array that is surgically implanted into deep brain structures. Pulses of electric current are continuously

[4] Though several TMS paradigms exist, TMS is in reference to a particular mode of neuromodulation, namely, stimulation of the nervous system via magnetic induction.

delivered and recovered from its electrodes, which impact the activity of nuclei affected by PD. Its effects almost completely alleviate Parkinsonian symptoms when the electrode is placed near the subthalamic nucleus. Similarly, the cortical electrode array targets specific areas in the cortex and also modulates neural activity through current injection from its electrodes. Cortical electrodes are surgically implanted between the skull and cortex to achieve stimulation of neural elements in a desired area. Both electrical cortical stimulation (ECS)[5] and DBS require the constant delivery of current impulses to achieve a therapeutic benefit.

TMS is distinct from invasive electrical modes of brain stimulation in terms of operation, mechanisms, spread of stimulation, and lasting effects. On the other hand, like all modes of neuromodulation, the stimulation parameter space (waveform shape, amplitude, frequency, etc.) for TMS is infinite. As a result, stimulation parameters are empirically determined through physiological observations. TMS has been employed as a neurophysiological tool, and thousands of studies over the last 20 years have demonstrated its physiological effects and its potential for improving our understanding of the nervous system (Di Lazzaro et al., 2008; Fregni et al., 2005; Hallett, 2000; Hoogendam et al., 2010; Sampson et al., 2006; Williams et al., 2009). However, the use of TMS as a therapeutic or neurophysiological tool has preceded a thorough scientific understanding of its effects. Its growth in popularity since its invention in 1985 (Barker et al., 1985) can be attributed to it being safe (Rossi et al., 2009), noninvasive, outpatient, and effective for a range of neurological conditions including depression (Bortolomasi et al., 2007; O'Reardon et al., 2007), epilepsy (Nitsche & Paulus, 2009; Säisänen et al., 2010), and tinnitus (Kleinjung et al., 2005; Langguth et al., 2008). Additionally, TMS has

[5] ECS is carried out through implanted electrodes between the skull and cortex. The implanted device contains one or many electrodes in an array. For therapeutic purposes, typically two electrodes (an anode and cathode) are implanted over a specific area of the cortex.

the potential for use as a screening tool to provide a measure of patient susceptibility to chronic electrode implant.

During TMS, a coil of wire encased in a wand is held to the head and energized by the discharge of a large capacitor, causing a current flow in its windings, which in turn produces a magnetic field (**B**; B-field) normal to the plane of the coil. Induced magnetic fields are not deflected or attenuated by biological tissue and therefore penetrate the skull and permeate the brain, inducing electric currents according to the principle of induction. The purpose of TMS is to generate suprathreshold electric fields that cause stimulation to neurons in the brain. The magnitude of the induced electric field (**E**; E-field) is proportional to the rate of change of **B**.

$$\nabla \times \mathbf{E} = \frac{d\mathbf{B}}{dt} \qquad \text{(Eq. 1)}$$

The resulting current densities can have immediate effects on nearby neural elements similar to the way currents are applied directly to the brain using electrodes. Though distinct from electrical stimulation, TMS shows promise in its ability to deliver therapeutic treatment similar to that of ECS. Notwithstanding, the effects of TMS are highly variable across subject populations as in other modes of (electrical) neuromodulation.

Though promising, TMS lacks repeatability both within a single subject and throughout subject populations. Compared to modern forms of invasive neuromodulation, the electric currents induced from TMS have a considerably greater expanse, and it is currently impossible to accurately predict the extent of modulation within the brain. The advantage of TMS being noninvasive is somewhat offset by the variability in physiological response. This variability is partially attributed to its inherent need to be physically placed over the scalp. Consequently, TMS has at least 6 degrees

of freedom (rotation, pitch, yaw, and location in 3D space). The difficulty in constraining these degrees of freedom is a major contributing factor to the observed variability in physiological response across subjects. Furthermore, the waveform shape, amplitude, and frequency are additional parameters that require individual constraint.

TMS 101

TMS requires a number of components to work properly and a number of add-ons to work effectively. Beyond the hardware, understanding its functionality and physical interactions with brain can be a daunting task, and the literature often contains conflicting viewpoints especially in regard to the reliability of TMS, “optimal” parameters, and even the conventions in determining values for these parameters.

Coil Design

Barker’s lab developed the first modern TMS coil in 1985, and its geometry was purely circular. Coils of circular geometry have a high efficiency and so were an obvious choice. The induced electric currents follow lines concentric to the geometry of the windings within the coil. Sharp corners in coil geometry result in decreased current densities, and the electric currents, nonetheless, turn in a gradual manner near the corners of coil.

The circular coil is typically referred to as a “high-powered” coil, and it is still utilized today. Normal Magstim[6] circular coils for human use are 90 mm in diameter with nine copper windings. At the expense of its power, the circular coil generates high electric currents over a widespread area of the brain. To lessen such widespread

[6] (Trade Mark) See http://www.magstim.com/.

stimulation, most studies employ a figure-8 coil[7], which consists of two coils that are placed adjacent and coplanar to one another with nine windings each. The coplanar coils carry current in opposing directions so that the maximum induced current is directly underneath the center of the coil in the direction of the wand handle.

The focal stimulation offered by the figure-8 coil is appealing and as a result, it is used ubiquitously in both research and clinical environments. A great deal of experimental research has been invested in developing coils that target focal areas of the brain and deeper brain structures (Hernandez-Garcia et al., 2010; Y. Roth et al., 2007). For example, customized deep brain "H-coils" have been used for research purposes, and studies are being performed to assess their efficacy in stimulating deeper structures (Y. Roth et al., 2014). Additionally, a new coil has been designed to remove the orientation dependencies of the figure-8 coil by inducing "rotating" electric fields in which the direction of the induced electric field is rotated between 0º and 270º throughout the duration of the stimulus (Rotem et al., 2014). Interestingly, coil design for clinical use has not significantly changed since the invention of TMS. Still, the figure-8 coil is the most widely used coil in both research and clinical environments.

Coil inductance is a product of coil geometry and has little impact on the stimulating electric field. The shape of the coil is designed to minimize inductance with the goal of preventing the coil from overheating. Inductance effects are negligible in terms of electromotive forces that oppose current flow, but inductance plays a role in thermal energy generation and efficiency. As a result, most present day TMS systems have integrated air- (or water-) cooling systems. The inductance (L) of a TMS coil having

[7] This name originates from its shape, which has the form of a "figure-of-8". Its shape naturally causes more focal stimulation compared to the circular coil.

a coil radius of r_c, wire radius of r_w, and N number of turns can be calculated by (B. J. Roth & Basser, 1990):

$$L = \mu_0 r_c N^2 \left(\ln\left(\frac{8r_c}{r_w}\right) - 1.75 \right) \quad \text{(Eq. 2)}$$

The circular TMS coil has an approximate inductance of 0.189 mH ($r_c = 45\ \text{mm};\ r_w = 1\ \text{mm};\ N = 9$). The inductor "material" in the case of the TMS coil is the air and head, which have a relative permeability (μ_r) close to that of free space ($\mu = \mu_0 \mu_r;\ \mu_0 = 4\pi * 10^{-6}\ [\text{H/m}]$).

Stimulator Unit Circuit Design

Electric current is generated within the coil by the discharge of a large capacitor within a TMS stimulator unit (Figure 1). The generic circuit of a TMS stimulator unit is shown in Figure 2. A capacitor is charged to a high voltage and then is discharged by a thyristor (an electronic switch). Circuit design requires that the stimulator unit be able to overcome 3kV and 10kA to discharge up to 5MW of power in under 100μs (approx. total discharge of 500J) (Wagner et al., 2007). The discharged electric current pulse flows through the coil windings, producing a magnetic field that changes magnitude over time according to the pulse shape of the current within the coil.

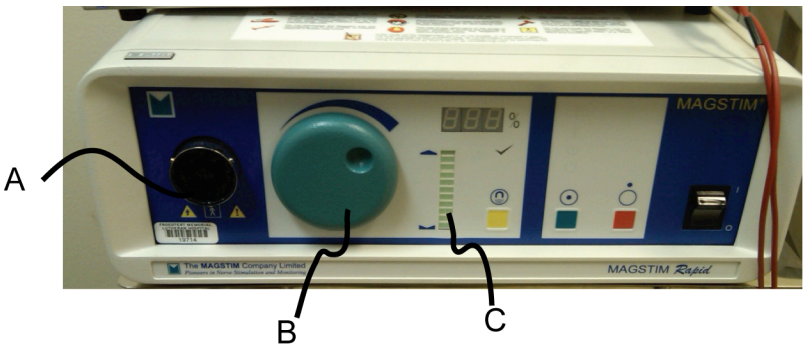

Figure 1 Photograph of the Front End of the Magstim Rapid Stimulator Unit. The coil is attached to the front of the unit (A), the stimulation intensity is set by a dial (B), and a meter indicates the charging status of the capacitor (C).

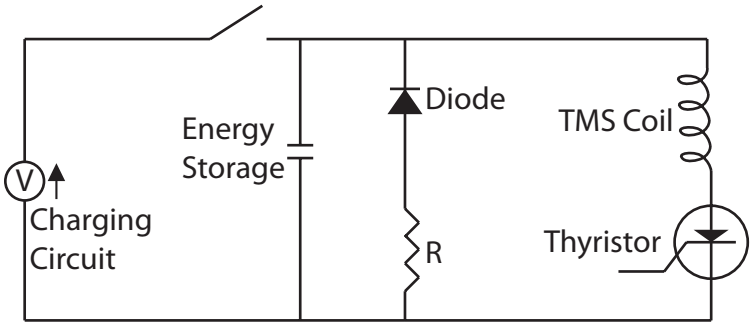

Figure 2 Schematic Diagram of Generic Circuitry for the TMS Coil (Wagner et al., 2007).

The generic circuit is customizable to produce different shapes of current pulses and to account for different rates of stimuli in repetitive TMS (rTMS)[8] applications. There are two primary types of current pulses: monophasic and biphasic (Figure 3). Monophasic waveforms are amenable to single-pulse or paired-pulse TMS (ppTMS)[9] whereas biphasic pulses have an efficiency advantage over the monophasic pulse and are therefore more frequently employed in rTMS applications. The differences between mono- and bi-phasic pulses are: 1) up to 60% of the energy discharged in the biphasic stimulus is returned to the capacitor, which provides a recharging boost for rTMS applications (Jalinous, 1998) and 2) the biphasic waveform has excitable capabilities for twice the duration of the monophasic waveform. Consequently, neural elements seem to show an increased sensitivity to the biphasic waveform over the monophasic (McRobbie & Foster, 1984; Walsh & Pascual-Leone, 2005). Reasons for this phenomenon are attributed to the leaky nature of the cell membrane capacitance. The quick rise time of the biphasic pulse (~60μs; Figure 3A) limits the time for a cell membrane to lose charge during stimulation, whereas the monophasic pulse is slower to rise (having a rise time of

[8] rTMS is carried out by pulse trains of magnetic stimuli usually between 1 and 10Hz. rTMS is known for its lasting effects on the central nervous system.

[9] ppTMS is a research methodology commonly used for investigation in intracortical inhibition or intracortical facilitation. Two consecutive pulses separated by a short interval (usually between 1ms and 8ms) are delivered from a single coil. The first and second pulses are referred to as the conditioning stimulus and the test stimulus, respectively.

~100μs; Figure 3B). To compensate for this slow rise time, monophasic stimulator units (e.g., Magstim 200) are typically designed to output currents that induce much higher E-field magnitude than do biphasic stimulator units (e.g., Magstim Rapid).

Monophasic and biphasic stimulation waveform templates (Figure 3) continue to be used in research and clinical environments with almost no modification because of the effectiveness of the mono- and bi-phasic waveforms as well as the established Food and Drug Administration (FDA) approval for commercial instruments, which normally do not contain interfaces to modify waveform shapes.

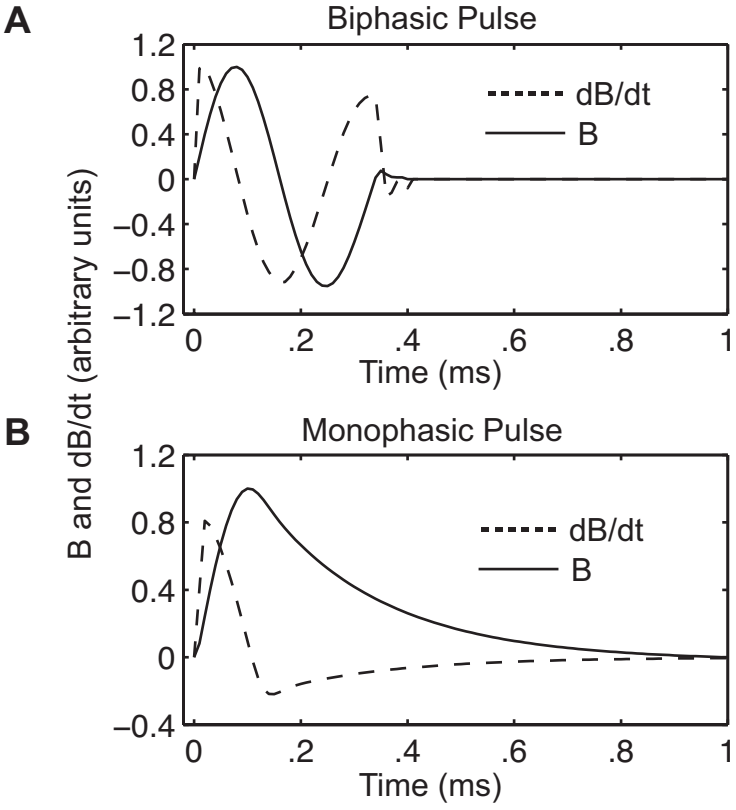

Figure 3 *In vitro* Stimulation Waveform Recordings of the Biphasic (A) and Monophasic (B) Stimulus Pulses from the Magstim Rapid and Magstim 200 Stimulator Units, Respectively.

Is it Electrical Stimulation or Magnetic Stimulation?

The pulses of current delivered from stimulator units vary in duration between 200 μs and 1 ms depending on the stimulator unit. Typical stimulator units have a peak output current of about 8 kA, which generates a time varying magnetic field having a peak magnetic flux of approximately 2 T. Owing to the brevity of the magnetic pulse, the resulting current densities in the cortex can reach 15 mA/sq-cm (Walsh & Pascual-Leone, 2005). The resulting current densities have immediate effects on neural elements throughout a broad region of the brain. By stimulating isolated axons, it has been demonstrated that activation is likely to occur near high electric field gradients along the axis of an axon (Basser & Roth, 1991; Nagarajan et al., 1993).

The classification, “magnetic brain stimulation,” is a misnomer. Neurons in the brain are not stimulated by magnetic fields alone, which can be demonstrated by placing a fixed magnet over the scalp. Without the induction of a *time-varying* magnetic field, no stimulation will occur. As previously mentioned, acute stimulation cannot occur unless the magnetic pulse has a fast rise time, i.e., the magnetic field does not stimulate neurons in and of itself, but neurons effectively respond to the behavior of the electric currents arising from induction. Admittedly, there is controversy about the biophysical mechanisms of neural excitation: are they chemical or electrical in nature? The work presented here assumes the chemical properties of neurons to be electrical mechanisms (Hodgkin & Huxley, 1952).

There are two main distinguishing features between magnetic stimulation and electrical stimulation. Firstly, electrodes that interface directly with neural tissue have *high* electric field gradients near the electrode, which fall off quickly with negligible effects on distant axons. Electric fields from TMS are greater in magnitude, but fall off slowly and have stimulating effects on a large volume. Secondly, electrical stimulation

involves the systemic injection of charge followed by its immediate retrieval. Magnetic stimulation involves only the induction of an electromotive force (EMF), which moves charge rather than injecting it. The nature of magnetic induction is such that the induced electric field exists in both extracellular and intracellular space, which differs from electrical stimulation in that its mechanisms are purely extracellular. In other words, electrical stimulation does not directly interact with intracellular space as magnetic stimulation does, i.e., charge cannot enter (or exit) the cell unless the extracellular potential is such that current loops can form between intra- and extra-cellular space, causing voltage-gated channels to open.

Electrodes have a clear advantage in that the waveform can be customized to have virtually any desired shape, whereas with commercial TMS hardware, the researcher is rather limited. On the other hand, TMS has versatility during stimulation in which the location of stimulation is immediately changeable, which is not a luxury of ECS.

Excitatory or Inhibitory?

It would be convenient if TMS could be explained in terms of excitation or inhibition. Plainly speaking, TMS is noise (Walsh & Pascual-Leone, 2005). Due to the expanse of the electric stimulation from TMS, it cannot be expected to elicit such discriminatory effects as excitation or inhibition. Nonetheless, studies have demonstrated that TMS can produce a signal, e.g., visual sensations and muscle twitches. It has also been shown that TMS can induce inhibitory effects, e.g., motor movement and muscle strength. TMS is normally described as “inhibitory” or “excitatory” in the context of rTMS. During rTMS, trains of magnetic stimuli are delivered at a set frequency. Some therapy sessions can amount to over 600 stimuli, which are delivered in a number of rTMS trains equal in duration.

The FDA has placed limits on stimulation frequency and intensity to avoid seizures. The FDA limits prevent most researchers from delivering >10Hz rTMS. rTMS frequencies are normally described using imprecise terms such as “low-frequency stimulation” (≤ 1 Hz) and “high-frequency stimulation” (> 5 Hz). Inhibitory rTMS has been associated with low-frequency stimulation whereas excitatory rTMS is achieved with high-frequency stimulation (Houdayer et al., 2008).

Researchers use rTMS for interacting with neural circuitry. Stimulation mechanisms in this context relate to the interrupting ability of rTMS within a neural circuit. These mechanisms then are circuit specific and are often coupled with hypotheses in neuroplasticity (Hoogendam et al., 2010; Rossini & Rossi, 2007; Trebbastoni et al., 2013). rTMS is therefore considered “inhibitory” or “excitatory”.

A single pulse of TMS is very likely to have multiple influences on a single cell. Compared to cell membrane time constants, the TMS pulse is nearly a discrete event. The monophasic TMS pulse duration is approximately 15-times shorter than an action potential. The immediate effect of TMS on cell membrane channels has been hypothesized to be heavily dependent on the membrane potential throughout the cell (Edgley et al., 1990, 1997). According to Barker’s activating function[10] (Barker, 1999), cellular activation from a stimulus depends on the orientation and curvature of its axons and dendrites (Ruohonen & Ilmoniemi, 1999). Consequently, the induced electric fields have fortuitous hyperpolarizing and depolarizing actions throughout a single cell. Moreover, suprathreshold E-fields from the figure-8 coil can span the area of three (sometimes more) adjacent gyri, causing stimulation to occur in untargeted areas due to the orientation of certain neural elements. An interesting corollary to this causation is

---

[10] The activating function is proportional to the second spatial derivative of the voltage along the axis of a neuron.

that a single cell can be exposed to depolarizing fields[11] in more than one location. Sites that cause membrane depolarization initiate the propagation of a bidirectional action potential (Basser & Roth, 1991; Pashut et al., 2011). Of course, the initiation of cellular depolarization or hyperpolarization will have immediate excitatory or inhibitory effects on the cell itself.

Direct and Indirect Waves

Suprathreshold TMS elicits two main types of waves that have been identified in electrophysiology recordings within the pyramidal tract: indirect waves (I-waves) and direct waves (D-waves). D-waves are the response of pyramidal cells to direct activation. I-waves are thought to follow trans-synaptic (indirect) activation of pyramidal cells (Silbert et al., 2010) or activation of interneurons that impinge on adjacent pyramidal cells (Davranche et al., 2007; Edwards et al., 2008; Hanajima et al., 2002). D-waves are necessarily earlier in latency than I-waves and are normally observed as corticospinal volleys via epidural recordings. The nature of D-waves and I-waves in magnetic stimulation differs modestly from those from electrical stimulation. Corticospinal volleys from TMS are considered to be either D-waves or I-waves depending on the relatedness to the latencies observed from ECS (Nakamura et al., 1996).

Early studies seemed to show that TMS fails to produce the direct excitation of pyramidal cells that can be observed using ECS electrodes (Day et al., 1987). However, later studies have confirmed the D- and I-wave hypothesis for TMS demonstrated by corticospinal recordings of an initial D-wave followed by a series of I-waves when stimulating the motor cortex in macaques (Awiszus & Feistner, 1994; Baker et al., 1995; Nakamura et al., 1996) and humans (Burke et al., 1993). Baker et al. (1995) show evidence that supports the initial D-wave hypothesis that stimulation occurs very near

[11] In other words, stimulating electric fields that incur depolarization of the cell membrane.

the initial segment of the pyramidal cell axon (Edgley et al., 1990). In this case, direct activation of the pyramidal cell would depend on its membrane potential and the stimulus intensity. Burke et al. (1993) records D-wave latency in humans to be around 4.1 ms when recording from the low cervical region. The I-waves follow behind by milliseconds (multiple waves in increments of approx. 2 ms).

Many studies in conscious humans employ electromyography (EMG) to investigate the effect of changes in TMS parameters on D-wave amplitude. Normally, electrodes are placed in peripheral hand muscles (e.g., first dorsal interosseous, or FDI), and D-waves are recorded during TMS to the primary motor cortex (M1). However, the muscle EMG record lacks the spatiotemporal resolution to disentangle the D-wave and I-wave since the motor evoked potential (MEP) is a summation of the D- and I-waves resulting from depolarization of excitatory neurons (Cheeran et al., 2010). Parsing the D- and I-waves would then require an undesirable deduction concerning the nature of the descending D-wave.

EMG recordings are utilized universally in TMS experiments for two reasons: 1) to establish the resting motor threshold (RMT)[12] stimulation intensity and 2) to locate the motor cortex as a point of reference. Motor cortex stimulation studies are able to gather a good deal of information by employing EMG as a measure of the robustness of motor pool activation (Edgley et al., 1997). As a result, using the EMG muscle record as an indirect measure of direct activation of pyramidal cells in M1 has become a well-established paradigm.

[12] The minimum stimulus intensity that results in an observable EMG response evoked from TMS of the motor cortex.

Medical Imaging and TMS: “Seeing” is Believing

TMS is both an investigatory tool and therapeutic resource for neuromodulation and neurorehabilitation. Its use as a research tool exceeds its use in the clinical setting due to the current inability to reliably predict the physiological response. Its ease of use outweighs its shortcomings, and it has become popular in brain-mapping research. At the advent of TMS navigation systems, the number of functional brain-mapping projects increased exponentially. TMS offers promise as a method for noninvasive brain-mapping, e.g. motor cortex mapping of stroke patients. TMS has its greatest relevance perhaps in preoperative cortical mapping (Julkunen et al., 2009). Navigated TMS facilitates integration with acquired medical images (e.g. MRI) and provides a visual of the TMS coil and brain to aid in “aiming” the induced current, but it cannot predict sites of neural activation.

It has been demonstrated that navigated TMS does not necessarily decrease variability in response (Jung et al., 2010). Many studies, therefore, recommend the integration of (costly) robotic arms to maintain a steady coil orientation even during head movement (Rotem et al., 2014; Salinas et al., 2011; Siebner et al., 2009). Most approaches still rely on a head localizer fixed on the subject head. Since head localizers are often flimsy and uncomfortable, new approaches seek to use headgear that enables the coil to be attached and secured in a fixed position relative to the head. TMS helmets are being explored to better constrain TMS parameters (Y. Roth & Zangen, 2014).

The improvements in TMS stability provide hope for increased reliability in clinical applications. Nonetheless, questions remain in TMS neuromodulation: what, where, and how is it stimulating? Efforts to answer these questions have led to the development of TMS-compatible hardware for integration with current imaging modalities such as functional magnetic resonance imaging (fMRI) (Grefkes et al., 2010), positron emission

tomography (PET) (Krieg et al., 2013), magnetoencephalography (MEG) (Hallett, 2007), electroencephalography (EEG), and single-photon emission computed tomography (SPECT) (Wyckhuys et al., 2013), but these modalities have neither the spatial nor temporal resolution to capture the immediate effects of magnetic stimulation on neural tissue in the brain. However, some effects of TMS last long enough to observe neural network effects in, for example, fMRI via blood-oxygen-level dependent (BOLD) signals (Caparelli et al., 2010; Moisa et al., 2009), but the mechanisms of neural activation remain unidentified. Though indirect effects of TMS can be measured through medical imaging modalities, it remains impossible to "see" the brain respond to TMS.

Modeling in Neuromodulation

The present technologies in neuromodulation modeling can be traced back to the first nonlinear model of the cellular transmembrane potential in a large axon (Hodgkin & Huxley, 1952). Since then, mathematical modeling in neuromodulation has matured to a level of sophistication where cell activation and patient responses to neuromodulation therapy can be predicted with reasonable confidence (McIntyre et al., 2004; Riva-Posse et al., 2014). Recent techniques provide an innovative way to investigate modulatory effects in ways that are currently impossible with medical imaging modalities. Mathematical modeling is widely applied in various fields of neuromodulation including DBS (Butson et al., 2007), transcranial direct current stimulation (tDCS)[13] (Datta et al., 2009), and TMS (Thielscher et al., 2011). Modeling techniques in neuromodulation are necessarily computational in nature because of the complex geometry of the nervous system and the nonlinearity of neurons. It has been demonstrated that computational modeling in neuromodulation can provide insight into mechanisms of activation (Butson

[13] tDCS is a neuromodulation technique designed to stimulate cortical structures by means of current flow between two large patch electrodes (an anode and cathode) adhered to the scalp.

& McIntyre, 2005) as well as predict patient outcomes for therapy (Chaturvedi et al., 2010).

Today, models are built by integrating medical imaging modalities with modeling software to construct detailed models of neuroanatomical structures (Butson et al., 2011; Datta et al., 2009). The accuracy with which patient outcomes can be predicted seems to depend on the geometry of the brain. Cortical folds and nonhomogeneous material properties of the head have been shown to influence the electric field (Salinas et al., 2009; Thielscher et al., 2011). For this reason, estimating electromagnetic tissue properties (conductivity; permittivity; permeability) in the head has become the focus of research (De Lucia et al., 2007; Tuch et al., 2001).

Investigators in DBS modeling research have set a new standard for the predictive ability of modeling in neuromodulation. Early DBS modeling approaches demonstrated that a probabilistic maps of the volume of tissue activated shows correlations with patient outcomes (Butson et al., 2007). Recently, the approach developed by Butson and McIntyre (2007) has been applied to DBS for depression and the activation of specific fiber pathways (Riva-Posse et al., 2014). Models used in clinical applications are normally patient-specific[14]. Geometry-dependent models (e.g., responses that depend on the orientation of cortical folds) employ finite element methods[15] to calculate the bioelectromagnetic fields in neural tissue. Detailed models (as in DBS) integrate patient-specific finite element models (FEM) and nonlinear time-dependent neuron models to predict areas of neural activation during stimulation (Maks et al., 2009).

---

[14] Or *subject-specific*.
[15] See Engineering Approaches to Modeling TMS, p. 23.

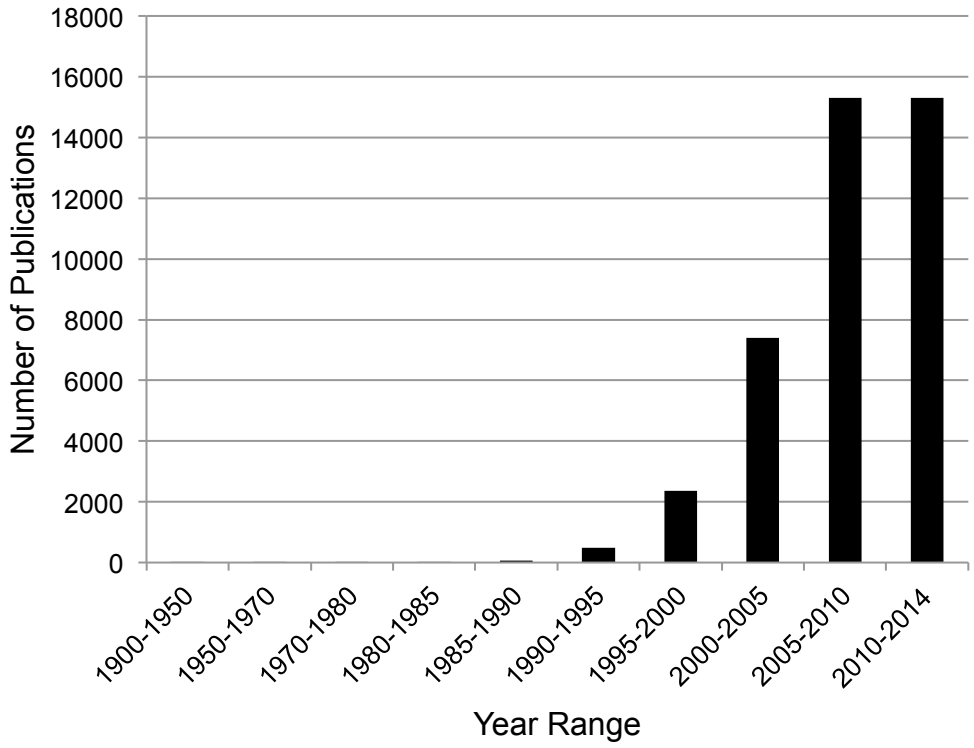

Figure 4 Number of publications in TMS modeling. Publications are listed by year range (note the changing bin size). The number of publications for each year range was obtained through GOOGLE scholar search using the keywords, "'transcranial magnetic stimulation' modeling" excluding patents and citations.

Engineering Approaches to Modeling TMS

The number of studies in computational modeling for TMS has dramatically increased in popularity since the mid 1990s (Figure 4). Early TMS modeling studies have a focus on analytically solving the electromagnetics of TMS (Tofts, 1990) and to the response of axons to magnetic stimuli (Basser, 1994; Nagarajan et al., 1993; B. J. Roth & Basser, 1990; Warman et al., 1992). The basic biophysical mechanism of TMS is the induced electric field in neural tissue. Accurate models for TMS are therefore viewed as necessary to provide the required improvements for its implementation (Opitz et al., 2013).

Modeling in TMS is warranted by its clinical use as an outpatient, noninvasive, neuromodulation tool. Modeling projects in TMS aim to accomplish two main goals that are impossible with neuroimaging: 1) better predict areas of activation during TMS and 2) uncover mechanisms of activation and variability in physiological response. Efforts are being made on these fronts to improve the reliability of TMS as a noninvasive therapeutic option of neuromodulation. Additionally, a better understanding of the mechanisms of activation would provide information about the spread of neural activity throughout the cortex and into deeper brain structures immediately following stimulation.

TMS has three main parameters that influence the type, location, and intensity of stimulation in the brain: 1) coil geometry (dimensions; number of windings); 2) stimulus pulse shape, amplitude and duration and 3) coil location and orientation relative to the head.

Coil and Waveform

Salinas et al. (2007) performed x-ray measurements of the dimensions of commercially available coils, recorded magnetic field measurements, and developed a validated model of the figure-8 TMS coil. TMS coil models are designed to predict either the maximum B-field or the maximum magnetic vector potential (**A**; A-field) produced by the coil in 3D space during a single stimulus. According to the principle of induction, the magnetic field produced by the coil is linearly dependent on the electric current flowing through the coil windings during induction. Therefore, the magnetic field at any point during the stimulus can be obtained by a scalar transformation. Coil models can now be employed in conjunction with human experimentation since the advent of TMS navigation systems, which have made it easy to acquire coil positions *post hoc*.

Few studies have investigated the effects of TMS by modeling the time-dependent electric field induced in an axon or cell body (or both) (Basser, 1994;

Nagarajan et al., 1993; Pashut et al., 2011; Warman et al., 1992). In these cases, the neuron (or axon) was modeled in a uniform electric field caused by induction. To our knowledge, no FEM approaches employ a time-dependent waveform to estimate induced fields throughout its duration (Chen & Mogul, 2009; Laakso et al., 2014; Opitz et al., 2011, 2013; Salinas et al., 2007, 2009; Thielscher et al., 2011). Instead, these studies assume single-frequency conditions to compute the induced fields.

Medical Imaging

Medical imaging techniques play an important role in model development for TMS, especially in calculating the electric field induced within the brain. The induced electric field depends on biological tissue properties, which are normally acquired via medical imaging paradigms (Opitz et al., 2011; Tuch et al., 2001). Consequentially, the anatomical accuracy of a subject-specific model is limited by medical imaging modalities. In most cases, the efficacy of TMS depends on the anatomical structure of the patient. As a result, subject-specific modeling techniques have a key role in TMS models.

Our knowledge of the interactions between the induced electric field and the physiological effect in the brain depends on anatomical connectivity[16] information. In many applications (e.g., treatment of depression), TMS aims to innervate deeper structures as well as cortical structures based on anatomical connectivity. Connectivity information can be acquired through a diffusion-weighted image (DWI) from nuclear magnetic resonance (NMR)[17] imaging. Additionally, the induced E-field depends on anisotropic material properties of the brain, especially in terms of the E-field vector orientation relative to conductivity tensor orientation (De Lucia et al., 2007). This

---

[16] The term “connectivity” is purposefully used in an ambiguous manner because of its broad application and relevance to both global connections (fiber pathways) and local connections (synapses) in the brain. See also “The Human Connectome Project” (http://www.humanconnectomeproject.org/).

[17] Or “magnetic resonance” (imaging), i.e., MRI.

information is normally gathered through a diffusion tensor image (DTI) that is derived from the DWI. The electrical conductivity tensor is a direct map from the diffusion tensor obtain via NMR (Tuch et al., 1999, 2001).

Subject-specific Finite Element Method

Subject-specific models are based on the finite element method to estimate the induced electromagnetic field. The finite element method is a numerical method to approximate the solution to a problem that contains complex geometrical features. The finite element method has two main computational processes: 1) geometrical entities are discretized into many finite elements or "links" to create a "mesh", and 2) a system of equations is solved by inverting the "stiffness" matrix (De Lucia et al., 2007). The number of variables in the system of equations is equal to the number of elements in the mesh. FEM equations are usually set up to minimize an error function (e.g., total energy of the system) to arrive at a numerically stable solution. The FEM approach is commonly used in modeling bioelectromagnetic fields for neuromodulation investigation (Chen & Mogul, 2009; Datta et al., 2009; Güllmar et al., 2010). The finite element method for electromagnetic dynamics is well established (Bastos & Nelson, 2003). Since the induced electric field is time-dependent, simplifications are usually made to compute the electric field at an approximate fundamental frequency[18].

Early FEMs used simplified head geometries for predicting the magnitude of induced currents (Davey, 2003). The variety of brain shape and cortical structure among subjects limits the usefulness of simplified models. Subject-specific models have shown marked improvements in electromagnetic predictions due to the impact of gyral geometry on the induced electric field (Opitz et al., 2011). The finite element method has

[18] The fundamental frequency approach is used in most models. This particular response solves the FEM at the frequency having the highest amplitude on the periodogram of the TMS waveform.

become an appealing approach as advancements have been made to merge medical images into 3D models (Dale et al., 1999; Jenkinson et al., 2012; Tadel et al., 2011). Subject-specific models are built from structural MR images and then segmented to obtain surface boundaries among the scalp, skull, cerebrospinal fluid (CSF), gray matter (GM), and white matter (WM).

Cellular Modeling

The effects of TMS are normally reported in terms of the electric field (magnitude, direction, or both) that is induced in the cortex. To our knowledge, no advancement has been made in modeling the cellular effects of TMS beyond the activation of an axon under varying magnetic stimulation conditions (Nagarajan et al., 1993). Pashut et al. (2011) modeled the response of a pyramidal cell to an electric field induced in a homogeneous medium from a circular coil. Pashut and colleagues report that their model indicates that excitation tends to occur within the soma of the cell.

Significance

Neuromodulation offers promise for treatment resistant patients or patients with neurological diseases untreatable by pharmaceutical drugs. Many patients are debilitated to the point where they seek relief through chronic implants for brain stimulation. Today, chronic implants are more therapeutically viable than TMS, but the risks (short and long term) associated with invasive surgery are greater than those with TMS. In many cases, patients view the potential benefit of a chronic implant to outweigh the risks. Even though TMS has been shown to induce long-term modulatory effects for a range of disorders, patients are more inclined to go with a chronic implant because outcomes are less variable than those from TMS. In recent years, neuromodulation research has advanced due to the use of patient- or subject-specific approaches,

especially for DBS (Butson et al., 2007; Chaturvedi et al., 2010), which resulted in the development of techniques for improving surgical planning. However, a subject-specific approach for TMS treatment planning has not been developed. The long-term goal of this dissertation work is to develop a patient-specific tool that enables the clinician to form a TMS treatment strategy.

Many published TMS studies provide a qualitative, rather than quantitative, description of the coil placement relative to the targeted brain region. The magnitude and direction (relative to neural structures) of the electric field induced by TMS is commonly used as a predictor of neural activation (Fox et al., 2004; Opitz et al., 2013; Salinas et al., 2009; Thielscher et al., 2011). Such approaches have limitations, e.g., the range of electric field magnitudes considered suprathreshold is a required assumption to identify sites of neural activation. At the same time, few studies account for the detailed morphology of the cortical surface or the position and orientation of individual neural elements in the cortex and white matter layers relative to the induced E-field. As a result, TMS has unrealized potential in two general scenarios: as a neuromodulation therapy and as a tool for neurophysiology studies. Two primary problems limit its usefulness: 1) the variability in physiological response within subject and subject populations and 2) the mechanisms and targets of TMS remain elusive. These complications hinder our current ability to predict the immediate effects of TMS and accurately prescribe therapy in terms of the free[19] parameters of TMS.

This dissertation provides a quantitative characterization of the interactions between the electromagnetic field and excitable neural elements in the cortex (pyramidal cell neurons). These results could provide information necessary to effectively activate,

[19] i.e., parameters that can be manipulated by the clinician. Free parameters are coil placement relative to the head, stimulation intensity, and stimulation frequency. Currently, fixed parameters are stimulation waveform and coil shape.

or avoid activating, cortical target regions using TMS. Additionally, this engineering approach provides detailed information about the immediate effects of TMS on a cellular level, which likely has value in many areas of neuromodulation research. For example, this approach can provide a metric of comparison between different modes of neuromodulation such as TMS and ECS. This comparison is especially advantageous for use in screening for implanted neuromodulation devices. The results of this study offer insights into important fundamental questions in the clinical application of TMS: 1) What are possible sources of variability? 2) What areas of the brain can be modulated using TMS? 3) Can TMS treatments be planned to ensure modulation of specific cortical regions?

The long-term implications of this dissertation have an impact in TMS use for predicting activation within and around targeted cortical regions. This methodology is also translatable to other areas of neuromodulation, and could enable effective treatment planning for TMS, ECS, or tDCS.

EXPERIMENTAL PROCEDURES

The experimental procedures and protocols performed in this study (Specific Aims 1, 2, and 3) were carried out with Institutional Review Board (IRB) approval (HR-2257 and PRO00014800 "*Quantifying TMS Variability*") from Marquette University and the Medical College of Wisconsin (Milwaukee, WI). All human experiments complied with HIPAA and Human Subjects Research. All computational experiments are original work or adaptations of previously published work available for research use (Amatrudo et al., 2012; Butson et al., 2007).

Motor Cortex Stimulation via TMS in Humans

Recruitment

Subjects were recruited via word of mouth, and then screened and given informed consent. Subjects did not receive a stipend for enrollment. Inclusion criteria for subjects were: 1) subjects may be of any ethnicity or gender, and must be 18 years of age or older; 2) subjects must be cognitively capable of informed consent. The strict exclusion criterion was: 1) any metal in the head. Subjects were considered for exclusion if they had: 1) cardiac pacemakers, 2) implanted neurostimulators, 3) implanted medication pumps, 4) intracardiac lines, 5) significant heart disease, 6) bipolar disorder (to reduce risk of mania), 7) history of stroke or other brain lesions, 8) history of suicide attempt(s) in subjects with psychiatric disorders, 9) personal history of epilepsy, 10) family history of epilepsy, 11) pregnant women, or 12) patients receiving tricyclic antidepressants or neuroleptics.

Medical Imaging

If the subject did not have usable available MRI scans, a protocol[20] was designed to acquire a high-resolution anatomical volume and DTI from the ventral limit of the cerebrum to the dorsal limit of the scalp. Medical images were acquired prior to TMS for utilization with TMS navigation. Prior to imaging, the subject was screened according to MRI safety standards of the Medical College of Wisconsin IRB.

Experimental Procedure

Experiments began by seating the subject in a moderately reclined position to achieve a comfortable resting position. The chair position locked to prevent further

---

[20] See Appendix D, p. 159 for details of the medical image acquisition protocol design.

movement. The subject's head was placed on a padded headrest designed to limit head movement during the experiment.

The subject wore an elastic headband with a localizer attached to it. The localizer is used by the navigation system to track the head position/orientation during the experiment. The position of the localizer relative to the head was determined from a calibration before each TMS session, which entailed gently touching a plastic stylus to the forehead and each ear of the subject.

The subject's MRI was loaded into the navigation system. The MRI may have been acquired as part of the study but was not required. If a subject did not have an MRI, an atlas brain was used instead.

The subject had simultaneous EMG and/or EEG recordings during TMS. EMG recordings were made via pairs of adhesive skin electrodes that were placed over muscle groups on the arm or leg contralateral to the side of the brain being stimulated. EEG recordings were made via a 128-channel EEG cap. A conductive gel was applied between the EEG electrodes and the scalp using a syringe. A reference electrode was placed at a distant location such as the abdomen or leg.

The subject received single (<1Hz) TMS pulses of variable intensity. The RMT was determined as the minimal intensity capable of evoking MEPs in 5 out of 10 consecutive trials for a hand muscle with an amplitude of at least 50mV in the EMG recording, or by a observing a consistent hand/arm response, as the coil was moved along a regular grid over the left frontal convexity. The TMS pulse was delivered by a Magstim figure-8 coil. The coil handle was fixed to a mechanical arm to suppress movements of the coil from the original position on the scalp.

In order to obtain a measure of intracortical interactions, the subject received ppTMS. Two pulses in rapid succession were delivered (<10 ms apart); the first pulse below RMT and the second pulse above RMT. Paired-pulses were applied at intervals of 2 sec or greater in order to preserve an average pulse rate <1Hz.

Data analysis was conducted using the available medical images (MRI and/or DWI) of the subject's head, and the EMG record during TMS.

Model Corroboration

Whole head medical image volumes (anatomical MRI and DWI) were used to construct a model of the subject's head for predicting neural activation during a single TMS pulse. Electrophysiology recordings from human experimentation were used as a measure of corroboration of the subject-specific modeling approach.

CHAPTER 1

CONCEPTUALIZATION AND CREATION OF A MULTISCALE, BIOPHYSICALLY BASED, COMPUTATIONAL MODEL OF TMS

INTRODUCTION

Despite decades of scientific research, the mechanisms of activation during magnetic stimulation remain elusive. Computational models of TMS have been used to predict the induced electromagnetic fields and possible sites of activation. Additionally, modeling provides potential insights into sources of variability, which have been suggested to exist at the neuronal level (micro) and also at the level of gyri and sulci (macro) (Ahdab et al., 2010; Ridding & Rothwell, 2007). Multiscale modeling could bridge the knowledge gap between macro and micro level interactions.

The mechanisms of activation during TMS are often likened to those from electrical stimulation (e.g. ECS) (George et al., 1999). Even the accuracy of TMS is often compared to that of ECS, even though there isn't a strong rationale for this comparison. Although both magnetic and electrical stimulation influence neuronal activity, these paradigms interface with membrane ion channels in different ways. Electric stimulation adds charge into extracellular space whereas magnetic stimulation imposes an electromotive force on charge in both extracellular and intracellular space.

During TMS, a large capacitor bank is discharged, causing rapid current flow through windings in a coil. Through induction, a rapidly changing magnetic field (about 2 Tesla) permeates the cerebrum. The magnetic field (B-field) strength falls off at a rate $\propto 1/R^2$. The B-field varies spatially and temporally, which gives rise to an electric field (E-field) that exerts an electromotive force (EMF) upon charged particles within the brain. These immediate effects of TMS are difficult to predict due to the convolution of

the cortical surface and the span of high intensity E-fields induced in the brain. As a result, computational models have been employed more frequently to better understand TMS. Modeling studies normally fall into three main categories: 1) electromagnetic field modeling, 2) axon modeling, and 3) network models (commonly employed in rTMS studies) (Reis et al., 2008). The first is based on electromagnetic physics (Chen & Mogul, 2009; Miranda et al., 2003; Salinas et al., 2007), the second on Barker's activating function and cable models (Barker, 1999; Basser, 1994; Nagarajan et al., 1993; Warman et al., 1992), and the third involves investigating brain function by modulation of broader networks. Recent modeling studies have aimed to physiologically validate a model based on electric field vector orientations relative to cortical geometry (Opitz et al., 2013). To our knowledge, a model that integrates E-field interactions within the brain with time-dependent biophysically based neuron models has not been developed.

The purpose of this study was to develop a subject-specific TMS model that can predict the mechanisms of TMS-induced activation. We tested the hypothesis (Burke et al., 1993; Edgley et al., 1990, 1997) that variability in neural response can be partly attributed to variations in membrane potential of excitable pyramidal cells. We also tested the effects of two different TMS pulse waveforms from commercial stimulator units.

The state of the art in TMS modeling has not yet advanced to include the E-field impacting neural elements within the brain. For Specific Aim 1, we created a multiscale, biophysically based computational model for use in TMS research. Our *motivation* for this approach is that TMS targets are not well understood and previously published model-based predictions rely only on the induced E-field at a single frequency. Our modeling approach is *novel* because it accounts for the time-dependent characteristics

of the E-field and it integrates two components that have previously been employed only independently: 1) a time-dependent electromagnetic field solver for any TMS waveform and 2) simulations of a multicompartmental pyramidal cell neuron model to TMS stimuli (Amatrudo et al., 2012). In summary, we define, describe, and model the physical and biophysical parameters at the interface of the induced E-field and neural elements. *We hypothesized that multiscale computational models with biophysically based properties can accurately predict the neural response to TMS.*

METHODS

i. Figure-8 TMS Coil Model Development

We constructed a figure-8 TMS coil model to accurately estimate the induced electromagnetic fields during a single pulse stimulus. The goal was to develop an analytical coil model that is adaptable for subject-specific use. Since the shape of the coil windings play a significant role in the spread of stimulation, the model was based on coil measurements by Salinas et al. (2007). Salinas and colleagues measured the geometry of the coil windings via x-ray and recorded the spatial dependence of the magnetic field produced from the coil. In this study, the electrical characteristics of the coil were modeled according to manufacturer specifications (Jalinous, 1998) and *in vitro* recordings.

Table 1 Coil Geometry. (From measurements by Salinas et al., 2007 for the figure-8 coil). All units are in millimeters.

Coil Loop	Center (x-coordinate)	Inner Radius	Outer Radius	Number of turns	Wire Width	Wire Height
1	-46.63	28.36	44.98	9	1.5	7.25
2	47.11	28.11	44.43	9		

A model of the coil current pulse waveform was developed from *in vitro* recordings. The Magstim 200 stimulator unit delivers a maximum of 8 kA through its windings (Jalinous, 1998). The current pulse was recorded in-vitro by a custom built magnetometer made of a double turn wire loop (D = 2 cm). We measured the time-varying EMF from the coil leads via Cambridge Electronics Design (CED) Power 1401 multichannel recording system integrated with Spike2 (CED) using a sampling rate of 100kHz. EMF transients were obtained for both the monophasic and the biphasic waveform, which are produced by the Magstim 200 and Magstim Rapid stimulator units, respectively. The TMS coil current was indirectly calculated by computing the discrete-time integral of the measured EMF.

An analytical model of the TMS coil windings by discretizing each coil turn was constructed based on previously published x-ray measurements of the coil geometry (Table 1). Each turn of the coil is made up of hundreds of elements that represent current dipoles (**Q** [A·m]). The induced magnetic vector potential (**A** [Wb/m; V·s/m]; A-field) or magnetic field (**B** [T; V·s/sq-m]) can then be calculated at any point (*p*) in space. The A-field resulting from a current dipole has the relation

$$\mathbf{A} = \frac{\mathbf{Q}\mu_0}{4\pi R} \qquad \text{(Eq. 3)}$$

where *R* is the distance from the current dipole to any point in space and μ_0 is the magnetic permeability constant ($4\pi \cdot 10^{-7}$ H/m). The B-field is obtained by calculating the curl of the A-field.

$$\mathbf{B} = \nabla \times \mathbf{A} \qquad \text{(Eq. 4)}$$

The custom coil model was comprised of 7200 current dipoles to describe the current flow through the coil windings (Figure 5). The A-field at any point, *p*, is calculated by superposition.

$$\mathbf{A}_p = \frac{\mu_0}{4\pi}\sum_i \frac{\mathbf{Q}_i}{R_i} \quad \text{(Eq. 5)}$$

where $\mathbf{Q}_i$ is a single current dipole and R_i is the distance from the current dipole to point *p*.

We compared our model predictions with the model developed by Salinas et al. (2007), which was validated by magnetic field measurements, and compared the E-field magnitude maps with those from Walsh and Pascual-Leone (2005).

The objective was to develop a validated figure-8 TMS coil model to accurately predict the electromagnetic fields produced within the head during a single stimulus pulse. This model was also designed for integration with subject-specific head models that would be built from medical image processing software (Figure 5).

ii. Time Dependencies: Fourier Solver vs. Single-frequency Approximation

We developed a custom Fourier Solver using m-script (MATLAB v8.1, MathWorks Inc.) to calculate the time-dependent electromagnetic solution from a discrete Fourier series, to enable computation of the time-dependent electromagnetic field solution induced by any TMS stimulus waveform, and to work together with frequency domain finite element solvers. The input to the Fourier Solver is the electric current waveform, or the discrete-time function of $\mathbf{Q}$ (Eq. 3 and Eq. 5).

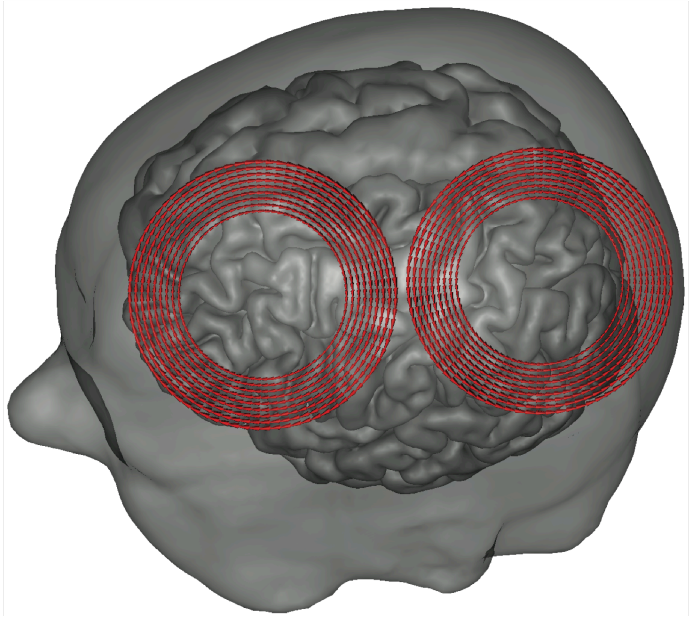

Figure 5 Figure-8 TMS Coil Model. The current dipoles to approximate the current through the coil windings are shown as red vectors. The coil is placed over a sample head to demonstrate its use in subject-specific modeling.

Previous studies reduce the TMS pulse to simple waveform features such as the rise-time or a single-frequency sinusoid. However, the single-frequency approximation oversimplifies the TMS waveform since most of the power in its spectrum is contained between 0 and 10 kHz.

Many brain stimulation devices employ a square biphasic waveform where static assumptions apply. However, a square waveform is problematic for use in TMS since the induced E-field is proportional to the rate of change of the magnetic field. Magnetic stimulator units are designed to produce a continuously variable, transient stimulus waveform. Previous studies attempt to model the E-field during the instant at stimulus onset when the first derivative of the coil current is at its peak by assuming steady-state[21] conditions. This assumption has been widely employed in TMS modeling due to

[21] Steady-state conditions, unless noted otherwise, refers to the electric current through the coil at either a constant rate of change or a single-frequency sinusoid.

its simplicity and low computational load. Steady-state conditions have been modeled in two different ways in TMS literature: 1) a constant rate of change of coil current flow or 2) a single-frequency oscillating sinusoid.

The Fourier Solver computes the induced E-field under quasistatic conditions at every Fourier component in the spectrum of the TMS waveform from a 512-point discrete Fourier transform (DFT). The result is a frequency response that is then transformed back to the time-domain via the inverse DFT. The output of the Fourier Solver is the theoretical discrete-time solution. Procedural computations of the Fourier Solver are outlined in Figure 6: 1) the time-dependent stimulus waveform is transformed into a discrete Fourier series via the FFT (fast-Fourier Transform), 2) the electromagnetic solution is computed at each component of the Fourier series, and 3) the Fourier series of the electromagnetic solution is transformed into discrete-time via the inverse FFT (IFFT).

We compared the time-dependent solutions from the Fourier Solver with those from previously published studies that assume steady-state conditions (and its respective variants). This simplification is prevalent in TMS modeling studies. For example, Thielscher et al. (2011) assume steady-state conditions using a fixed rate of change of coil current (1A/μs). Miranda et al. (2003) approximate the TMS waveform as a fixed rate of change of current of 100 A/μs, and Chen and Mogul (2009), as well as Kowalski et al. (2002), approximate the magnetic stimulus as a 2440Hz sinusoid. For the sake of comparison, the rise-time (from Thielscher, 2011 and Miranda, 2003) was converted to a single-frequency sinusoid. The Fourier Solver was implemented using a 512-point DFT to estimate the solution from the stimulus waveform. Our objective was to develop a validated algorithm to compute the time-dependent solution and compare its results with previously published approaches.

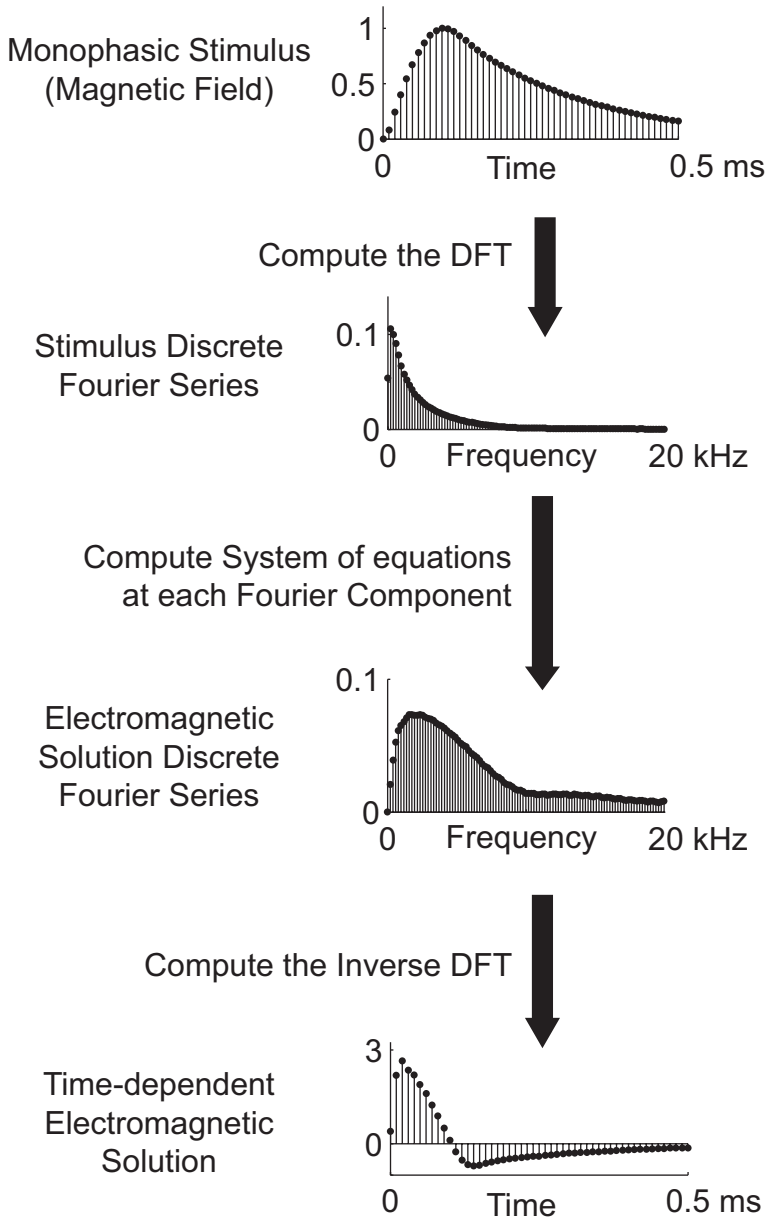

Figure 6 Fourier Solver Calculation Steps. The numerical process to calculate the time-dependent electromagnetic solution from a transient magnetic pulse has three steps indicated by the black arrows. In the case of TMS, the magnetic source is the electric current flowing through the TMS coil. The Fourier Solver was developed for use in finite element methods (middle black arrow).

iii. Conceptualizing Barker's Activating Function

To investigate the implications of the activating function (f; Eq. 6) value on different orientations of a straight axon relative to the fields produced by the TMS coil, we created a conceptual model of f along a straight hypothetical axon within the stimulating E-field of two widely used TMS coils (figure-8 and circular).

Barker's activating function (Barker et al., 1985) has traditionally been used as a tool to explain the mechanisms of TMS on the neuronal level as it relates to the induced E-field. The activating function is formally defined as proportional to the transmembrane potential resulting from an induced E-field.

$$f = \frac{\partial^2 V}{\partial x^2} = \frac{\partial E_x}{\partial x} \qquad \text{(Eq. 6)}$$

The f function is the first spatial derivative of the E-field along the axis (x) of the axon, which is a coarse approach to predicting neural activation because the transmembrane potential is proportional only to f, and it has no time-dependent term. However, f can be calculated at discrete time points in the TMS waveform using the E-field computed from the Fourier Solver. The activating function has usefulness as a predictor of activation sites during suprathreshold stimulation in tube-like neural elements as in the cable model (Basser & Roth, 1991). Our objective in this study was to build upon the activating function model by demonstrating its application in a simple case.

iv. Theoretical Analysis of the Magnetic Stimulus

In light of Barker's activating function, the monophasic and biphasic pulses have biophysical implications. We therefore applied principles in electrodynamics to test the hypothesis of the activating function for monophasic and biphasic magnetic stimuli. The

forces exerted on an ion channel throughout the duration of a biphasic or monophasic time-varying magnetic stimulus were qualitatively described using a combination of Maxwell's equations with Ampere's law of charge conservation.

A single neuron in the presence of a suprathreshold magnetic stimulus is subjected to high intensity E-fields that can cause membrane polarization. Throughout the stimulus duration, a single ion channel on a patch of membrane experiences a unidirectional or bidirectional EMF according to the stimulus waveform. Polarization across ion channels happens according to the induced EMF in agreement with Maxwell's equations. The EMF arises from the induced E-field according to Maxwell's equations and Ampere's law of current conservation, which is computed by the Fourier Solver. The E-field is described in discrete-time by the A-field and the gradient of a scalar potential (Φ) caused by charge distribution for dynamic situations[22] (see also Eq. 4).

$$\mathbf{E} = -\nabla\Phi - \frac{d\mathbf{A}}{dt} \qquad \text{(Eq. 7)}$$

Cell membrane polarizations are believed to be a function of the E-field magnitude and the relative structure or shape of the neural element (Barker et al., 1985). The lipid bilayer of the cell membrane acts as an insulator permitting electric current flow in only the axial direction. Therefore, a patch of cell membrane normal to the E-field direction would experience no current flow, but the highly conductive intracellular space would experience high currents in the axial direction according to the magnitude of the axial component of the E-field. Charge can enter or exit a system (e.g., intracellular space) in a manner according to Ampere's law of charge conservation.

---

[22] See Appendix A, p. 158, for a description of Maxwell's equations.

$$\mathcal{Q}_{in} - \mathcal{Q}_{out} = \nabla \cdot \mathbf{J} + \frac{\partial \rho}{\partial t} = 0 \quad \text{(Eq. 8)}$$

Equation 8 describes charge/current conservation of a system ($\nabla \cdot$ is the divergence operator, $\mathbf{J}$ is current density, and ρ is charge density of the system). In electrostatics, unless sources or sinks exist, it is normally assumed that $d\rho/dt = 0$. The current density is related to the induced E-field by

$$\mathbf{J} = \mathbf{E}\sigma \quad \text{(Eq. 9)}$$

and within intracellular space, this reduces to

$$\mathbf{J} = \mathbf{E}_x\sigma \quad \text{(Eq. 10)}$$

where $\mathbf{E}_x$ is the axial component of the E-field in intracellular space. If the system is defined as the intracellular space of a neuron compartment having an axis (x) and a spatially varying E-field ($d\mathbf{E}_x/dx \neq 0$), it follows from Eq. 10 and Eq. 8 that the divergence of $\mathbf{J}$ is non zero. Thus, residual charge presents itself in the system ($d\rho/dt \neq 0$) throughout the duration of the TMS stimulus. Charge either builds up or is removed from the inside of the membrane wall, which causes local areas of the membrane wall to experience depolarization or hyperpolarization. The many ion channels and pumps that line the membrane wall are exposed to a voltage load that works with or against the ionic gradients. Under these conditions, immediate cellular response is governed by the membrane capacitance (assuming the charge buildup is a transient), potassium leak channel (leakage current), and voltage gated ion channels.

To test the hypothesis of the activating function in magnetic stimulation, we developed a theoretical model based on Ampere's law of current conservation (Eq. 8). The activating function, f, should predict the relative magnitude and polarizations of the transmembrane potential.

The cell membrane was assumed to be made up of passive ion channels within a membrane having electrical insulation properties. The system boundary encloses a volume of intracellular space in a curved axon with a 90º bend. This system design causes $d\mathbf{E}_x/dx$ to be non-zero and thus $\nabla \cdot \mathbf{J}$ is non-zero. We assumed the environment was strictly ohmic according to quasistatic conditions. These conditions were analyzed at three discrete-time points throughout the monophasic and biphasic stimulus pulse in order to approximate the relative charge transfer during a magnetic stimulus and to create a conceptual base for understanding activation mechanisms of magnetic stimulation.

v. The Response of a Passive Cylindrical Axon to a Monophasic Stimulus

We developed a 3D cylindrical model of a bent axon segment to investigate time-dependent effects that result from a monophasic magnetic stimulus on a passive cell membrane of an axon segment. The solution to Maxwell's equations and Ampere's law of current conservation was computed using the Fourier Solver in conjunction with the magnetic and E-field (*mef*) solver in COMSOL Multiphysics. The axon segment was modeled in an extracellular medium having material properties as defined in Table 2. Material properties were chosen based on consensus (Carnevale & Hines, 2006; Chen & Mogul, 2009; Güllmar et al., 2010; Opitz et al., 2011; Thielscher et al., 2011).

Table 2 Material Properties of Axon Segment Model.

	Extracellular Space	**Intracellular Space**	**Cell Membrane**
Conductivity	0.276 S/m	2.825 S/m	0.3 mS/cm^2
Capacitance	-	-	1 μF/cm^2
Permeability	$1\mu_0$	$1\mu_0$	-
Permittivity	$1\varepsilon_0$	$1\varepsilon_0$	-

We compared the transmembrane potential from the axon segment model to the theoretical analysis. Model entities were assumed to have no effect on the induced magnetic field ($\mu = \mu_0$) and dielectric effects of intracellular and extracellular space were assumed negligible ($\epsilon = \epsilon_0$). The axon diameter was set to $D = 5\mu\text{m}$, its length $L = 200\mu\text{m}$, and the radius of curvature at the bend was 3x the diameter ($r = 15\mu\text{m}$). Membrane properties were assigned based on default passive membrane parameters from NEURON v7.3 (Yale, New Haven) (Thielscher et al., 2011).

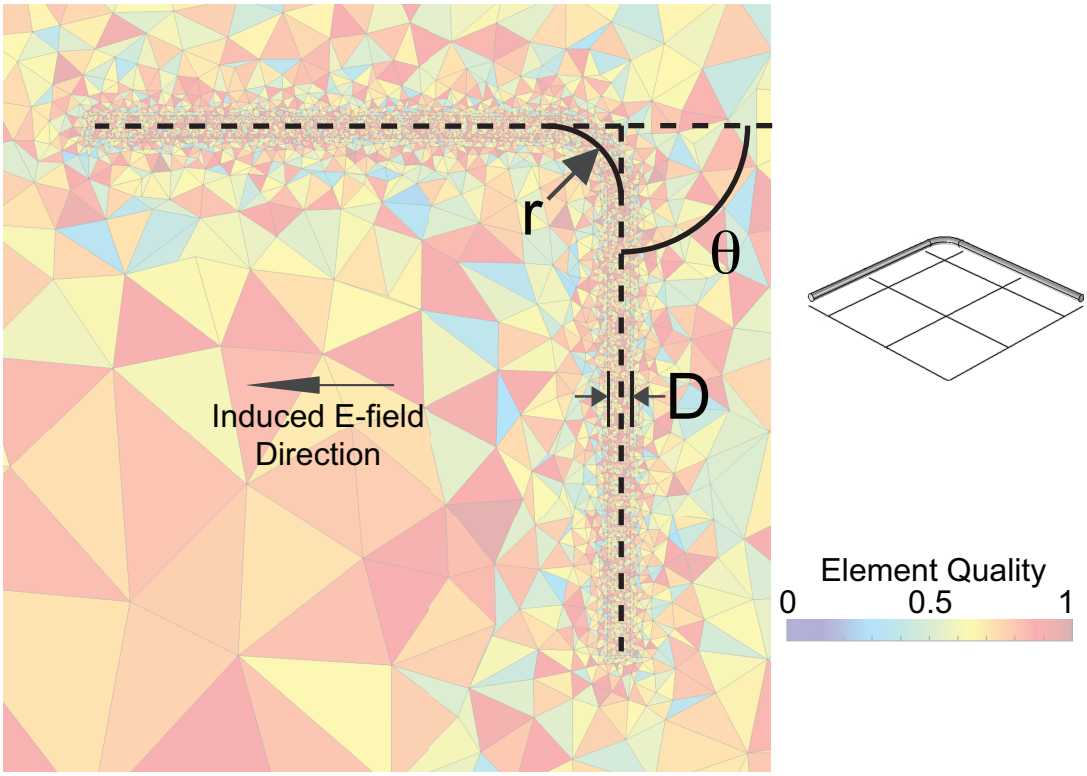

Figure 7 Cross-Section of Bent Axon Segment FEM Mesh. Passive axon segment with θ = 90º bend is shown. Axon diameter and the radius of curvature are 5 µm and 15 µm, respectively. False color map indicates element quality where 1 is an equilateral tetrahedron and 0 is a degenerated tetrahedron. A finer mesh density near the axon was employed to minimize numerical error in and around the axon segment.

A single current dipole source was positioned 500µm above the axon segment. Its magnitude was assigned to mimic that of the monophasic current pulse through a typical TMS coil (8kA). Cylindrical axon geometry was created in COMSOL and then

oriented as shown in Figure 7. The induced E-field was modeled to point in the –*x* direction. Using the Fourier solver, the transmembrane potential was computed in discrete-time throughout the duration of the monophasic stimulus (Figure 6) for various bend angles (θ = 30º, 60º, 90º, 120º, 150º) to obtain a quantitative measure of the effects of axon bending and to attempt to corroborate the theoretical analysis[23] for a time-dependent magnetic stimulus.

vi. Comparison of Induced E-fields from Magnetic and Electrical Stimulation

TMS is often conveyed by analogy to brain stimulation from a current controlled electrode. In order to quantitatively describe the spatial characteristics of the E-field produced by TMS, we compared the field induced by a figure-8 coil to that by an ECS electrode. We scrutinized the E-fields within a plane at a depth of 1cm from the stimulating source. The resulting E-field magnitude from both modes of stimulation is linearly dependent upon the magnitude of the source (current or magnetic field); therefore, normalized units were used.

The E-field produced by the TMS coil was analytically calculated using the validated figure-8 coil model[24]. Since the magnetically induced E-field is independent of conductivity within a semi-infinite, homogenous medium, a conductive medium was not needed in the model. Additionally, the magnetic permeability was assumed to be that of free space ($\mu = \mu_0$) on the basis of previously published work that contains models for TMS in biological tissue (Thielscher et al., 2011).

The E-field produced by the ECS electrode was computed via the finite element method, using an FEM of an electrode (D = 5 mm; thickness = 2 mm) within a

[23] See Theoretical Analysis of the Magnetic Stimulus, p. 40.
[24] See Figure-8 TMS Coil Model Development, p. 34, 54.

homogenous conductive medium having the approximate conductivity of saline (σ = 0.2 S/m). We modeled the ECS system under steady state conditions with an assumption of negligible dielectric effects ($\epsilon = \epsilon_0$). The electrode was modeled as a constant current source (floating potential) and the outermost boundaries of the model were conditioned to zero potential (V = 0; ground).

Physical principles were based on Ampere's law. ECS effectively adds charge to extracellular space, which affects the transmembrane potential. No intracellular charge is added or displaced without membrane channels opening. For ECS, the voltage between any two points is path independent:

$$\Delta V = \int_a^b \mathbf{E} \cdot d\mathbf{s} \qquad \text{(Eq. 11)}$$

For Eq. 11 to be true, it must also be that $\nabla \times \mathbf{E} = 0$. Conversely, in the generalization to electrodynamics, $\nabla \times \mathbf{E} \neq 0$ (see Eq. 4 & 7). Therefore, Eq. 11 is not valid in electrodynamics because ΔV is path dependent. Magnetic stimulation does not add charge into the system, but rather an induced EMF is exerted on existing charge in extracellular space and intracellular space.

Our objective was to gain insight into the relatedness between magnetic and electric stimulation by answering the question: Are electric and magnetic stimulation analogous?

vii. Development of Pyramidal Cell Model

We adapted the pyramidal cell model published by Amatrudo et al. (2012) for the purpose of modeling TMS experiments. This model was made publicly available on

ModelDB[25]. Amatrudo et al. (2012) constructed this model by performing a high-resolution 3D morphometric analysis from a layer 3 pyramidal cell within the left dorsolateral prefrontal cortex (dlPFC) of the monkey. This particular model was selected for use in TMS for four main reasons:

1) The hypothesis that TMS has immediate and direct effects on pyramidal cell neurons is well supported (Arias-Carrión, 2008; Di Lazzaro et al., 2008). This could be due to the large density of excitatory post-synaptic connections compared to other neurons in cortex. Also, evidence exists that direct targets of activation are subcortical descending axons (Burke et al., 1993; Nowak & Bullier, 1998).
2) The model's size is representative of pyramidal cells anterior the central sulcus. Amatrudo et al. (2012) show modeled reconstructions of 10 neurons (5 from visual cortex (V1) and 5 from dlPFC) with an analysis of size vs. presence in cortical areas.
3) The biophysical structure and electrical properties of the model were gathered from experimental data and imaging. The structural integrity of the pyramidal cell is paramount since activation from TMS depends on the shape of neural elements.
4) It was built and coded in a well-established neuron modeling environment (NEURON) and was made readily available for customization through ModelDB[25].
5) A 20 mm synthetic axon (Mainen et al., 1995) was added, which includes an axon hillock, initial segment, and 200 sections of myelin and nodes of Ranvier. Cellular electrical parameters (space constants, time constants, etc.) were obtained by Amatrudo et al. (2012) for passive and active membrane properties. Neuron compartments were tuned to have H-H style kinetics by physiological current-voltage

[25] A database of published neuron models that were built in the NEURON environment. See http://senselab.med.yale.edu/modeldb/.

relations (Mainen et al., 1995). The final multicompartmental model contains 1392 compartments (Figure 8).

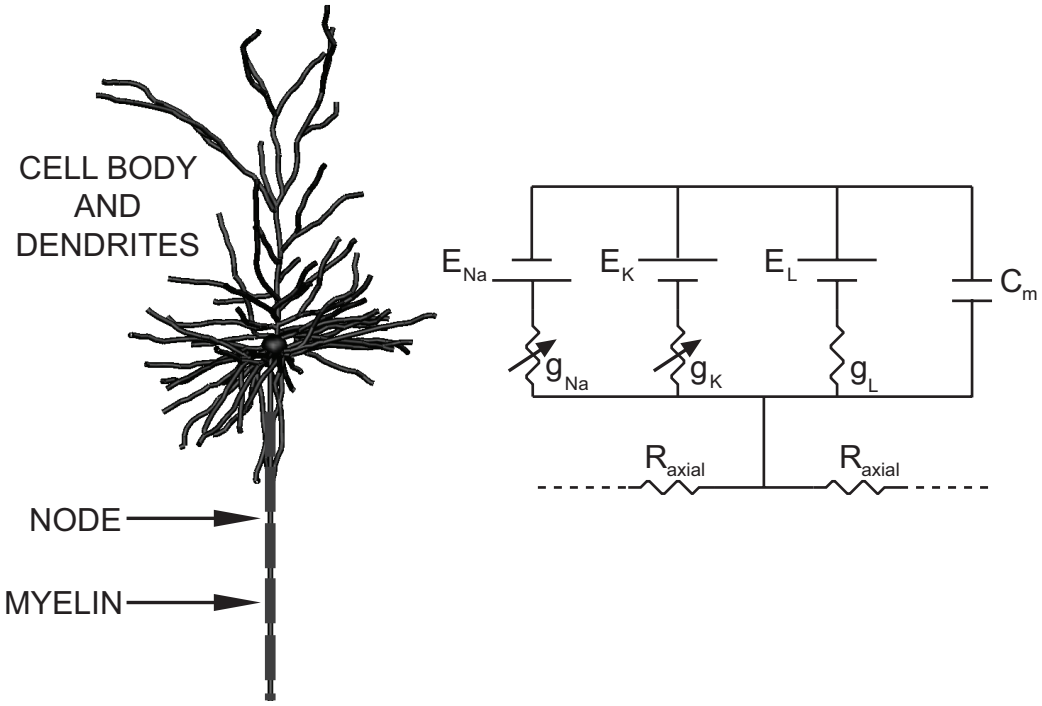

Figure 8 Pyramidal Cell Model Structure and Circuit Model. Cell body and dendritic tree of dlPFC pyramidal cell model created by Amatrudo et al. (2012). A synthetic axon was added. Single compartment circuit model describing ionic channel conductances and Nernst potentials are shown.

Ionic currents of the compartment model have the general form of

$$I_{ion} = g_{ion}(v,t)\left(v - \mathcal{E}_{ion}\right) \quad \text{(Eq. 12)}$$

where v is the intracellular potential, $\mathcal{E}_{ion}$ is the Nernst potential of the potential from the ion gradient, and $g_{ion}(v,t)$ is the conductance of the ion channel. The ion conductance is generalized by the maximum conductance ($\overline{g_{ion}}$) multiplied by gating variables (ϱ) that range between 0 and 1.

$$g_{ion}(v,t) = \overline{g_{ion}}\varrho \quad \text{(Eq. 13)}$$

By virtue of the rate constants (α, β), gating variables are voltage- and time-dependent.

$$\tau_\varrho = \frac{1}{\alpha_\varrho + \beta_\varrho}$$

$$\frac{d\varrho}{dt} = \alpha_\varrho(1-\varrho) - \beta_\varrho\varrho = \frac{\left(\varrho_\infty - \varrho\right)}{\tau_\varrho} \quad \text{(Eq. 14)}$$

Due to the nonlinear nature ion channels, neuron models are inherently computational. Simulations were performed within the NEURON environment[26]. Gating variables describe the fraction of ion channels within a membrane patch that are open at any time, t. The opening of the ion channels relieves the membrane of the diffusion gradient and causes graded potentials or action potentials described by depolarization preceding hyperpolarization. The values of the activation (α) and inactivation (β) parameters are described below for the two membrane mechanisms implemented in this pyramidal cell neuron.

Potassium (K) channel kinetics

The ion channel current depends on the max conductance ($\overline{g_K}$) and its gating variable (n),

$$I_K = \overline{g_K} n\left(v - \mathcal{E}_K\right) \quad \text{(Eq. 15)}$$

and the rate constants α and β (units of $[\mathrm{ms}^{-1}]$):

[26] NEURON script is written in a custom (and perhaps esoteric) programming language called "hoc", or "high order computing" code. NEURON also works well with ion channel mechanisms built within other environments such as GENESIS (GEneral NEural SImulation System; www.genesis-sim.org/GENESIS/).

$$\alpha_n = \frac{0.02[\mathrm{ms}^{-1}](v - 25[\mathrm{mV}])}{\left(1 - \exp\left(-\frac{(v-25[mV])}{9[\mathrm{mV}]}\right)\right)}$$

$$\beta_n = \frac{-0.002[\mathrm{ms}^{-1}](v - 25[\mathrm{mV}])}{\left(1 - \exp\left(\frac{(v-25[\mathrm{mV}])}{9[\mathrm{mV}]}\right)\right)} \qquad \text{(Eq. 16)}$$

$$\tau_n = \frac{1}{\alpha_n + \beta_n}$$

$$n_\infty = \alpha_n \tau_n$$

The units for the terms are included in Eq. 16 and are consistent throughout.

Sodium (Na) channel kinetics

The ion channel current for sodium is

$$I_{Na} = \overline{g_{Na}} m^3 h\left(v - \mathcal{E}_{Na}\right) \qquad \text{(Eq. 17)}$$

and the rate constants for gating variable *m*,

$$\alpha_m = \frac{0.182(v + 35)}{1 - \exp\left(-\frac{v+35}{9}\right)}$$

$$\beta_m = \frac{0.124(v - 35)}{1 - \exp\left(-\frac{v-35}{9}\right)} \qquad \text{(Eq. 18)}$$

$$\tau_m = \frac{1}{\alpha_m + \beta_m}$$

$$m_\infty = \alpha_m \tau_m$$

and the rate constants for the gating variable *h*.

$$\alpha_h = \frac{0.024(v+50)}{1-\exp\left(-\frac{v+50}{5}\right)}$$

$$\beta_h = \frac{0.0091(v-75)}{1-\exp\left(-\frac{v-75}{5}\right)} \quad \text{(Eq. 19)}$$

$$\tau_h = \frac{1}{\alpha_h + \beta_h}$$

$$h_\infty = \frac{1}{1+\exp\left(\frac{v+65}{6.2}\right)}$$

Table 3 Pyramidal Cell Model Parameters.

	Soma and Dendrites	*Myelin*	*Axon Hillock and Initial Segment*
$gbar_{Na}$ (mS/cm^2)	105	105	105000
E_{Na} (mV)	60	60	60
$gbar_K$ (mS/cm^2)	115	0	1916.7
E_K (mV)	-90	-90	-90
C (uF/cm^2)	1	0.04	1
E_L (mV)	-69	-69	-69
g_L (mS/cm^2)	0.038	0.038	0.038
R_{axial} (Ω-cm)	150	150	150

Strength-duration Relationships

Strength-duration relationships for the model were obtained from three stimulation paradigms: 1) intracellular stimulation via somatic current injection, 2) extracellular stimulation via ECS electrode, and 3) magnetic stimulation via a 90 mm diameter circular coil.

Strength-duration relationships were quantified by rheobase (the threshold stimulus amplitude required to initiate an action potential with an infinitely long stimulus pulse) and chronaxie (the stimulus duration where the threshold stimulus amplitude is 2x

rheobase). This analysis was performed using well-established methods for electrical and magnetic stimulation of nervous tissue (Chronik & Rutt, 2001; Holsheimer et al., 2000; McIntyre et al., 2004; Recoskie et al., 2009). We developed a custom NEURON script to search for the stimulus threshold for any stimulation paradigm. This script allows for customizing the stimulus duration, stimulus waveform shape, cell state (resting state, active state, passive state, etc.), and cell activity.

For intracellular current injection (Malmivuo & Plonsey, 1995), the shape of the strength-duration curve follows

$$I_s = \frac{I_{rh}}{1 - e^{-\frac{t}{\tau}}} \quad \text{(Eq. 20)}$$

where I_s is the stimulus current threshold having a duration of *t* for a membrane having a time constant, τ, and a rheobasic current, I_{rh}. For extracellular electrical stimulation, the strength-duration follows the general relation

$$V_s \geq V_r \left(1 + \frac{\tau_c}{t}\right) \quad \text{(Eq. 21)}$$

where V_s is the stimulus strength required for membrane activation, V_r is the rheobase threshold, τ_c is chronaxie, and t is the stimulus duration. Equation 21 is the generalization for the strength-duration relationship. The shape of the strength-duration curve follows an exponential relationship from Eq. 20.

The magnetic strength-duration relationship is derived from the E-field strength-duration equation (Recoskie et al., 2009).

$$E_s \geq E_r \left(1 + \frac{\tau_c}{t}\right) \quad \text{(Eq. 22)}$$

Equation 22 is then reformed for magnetic stimulation by the following proportionalities.

$$|\mathbf{E}| \propto \frac{d|\mathbf{B}|}{dt}$$

$$|\mathbf{B}| \propto I_{coil} \qquad \text{(Eq. 23)}$$

$$\frac{d|\mathbf{B}|}{dt} \propto \frac{dI_{coil}}{dt}$$

The strength-duration relationship[27] for magnetic stimulation from a TMS coil can be written as

$$\Delta I_s \geq \left(\frac{dI_{coil}}{dt}\right)_{min} \tau + \Delta I_{min} \qquad \text{(Eq. 24)}$$

where ΔI_s is the rise in coil current over a time τ required for suprathreshold stimulation, the bracketed term is the minimum rate of change of the coil current at the upper limit of the coil current I_{coil} that causes stimulation, and ΔI_{min} is the minimum current rise at the upper limit of the current rise rate ($(dI_{coil}/dt)_{max}$) that causes stimulation. Chronaxie can be determined directly from threshold parameters by

$$\tau_c = {\Delta I_{min}}\Big/{\left(\frac{dI_{coil}}{dt}\right)_{min}} \qquad \text{(Eq. 25)}$$

where the numerator has units of [A] and the denominator has units of [A/s]. Equations 24 and 25 are normally applied when the induced eddy currents are unknown. In order to compare magnetic with electric stimulation and since the E-field is not unknown, Eq. 22 was employed to determine strength-duration relationships.

Chronaxies from three experimental setups were determined for the purpose of comparison (Figure 9). Magnetic chronaxie was determined by modeling the approach similar to that employed by Basser and Roth (1991). Magnetic chronaxie was determined via a current-controlled circular stimulating coil. This coil is similar to TMS

[27] See Appendix B, p. 159, for derivation.

circular coils having 9 windings, a 90 mm diameter, and a maximum current delivery of 8 kA. The coil was assumed to have a maximum rise time of 100 μs with an adjustable maximum current output. The pyramidal neuron was oriented in such a way that its axon lies in-plane with the circling E-field (Figure 9A). Chronaxie from extracellular electrical stimulation was obtained by modeling the scalar potential field produced a voltage-controlled ECS electrode having cylindrical geometry (D = 5 mm). The pyramidal cell was placed 1 cm below the plane of the ECS electrode and oriented such that the axon lies within a plane parallel to the bottom of the electrode (Figure 9B).

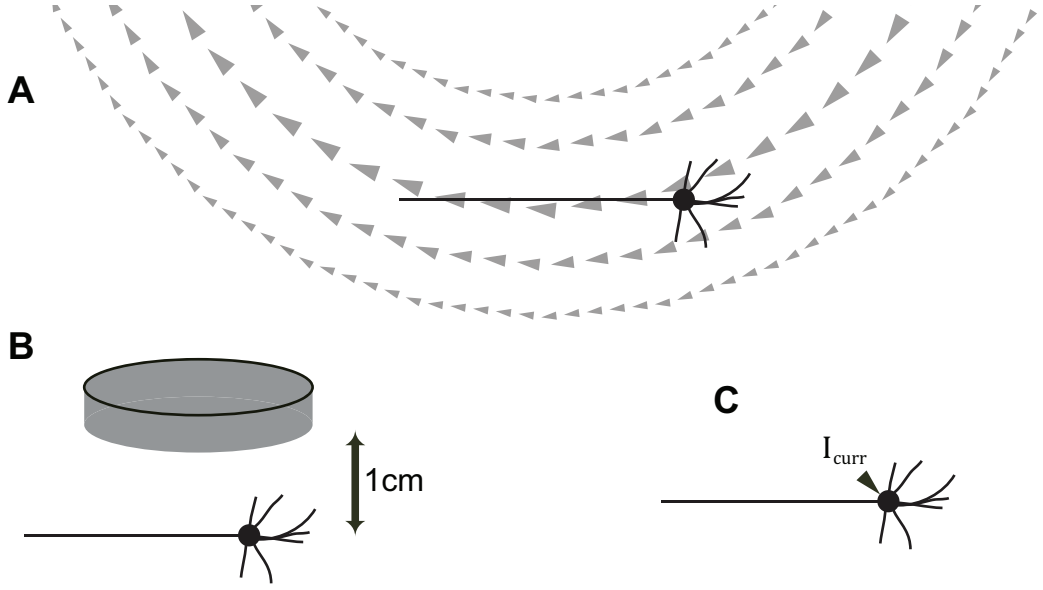

Figure 9 Strength-duration Experimental Setup. Strength-duration curves were obtained under three conditions shown in (A), (B), and (C). (A) Pyramidal cell is shown oriented within the induced E-field (concentric arrows) from magnetic induction at a depth of 1cm. (B) Pyramidal cell orientation relative to ECS electrode (D=5mm). (C) Pyramidal cell is shown under somatic current injection.

These excitability characteristics would not be obtainable in-vitro without stimulation hardware that has modifiable stimulus waveform parameters. Only through modeling can a magnetically induced E-field have a semi-infinite duration.

Activation Threshold Relative to Membrane Potential

We tested the Edgley et al. (1990)[28] hypothesis using the same setup illustrated in Figure 9A with magnetic waveforms as produced by Magstim stimulator units. We then examined the threshold to activation relative to varying membrane potentials within the cell body. In order to raise the membrane potential above resting state, varying degrees of sub-rheobase current injection within the soma were modeled. The current injection was relieved at the time of the magnetic stimulus and the intracellular voltage was recorded to evaluate the relationship between membrane potential at the time of the stimulus and stimulation threshold. Both the monophasic and biphasic magnetic stimulus pulses were tested.

Our objective for Specific Aim 1 was to develop a working single-cell model of a pyramidal cell for experimentation in TMS to gain new insights into neural response variability as well as possible mechanisms of activation during TMS.

RESULTS

i. Figure-8 TMS Coil Model Development

We created an analytical model of the figure-8 TMS coil to estimate the electromagnetic fields generated by current flow through its windings. E-field calculations were compared with those of the Salinas et al. (2007) validated model based on in-vitro magnetic field measurements; the custom coil model was found to produce E-fields comparable to those predicted by Salinas et al. with little discrepancy (Figure 10). E-field vectors and magnitude maps (Figure 11) were found to match those by Walsh and Pascual-Leone (2005, p. 59). The coil model produced a magnetic flux of 2.09 T directly

[28] Edgley et al. (and many others) surmise that a contributing factor to the variability observed from TMS is related to the membrane potential at the time of stimulus.

underneath the coil, which agrees with published in-vitro measurements of 2.0T (Jalinous, 1998).

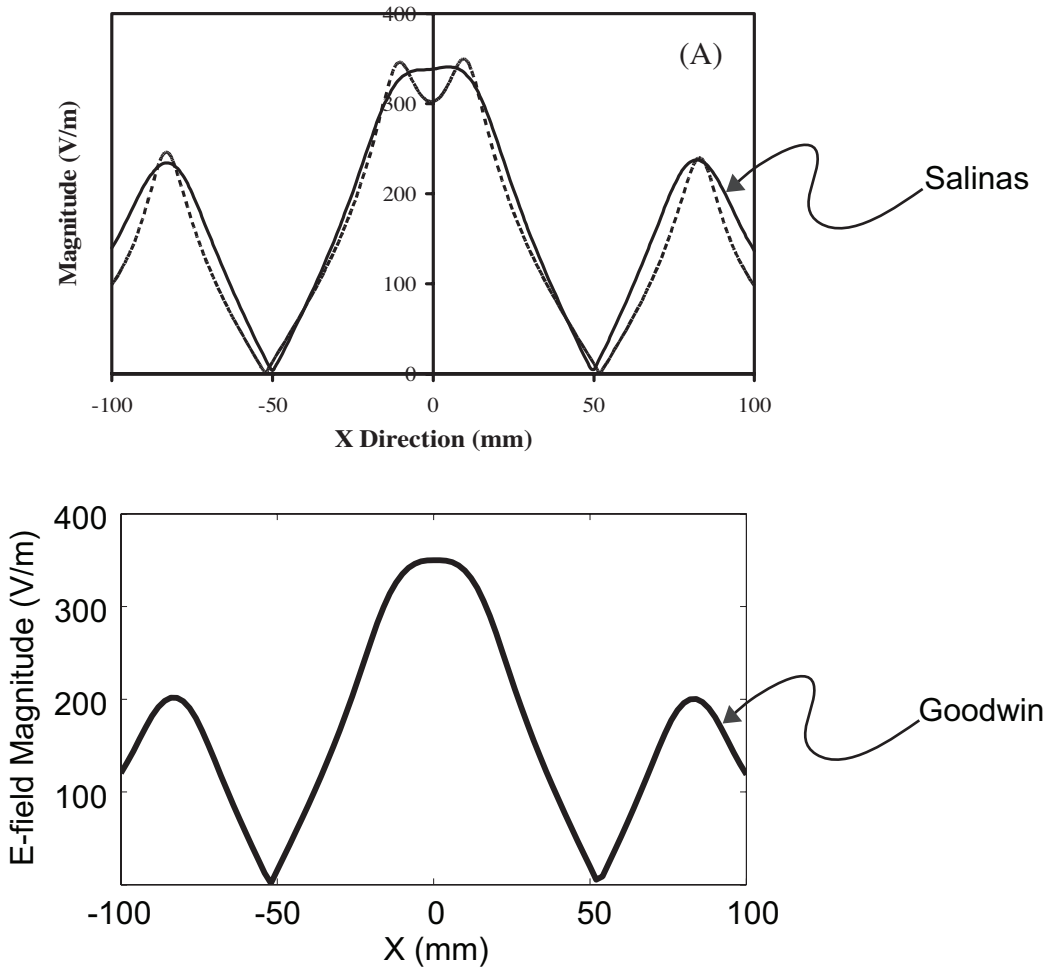

Figure 10 Coil Model Validation. E-field calculations from the model (bottom) in this study are compared with those from Salinas et al. (2007) (top, solid line) where the coil current rise time is assumed 100 μs at 100% intensity. The top plot was copied from Figure 5A in Salinas et al. (2007) for the purpose of comparison. Plots show E-field calculations along an evaluation line 3.5mm below the plane of the coil along the width dimension of the figure-8 coil (x-axis). (*Top plot used with permission from Salinas et al., 2007*.)

Our model predicted electromagnetic fields as expected from Maxwell's equations[29]. The induced E-field followed streamlines that were concentric with the coil turns (Figure 11). Induced currents were found to flow in the opposite direction of the current through the coil according to Maxwell's equations.

[29] See Appendix A, p. 158.

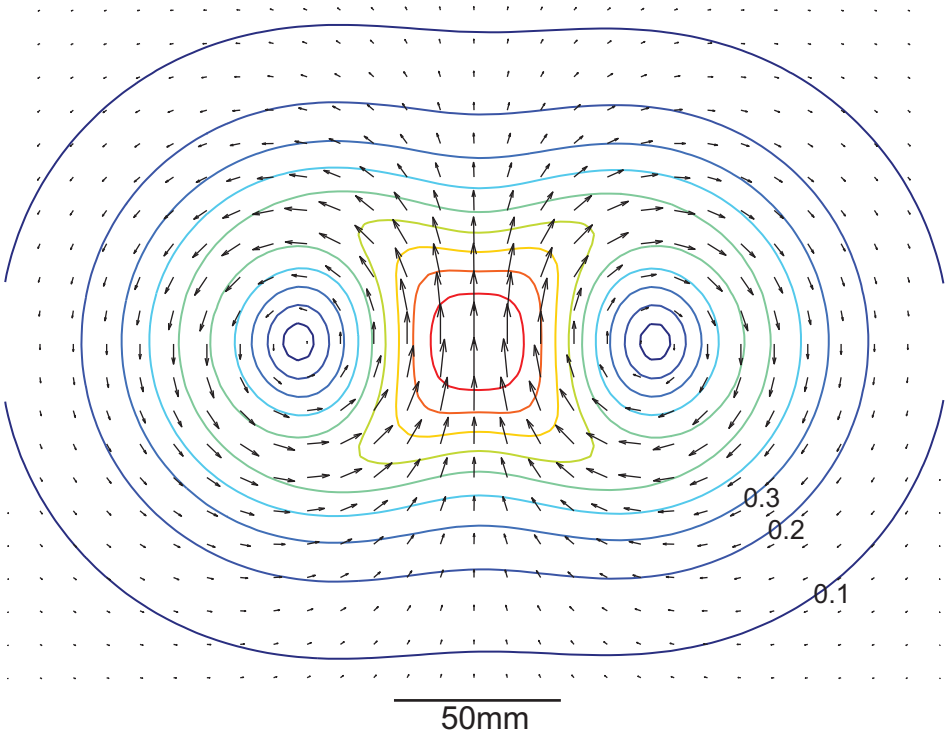

Figure 11 Induced E-field Vectors and E-field Magnitude Contour Map. Induced E-field vectors and relative E-field magnitude contour lines on a plane 1 cm below the plane of the figure-8 TMS coil. Dark red line indicates 0.9 of the max E-field magnitude.

The measured EMF matched the waveform characteristics (Figure 12) specified by the manufacturer in terms of the rise time, duration, and shape (Jalinous, 1998; Walsh & Pascual-Leone, 2005). The actual current through the TMS coil could not be recorded due to the hardware casing around the stimulator unit. For this reason, the actual current was modeled by normalizing the measured waveforms and scaling them according to manufacturer specifications to enable prediction of the absolute induced fields. The shape of the current waveform through the coil was calculated post-hoc by integrating the EMF record (Figure 12).

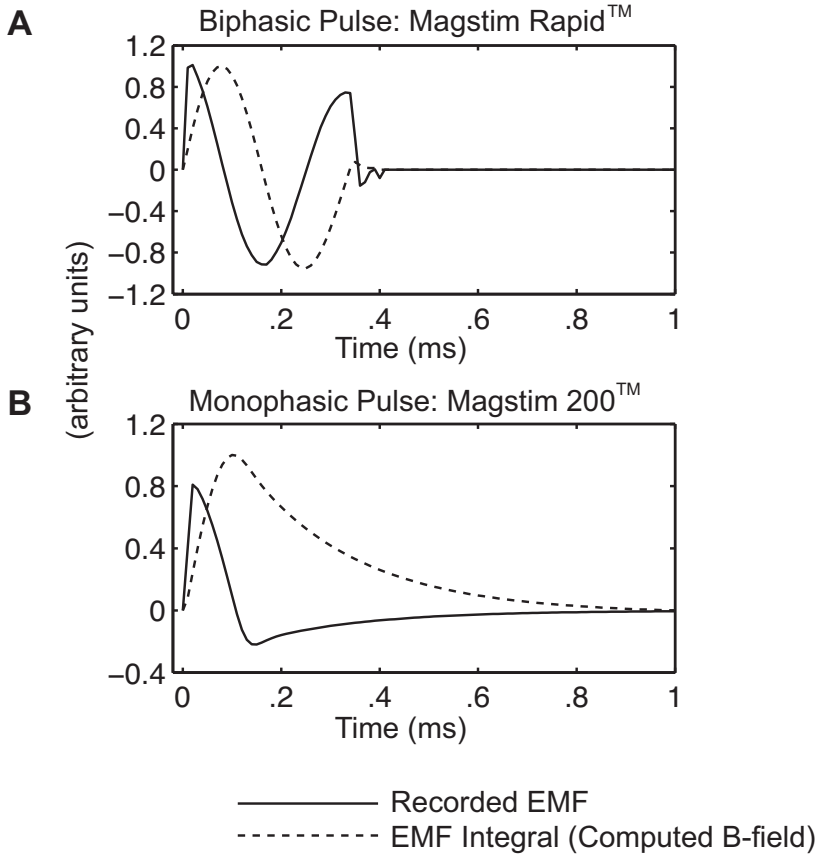

Figure 12 In-vitro Recording of TMS Stimulus Waveform. In-vitro EMF records for both the biphasic (A) and monophasic (B) TMS stimulus. The actual current waveform ($\propto$ B-field) was found indirectly by computing the integral of the Recorded EMF.

ii. Time Dependencies: Fourier Solver vs. Single-frequency Approximation

Our Fourier Solver produced the expected stimulus waveform according to Maxwell's equations (Figure 13C & D) and according to published work describing TMS (Walsh & Pascual-Leone, 2005, p. 41-8). Comparisons were made with previously published E-field modeling methodologies applied for TMS (Figure 13B). The previously published approaches assume single-frequency conditions by simplifying the time-dependent pulse to a signal with one frequency component (Figure 13B).

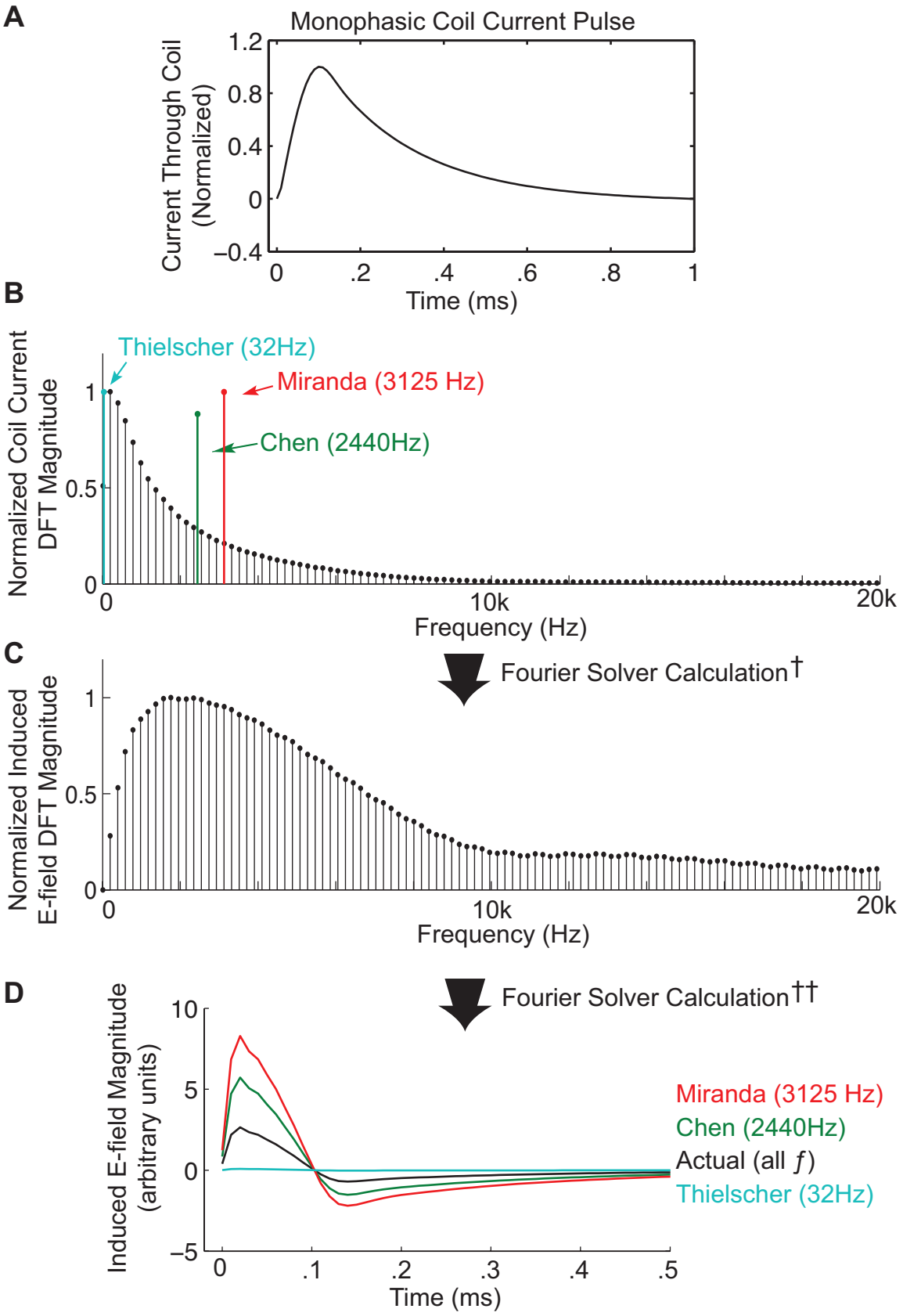
A
Monophasic Coil Current Pulse
Current Through Coil (Normalized)
1.2
0.8
0.4
0
−0.4
0
.2
.4
.6
.8
1
Time (ms)
B
Normalized Coil Current DFT Magnitude
Thielscher (32Hz)
Miranda (3125 Hz)
Chen (2440Hz)
1
0.5
0
0
10k
20k
Frequency (Hz)
C
Fourier Solver Calculation†
Normalized Induced E-field DFT Magnitude
1
0.5
0
0
10k
20k
Frequency (Hz)
D
Fourier Solver Calculation††
Induced E-field Magnitude (arbitrary units)
10
5
0
−5
0
.1
.2
.3
.4
.5
Time (ms)
Miranda (3125 Hz)
Chen (2440Hz)
Actual (all f)
Thielscher (32Hz)

Figure 13 Time-dependent Analysis with Fourier Solver. Calculation steps of the custom Fourier solver to obtain the resulting induced E-field from a monophasic TMS pulse (A). (B) The DFT of the TMS pulse is calculated, (C) the E-field is calculated in the frequency domain, and (D) the inverse DFT is calculated to obtain the resulting waveform in time. Approximations from previously published approaches have been included for the purpose of comparison with the Fourier Solver calculation (Actual).
† The Fourier Solver was designed specifically for use in the finite element method. Here, the electromagnetic equations are solved at every frequency in the spectrum of (B). The result is a discrete Fourier series of the E-field from magnetic induction.
†† The time-dependent solution is found by calculating the inverse DFT of the discrete Fourier series in (C). The actual induced E-field was calculated via the Fourier Solver, which was compared with the results from the approach of other investigators (Jalinous, 1998; Walsh & Pascual-Leone, 2005).

We compared the results from the Fourier Solver with those reported from single-frequency assumptions. (This approach results in an oscillating E-field at a single frequency, not a transient E-field as shown in Figure 13D.) The single-frequency approximations were manually transformed to the shape of the TMS pulse for the purpose of comparison with the Fourier Solver solution (Figure 13D, *Actual*). The Fourier Solver produced a theoretical solution to the time-dependent problem by computing the solution within the spectrum of the TMS waveform (0-100kHz) at a negligible computational cost.

The time-dependent E-field calculations differed significantly (percent difference of 115% to Chen and Mogul, 2009 and 213% to Miranda et al., 2003) from studies that reduce the monophasic stimulus pulse to a single-frequency sinusoid (Figure 13D). These results suggest that a single frequency component is a poor representation of the actual coil current pulse, and the Fourier Solver is a viable method to estimating the actual induced E-field in discrete-time for any TMS waveform.

iii. Conceptualizing Barker's Activating Function

According to the activating function, f, an axon exposed to threshold stimulus would be expected to depolarize where f is maximum. We performed a theoretical analysis to provide a framework for understanding how excitation occurs from magnetic

stimuli. The analysis of the activating function confirmed modeled axon responses measured by Basser (1994) and B. J. Roth and Basser (1990).

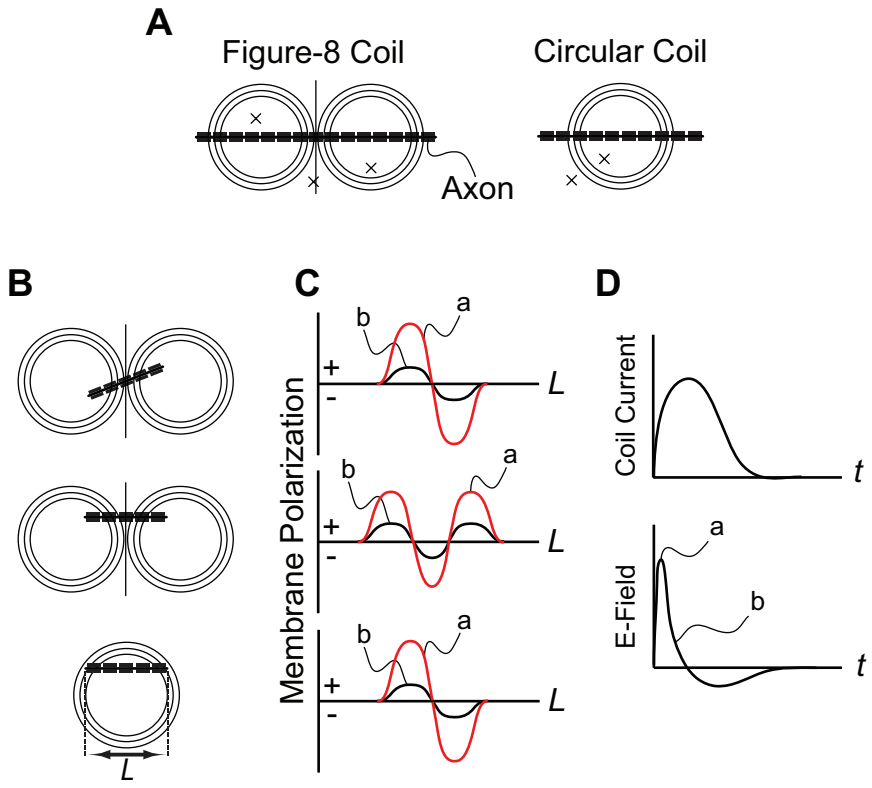

Figure 14 Activating Function of Hypothetical Axon. (A) The E-field lines of two widely used coil shapes in TMS are illustrated relative to hypothetical axons ("×" indicates an axon oriented normally to the plane of the page) that experience no activation regardless of E-field intensity, i.e., f is 0 everywhere along the axis of each axon. (B) Different orientations of a straight axon relative to a TMS coil are shown with their corresponding activating function plots (C) along the length, L, of the axon. (C) Activating function plots are illustrated for the adjacent axon orientation in (B). Lines labeled "a" and "b" correspond to different time points during the TMS pulse (see (D)). (D) Monophasic TMS pulse and the induced E-field in time where time points "a" and "b" occur at <20 μs and 90 μs, respectively.

Certain distinct orientations of an axon could yield no activation (Figure 14A) according to Eq. 6, specifically, f = 0 along axons oriented perpendicular to E-field lines. Otherwise, due to the nonhomogenous E-field, f was found be non-zero in any other orientation.

The f value does not contain time-dependent terms (Eq. 6). The f value provided a valuable basis for understanding mechanisms of TMS but it was an oversimplification of the effects of TMS even though it has been employed for such

evaluations (Opitz et al., 2011; Silva et al., 2008). A more in-depth assessment of the excitability of an axon in an E-field would require a strength-duration analysis and time-dependent models.

iv. Theoretical Analysis of the Magnetic Stimulus

Based on Ampere's current conservation law (Eq. 8), the axial current played a role in initiating membrane polarizations. The magnitude of the current induced in intracellular space depends on the axial component of the induced E-field (Figure 15). Given the scenario defined in Figure 15A, the maximum axial current occurs where the induced E-field is collinear with the axon axis. Therefore, the axon bend was found to cause attenuated E-fields giving rise to distinct, concentrated increases in intracellular charge (ρ) to occur at the bend.

$$d\rho/dt = -\nabla \cdot \mathbf{J} \qquad \text{(Eq. 26)}$$

This charge build-up near the axon bend leads to membrane polarization, which, if above threshold, would give rise cell activation.

The monophasic pulse created a single abrupt polarization across the cell membrane in a bent axon (Figure 15B), and the biphasic stimulus elicited three consecutive membrane polarizations that are similar in magnitude but differ in direction (Figure 15C).

These results suggest that a similar effect in neuronal sections where there is a change in neurite[30] diameter (Figure 16). This phenomenon would be expected to occur in dendrites or near synapses. Axons having a constant diameter (e.g., myelinated axons) can be polarized only at bends.

---

[30] A "neurite" is any projection of the cell from its cell body (e.g. dendrites, axons, etc.).

As demonstrated, the activating function is limited to cylindrical neural elements with a constant diameter. In axons with a constant diameter, the results confirm the activating function (Walsh & Pascual-Leone, 2005). These findings demonstrate the electrical forces exerted by a stimulus waveform on ion channels within a bend. However, Ampere's law alone cannot explain biophysical effects of the monophasic and biphasic waveform on the membrane ion channels. Furthermore, these results cannot describe the threshold stimulus or the cellular response.

The theoretical analysis provided an explanation of the one mechanism of activation within an axon that is consistent with Barker's activation function. Furthermore, Ampere's law offered a viable framework for answering questions related to the cellular response from a stimulus.

v. The Response of a Passive Cylindrical Axon to a Monophasic Stimulus

Finite element methodology was employed to model a bent axon in the presence of a time-varying magnetic field. The bend angle (θ) of the axon was varied and the effects were evaluated. The resulting transmembrane potential was compared to predictions based on Ampere's law of current conservation (Figure 15). The results suggest that an isolated axon experiences a stimulus along the full length of the membrane, but is intensified at bends.

The induced E-field gave rise to membrane hyperpolarization for all bend angles at t = 50 μs (Figure 17C). Evaluation lines around the bend (Figure 17A, dotted lines) yielded unequal transmembrane voltages on opposite sides of intracellular space (Figure 17B & C). Maximum membrane hyperpolarization was found near the axon bend (cf. Figure 15C, *middle*). Hyperpolarization occurs on both sides of the cell membrane, but differs in magnitude. The membrane voltage response followed the shape of the

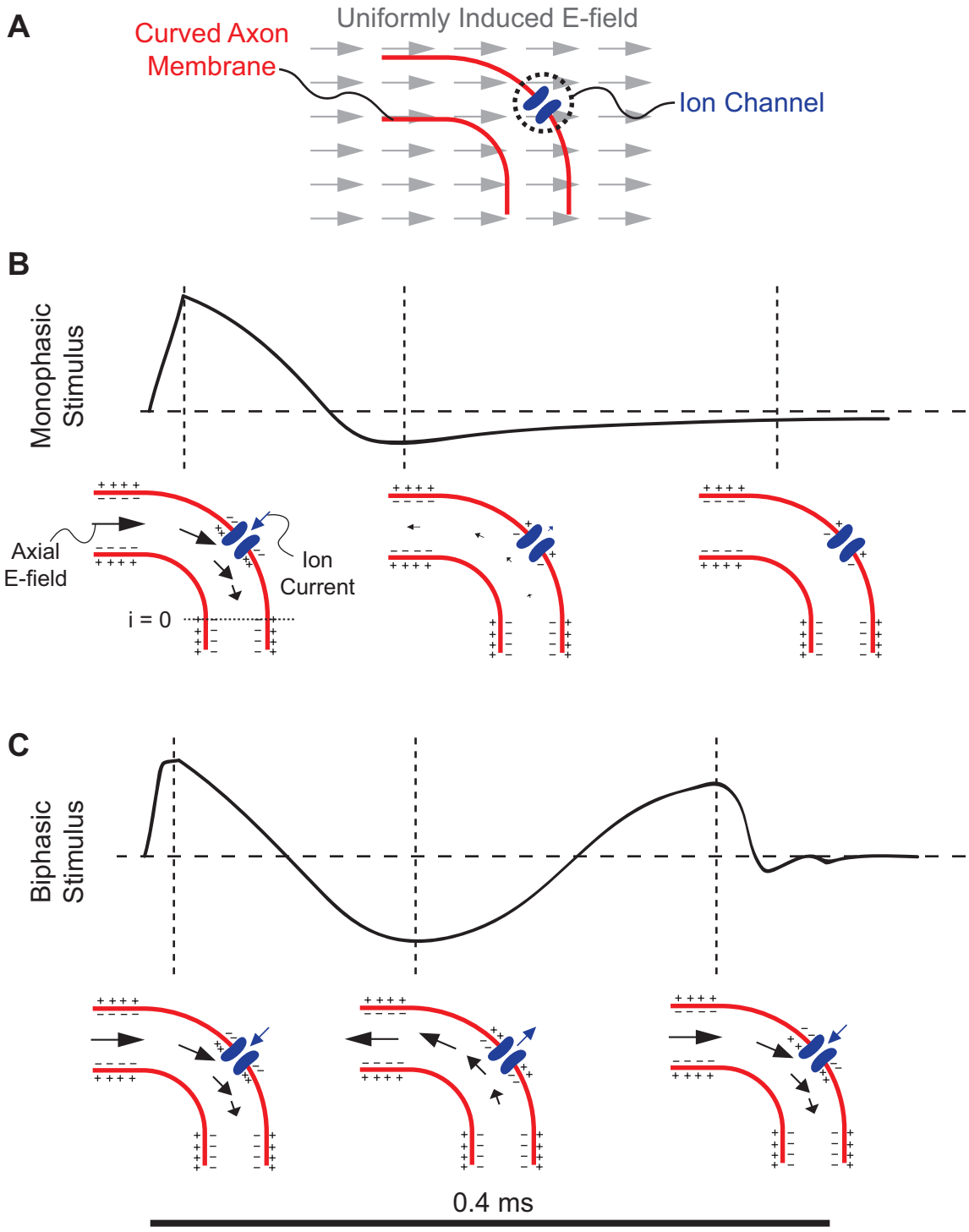

Figure 15 Cross-section of Single Membrane Compartment in a Curved Axon Within Uniformly Induced E-field. Ampere's law of current conservation for an E-field induced within intracellular space has been modeled for the monophasic (B) and biphasic (C) stimulus. (A) For exemplary purposes, the induced E-field was assumed uniform around an axon with a 90º bend. (B & C) Black arrows indicate induced electric currents and blue arrows describe the driving force of ionic currents arising from membrane polarization. Vertical dotted lines mark the time points for the corresponding illustrations directly underneath.

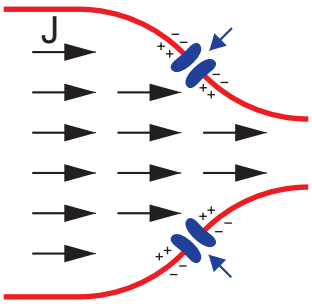

Figure 16 Charge Conservation at Diameter Change. Ampere's law of charge conservation applied to an axon having a change in diameter in the presence of a parallel E-field. Resulting axial current (**J**) decreases with decreasing diameter. This phenomenon is not detected by the activating function.

monophasic stimulus with a phase delay. For a bend angle of θ = 90º (Figure 17B), transmembrane voltage has an increasing phase delay with an increasing evaluation line number on the side of the bend having the greatest surface area (Figure 17A, *red points*). However, this phase delay is not present on the opposite membrane (Figure 17A, *green points*). The existence of a phase delay can be attributed to the capacitive properties of the membrane. This phase difference in the transmembrane potential (Figure 17B; *red* vs. *green* traces) is likely due to the larger surface area on the outside of the bend.

The magnetic stimulus was found to induce non-uniform potentials along the circumference of the membrane cross section. The transmembrane potential varied along the axon axis and around its circumference (Figure 17C). These variations were especially apparent with greater axon bend angles. The direction of the E-field played a significant role in membrane polarization during a magnetic stimulus. Bent axons experienced increased polarization with increasing bend angles. Importantly, these findings support predictions based on a theoretical approach (cf. Figure 15 & Figure 16).

Axial models such as the activating function cannot account for the asymmetric activation of ion channels around the axis of an axon (Figure 14). However, an axial

model would capture the net effect of the stimulus on all channels within or near the axon bend. Therefore, a model of this detail is unneeded in order to describe loci of activation along the axial direction of an axon.

vi. Comparison of Induced E-fields from Magnetic and Electrical Stimulation

We compared the induced E-field produced by a figure-8 TMS coil with that produced by an ECS electrode (D = 5 mm), and the magnetically induced E-field was analytically computed using the figure-8 coil model. The E-field produced by a current-controlled ECS electrode was computed within COMSOL using the finite element method. The E-field magnitude was plotted on a line (L = 40 mm) positioned 10 mm below the plane of each source (coil and electrode) (Figure 18).

The ECS E-field was axisymmetric whereas the E-field from the TMS coil was symmetric only about the x-axis (or xz-plane) (Figure 19). At a depth of 10 mm, the area containing at least 80% of the maximum E-field for magnetic stimulation was 15.9 sq-cm (Figure 19, *0.8 contour*) and the ECS counter-part (Figure 18 and Figure 19, *dotted-line*) was 1.2 sq-cm (13.2x smaller).

These results suggest that ECS is not analogous to TMS. E-field calculations demonstrate large differences in E-field distribution between TMS and ECS. At 10 mA delivery, the ECS electrode produced a maximum E-field of 26 V/m (depth of 10 mm). At the same depth, the TMS coil to produced a maximum E-field of 432 V/m from a max-intensity monophasic stimulus. Though the E-field delivered by the figure-8 coil is greater in magnitude, its E-field gradient magnitude was lesser than that from ECS.

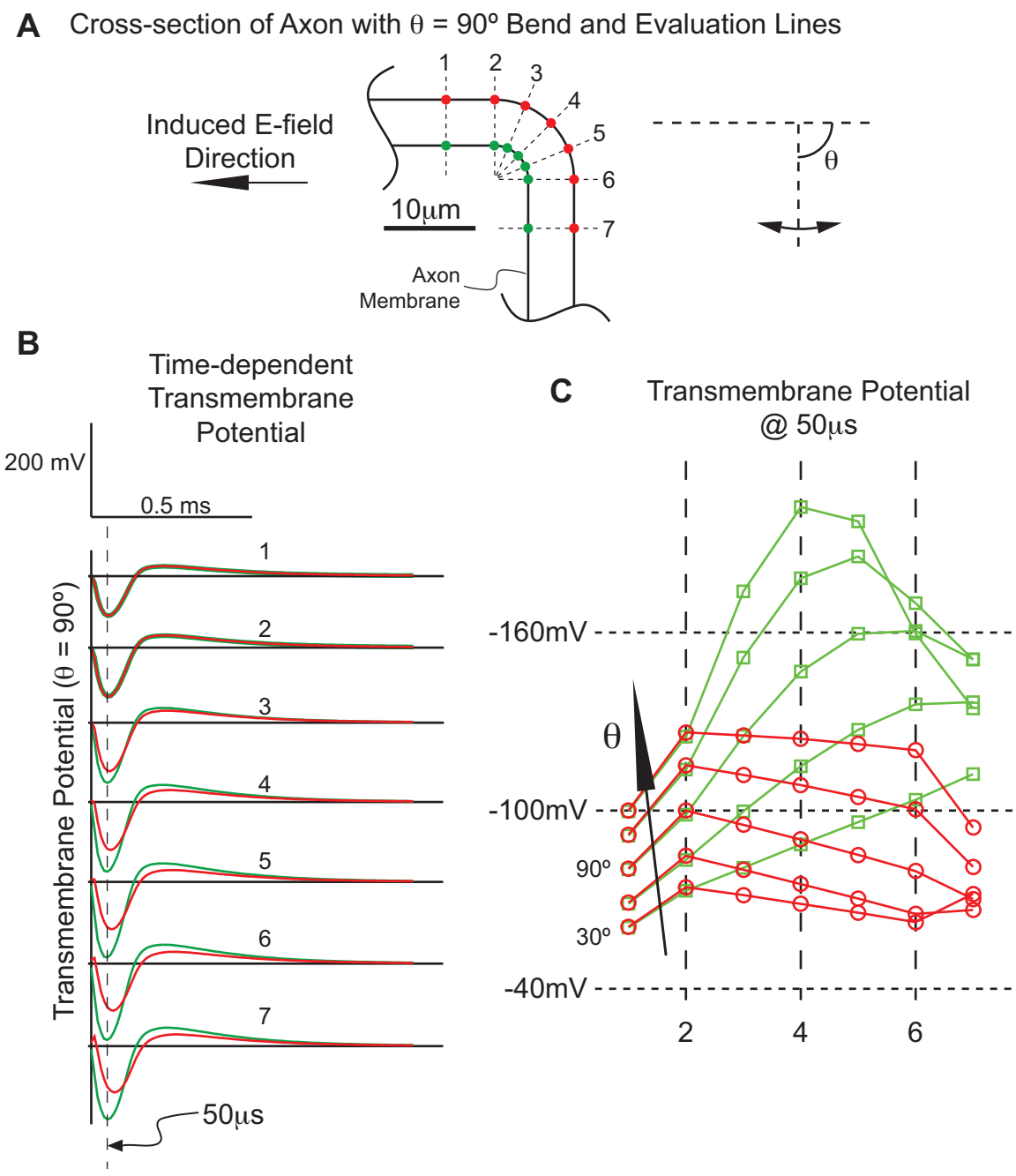

Figure 17 Transmembrane Potential at the Bend in Axon FEM Model. Transmembrane potential was computed relative to extracellular space. (A) Axon schematic with a right-angle bend (θ = 90º) and evaluations lines 1-7 is shown relative to the direction of the induced E-field. The transmembrane potential was evaluated at the red and green dots. The angle convention is also shown. (B) Resulting transmembrane potential for θ = 90º at each evaluation point during a monophasic magnetic stimulus. (C) The transmembrane potential at evaluation points (dotted vertical lines) at time t = 50 μs as indicated in (B).

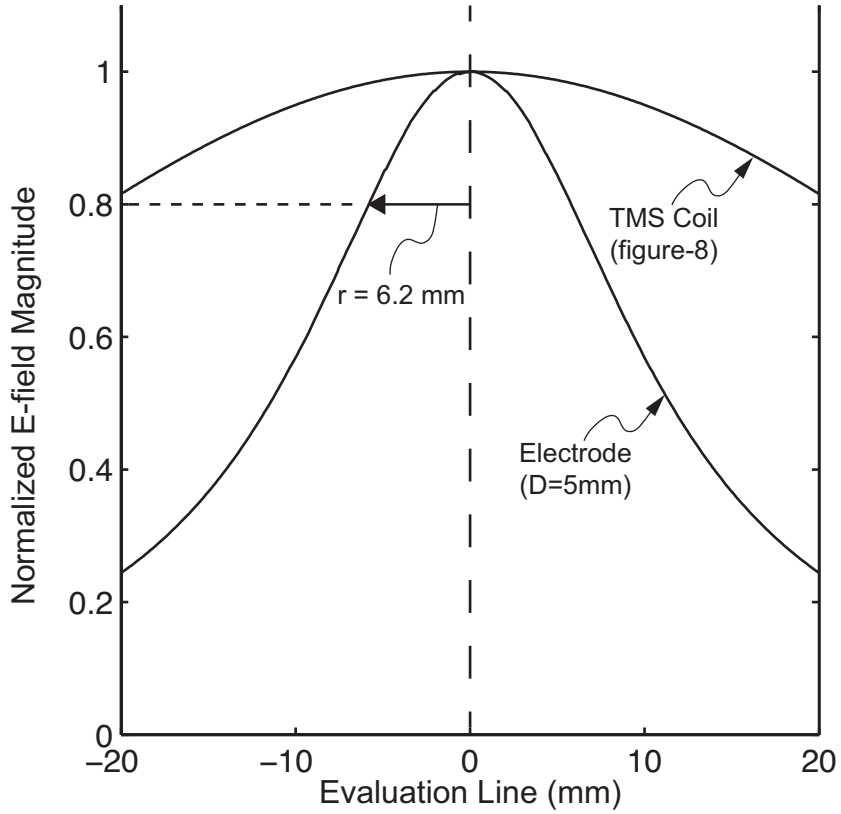

Figure 18 Normalized E-field Magnitude from TMS Coil and Electrode. The resulting E-field produced by a magnetic (figure-8 TMS coil) and electric (cylindrical ECS electrode) source was compared. E-field magnitude was computed on an evaluation line positioned 10 mm below the plane of each source. The center of the evaluation line (0 mm) intersects the vertical midline of each source.

i. Development of Pyramidal Cell Model

The pyramidal cell model was adapted from the model created by Amatrudo et al. (2012), with the addition of a synthetic axon (L = 2 mm) developed by Mainen et al. (1995). Modifications of the Amatrudo et al. model included mechanisms to accommodate for either electric or magnetic stimulation. We performed two computational experiments of the effect of the E-field from TMS and ECS on the neuron model. For the first, the strength-duration relationship for the neuron was obtained under three conditions: 1) stimulation from magnetic induction via a circular coil (*D* = 90mm) elevated from the plane containing the neuron by 10 mm, 2) stimulation from cylindrical

ECS electrode (D = 5 mm) elevated from the plane containing the neuron by 10 mm, and 3) stimulation from a current injection within the soma of the cell.

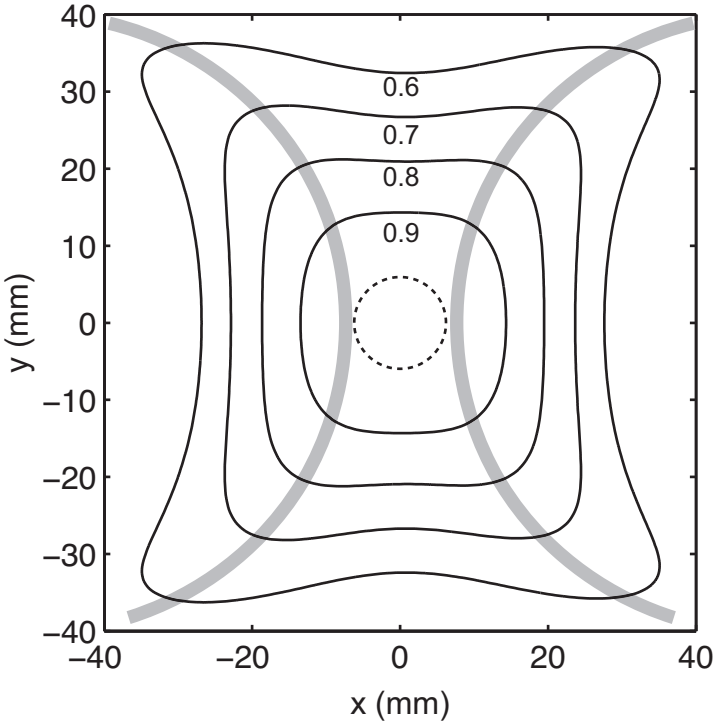

Figure 19 Contour Plot of E-field Magnitude from Figure-8 TMS Coil. Normalized ($\mathbf{E}/\mathbf{E}_{max}$) contour plot of the E-field magnitude is plotted with the 80% E-field contour from the ECS electrode (dotted line). The large transparent half circles illustrate coil windings of the figure-8 coil.

In the second experiment, the response of the neuron to a magnetic stimulus at different transmembrane voltages was simulated. The threshold stimulus (stimulus amplitude required to cause soma depolarization) was found at different transmembrane potentials, and the simulated response to the threshold stimulus was recorded. This experiment was carried out for both the biphasic and monophasic stimulus waveform using the same setup as in the strength-duration experiment. Transmembrane potential was modulated prior to the magnetic stimulus by injecting sub-rheobase current into the soma.

Strength-duration Relationships

Strength-duration curves were obtained (Figure 20) and chronaxies were normalized to rheobase. The rheobasic E-fields for magnetic and electric stimulation were 241.0 ± 0.4 V/m and 243.8 ± 32.0 V/m, respectively. Chronaxies from TMS and ECS were found to have lesser durations than that from intracellular stimulation (current clamp). Respective chronaxies are shown in Table 4.

Table 4 Chronaxie and Rheobase for Tested Stimulation Paradigms.

	Chronaxie	*Rheobase*
Circular Coil	0.791 ms	241.0±0.4 V/m
ECS Electrode	1.072 ms	243.8±32.0 V/m
Somatic Current Clamp	5.675 ms	0.289 nA

Electric and magnetic stimulation produced very different E-fields around the neuron. The magnitude of the stimulating E-field from the ECS electrode had a standard deviation 91x greater than that from TMS. In other words, the E-field was more uniform during TMS than during ECS. Chronaxie of the pyramidal cell was dependent upon the stimulation paradigm.

I found that an action potential was initiated at varying latencies following the onset of the stimulus (step function). Stimulus durations of even 100 ms (above rheobase) caused no additional depolarization after the first spike. Conversely, intracellular stimulation greater than rheobase caused a train of periodic action potentials to spread throughout the cell.

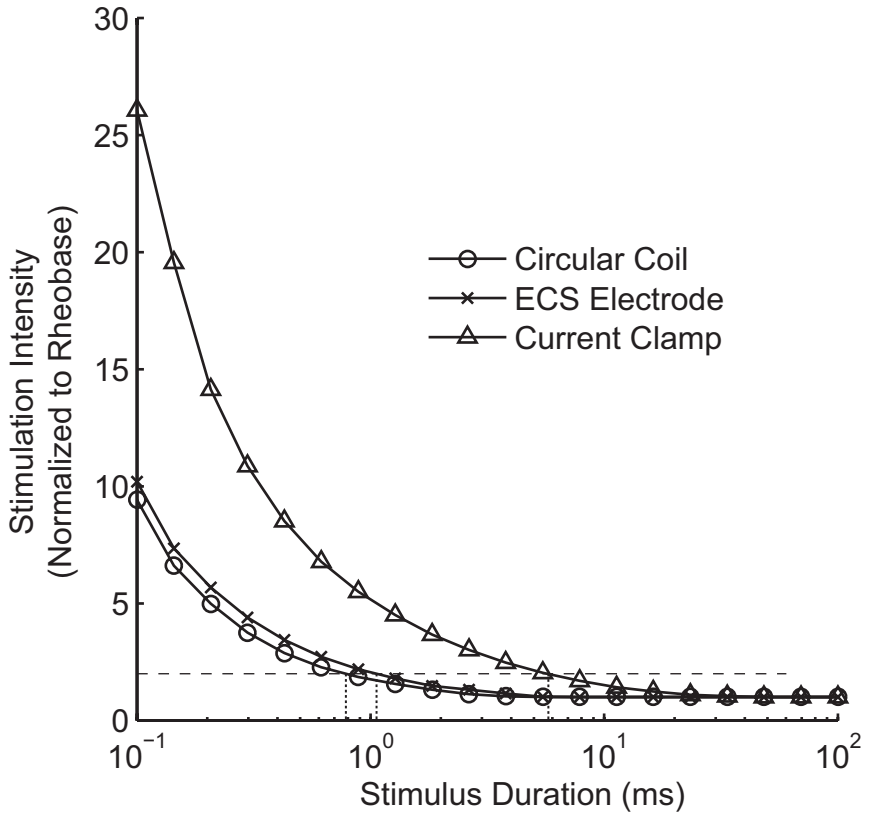

Figure 20 Strength-duration Relationship of Pyramidal Cell Model. Strength-duration curves are shown for the pyramidal cell under three stimulation conditions: 1) magnetic stimulation via a circular coil, 2) electrical stimulation via an ECS electrode, and 3) intracellular stimulation via somatic current clamp. Twice the rheobase is indicated by the horizontal dotted line. Vertical dotted lines are chronaxies for respective stimulation paradigms.

Membrane Potential Influences Activation Threshold

It has been hypothesized that the variability in neural response to TMS can be ascribed to variability in cell membrane potential at the time of the stimulus (Walsh & Pascual-Leone, 2005). This hypothesis was tested in this study by means of the pyramidal model oriented in an induced E-field as illustrated in Figure 9A. The magnitude of the threshold stimulus was found to depend upon the transmembrane potential at the time of the stimulus (Figure 21A). Additionally, the latency of soma depolarization varied with respect to both the stimulus waveform shape and transmembrane potential (Figure 21B). Mean latencies of soma depolarization following the stimulus were 2.60 ms and 3.91 ms for the monophasic and biphasic waveform,

respectively. Intracellular potential prior to stimulation was found to be unrelated to the latency of soma depolarization.

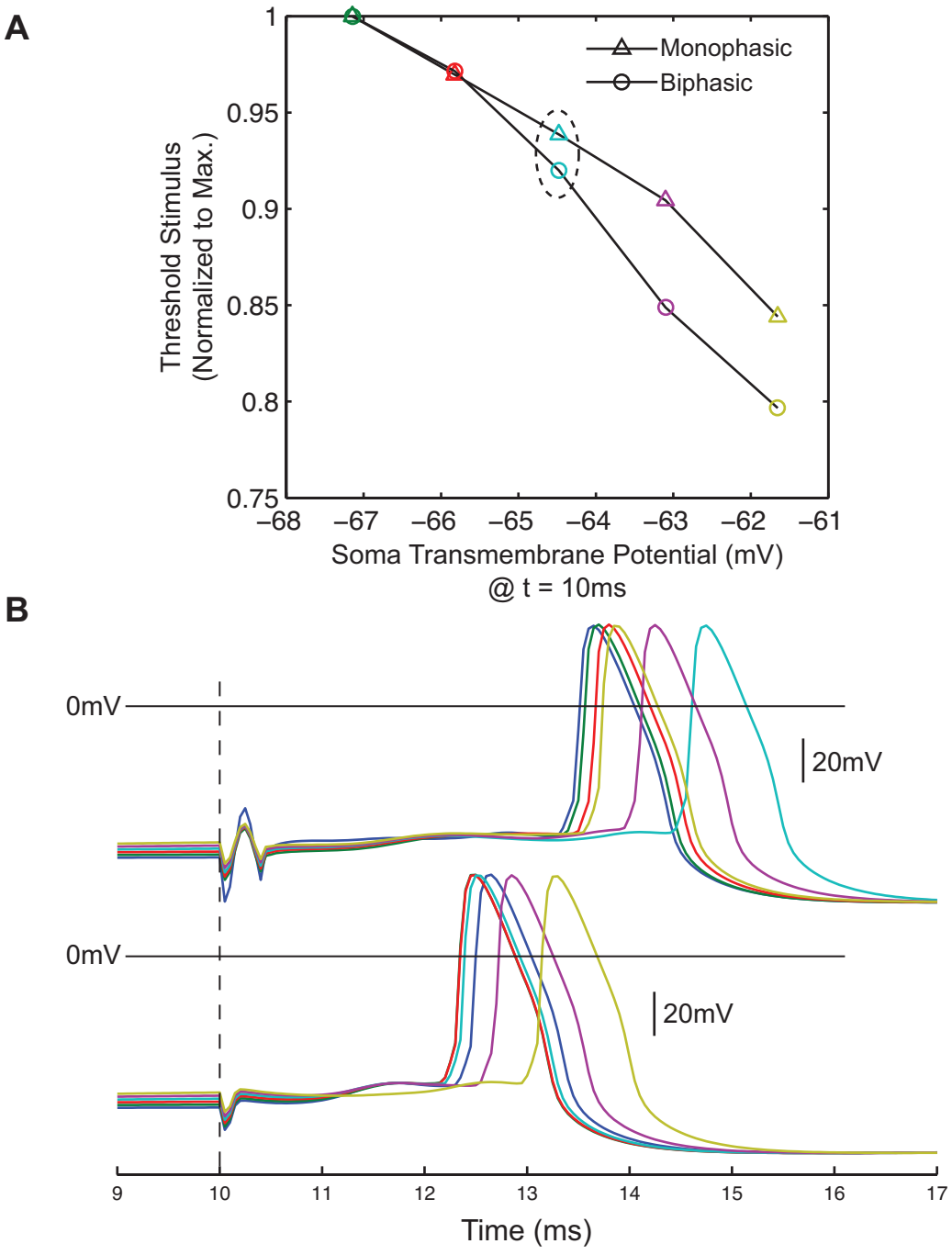

Figure 21 Threshold Stimulus as a Function of Intracellular Potential. (A) Threshold stimulus was found relative to soma membrane potential at stimulus onset (resting potential = -70mV). (B) The soma response to a biphasic (top) and monophasic (bottom) stimulus at the threshold stimulus for each case. Marker colors in (A) correspond to (B). Circled data in (A) are points of interest and have been analyzed further (see **Figure 22**). Note the relative order of their action potential times in (B).

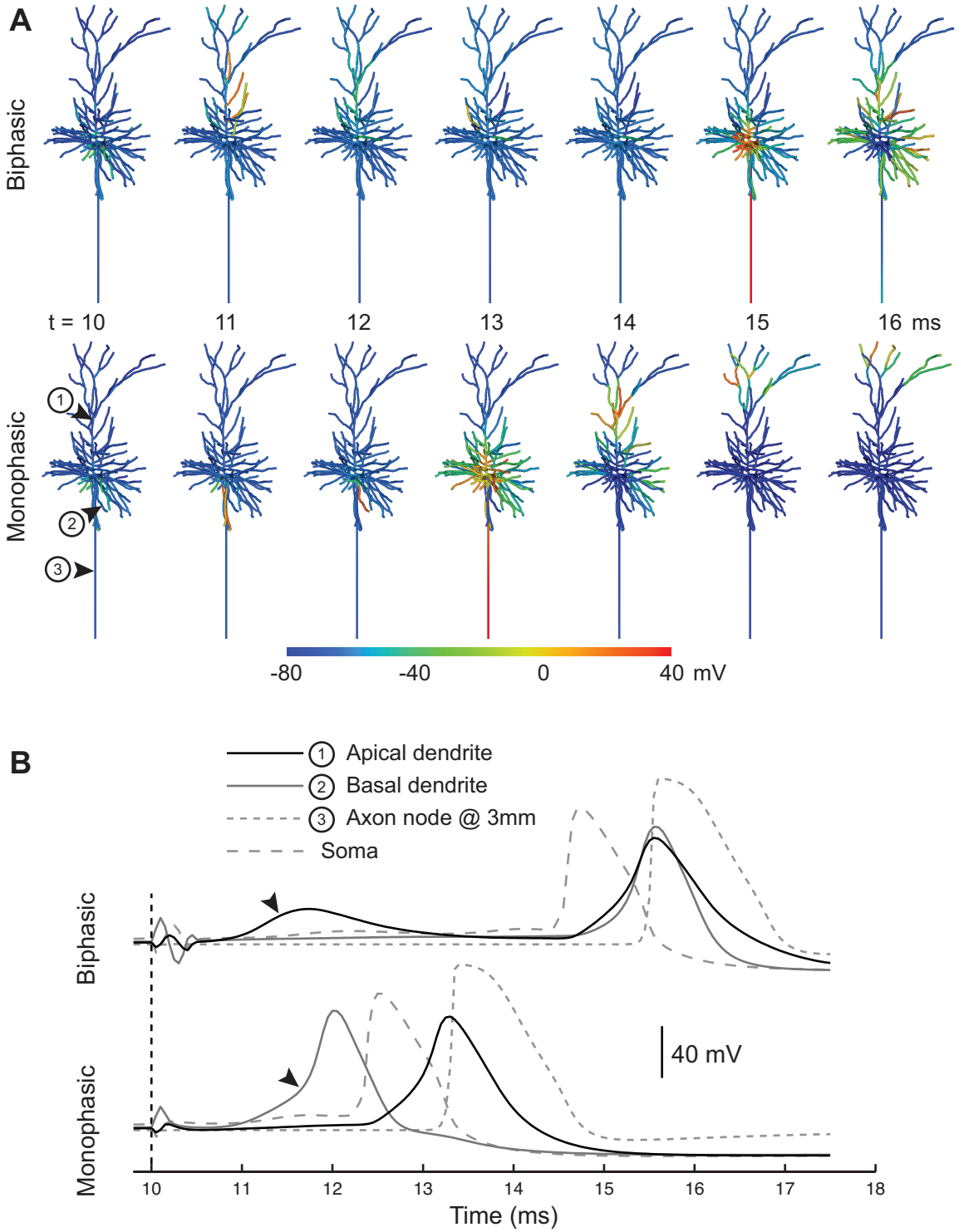

Figure 22 Pyramidal Cell Response to Biphasic and Monophasic Stimulus. Pyramidal neuron response to biphasic and monophasic stimulation is shown for data points of interest (circled points in **Figure 21**A). (A) False color map of intracellular response to threshold stimulus. Cell compartments of interest are marked numerically (1, 2, and 3). Compartments of interest include (1) an upper compartment of the apical dendrite, (2) a compartment within a basal dendrite, and (3) a node of Ranvier at 3 mm depth (arrow indication not to scale). (B) Transmembrane responses are shown for compartments of interest. Black arrows indicate times

of depolarization in compartments that send excitatory input to the soma. Subsequently, the soma depolarizes, which leads to a spread of depolarization throughout the cell.

The cellular response from a monophasic stimulus had marked differences to that from a biphasic stimulus. Neurites extending from the soma showed sensitivity to stimulus waveform. Pyramidal cell simulations indicate that, for the given stimulation condition (Figure 9A), apical dendrites are more sensitive to biphasic stimulation whereas basal dendrites are more sensitive to monophasic stimulation. This result suggests that the structure of a dendrite relative to the induced E-field influences its susceptibility to activation (Figure 22).

Cell simulations show that the threshold stimulus of neural elements varies with membrane potential (Figure 21 & Figure 22). In addition, increasing the soma transmembrane potential caused both the biphasic and monophasic threshold to decrease. The biphasic threshold was found to decrease more than the monophasic threshold.

In summary, our model simulations suggest that 1) the threshold stimulus varies with induced E-field (Figure 20), 2) the threshold stimulus decreases with increasing intracellular potential of the soma (Figure 21), 3) the neuron response varies with respect to stimulus waveforms (Figure 21A and Figure 22), and 4) the susceptibility of a neurite to activate depends upon stimulation waveform and transmembrane potential at the instant of the stimulus.

DISCUSSION

In this study, electromagnetic theory has been applied to the analysis of magnetic stimulation of neurons and techniques in computational neuroscience have been applied to simulate the response of a single pyramidal cell to a time-varying E-field

from magnetic induction. Our modeling approach offers a number of advantages over previous methods in TMS modeling: 1) the E-field produced by Magstim stimulator units[31] can be accurately predicted in space and time, 2) the effects of TMS on neurons with complex structures can be assessed, and 3) the time-dependent neuron response to a defined magnetic stimulus can be simulated. Using this novel approach, the model has been demonstrated to be viable in simulating the response of a single cell to electric or magnetic stimulation. Transmembrane responses of individual neural elements following a magnetic stimulus were presented. These techniques were implemented to obtain: 1) a comparison between electric and magnetic stimulation via the strength-duration relationship, 2) a comparison between the biphasic and monophasic threshold stimulus, and 3) a relationship between threshold stimulus and transmembrane potential at the stimulus onset.

Time Dependencies: Fourier Solver vs. Single-frequency Approximation

We compared our Fourier Solver calculations of the E-field stimulus with calculations from past studies that employ a single-frequency approximation. Thielscher et al. (2011), Miranda et al. (2003), and Chen and Mogul (2009)[32] modeled the TMS pulse as a single-frequency sinusoid. TMS model parameters vary among studies, but the single-frequency simplification is congruous throughout the TMS literature because of its simplicity and low computational load. For most cases, induced E-fields can be approximated by this simplification due to the ohmic nature of biological tissue. It has

[31] The work presented in this chapter and subsequent chapters did not involve investigation of any other TMS systems.
[32] See also Kowalski et al. (2002).

been shown that electric permittivity (ϵ) and permeability (μ)[33] have negligible effects on the E-field induced in the head during TMS (Thielscher et al., 2011). Non-negligible effects have been found to occur when permittivity values approach $10^4\epsilon_0$, which is well beyond the electrical properties of biological tissue (Heller & van Hulsteyn, 1992). Therefore, the frequency dependent material properties can be safely assumed as linear. For example, Thielscher et al. (2011) report E-field magnitudes in terms of $\mathbf{E}/\mathbf{E}_{max}$, not in absolute units.

Though single-frequency conditions can be assumed for quantifying the normalized E-field throughout the brain, this assumption is incompatible when either the absolute E-field (V/m) or neuronal influences are of interest. The time course of the induced stimulus has biophysical ramifications (Thielscher et al., 2011) and could significantly affect the spatial extent of stimulation. As a result, using the E-field solution from a single frequency with Barker's activating function is an oversimplification of the effects of TMS on neural elements, and this was confirmed by our model of a TMS pulse on a multicompartmental pyramidal cell neuron model shown in Figure 21 and Figure 22.

The Fourier Solver has versatility as an analytical tool for computing the effects of any TMS waveform, which is a pivotal advantage over steady-state (or single-frequency) solvers. Further investigation can be carried out to better understand the effects of waveform shape on neural elements, and it enables the TMS waveform to be optimized for either targeting or not targeting certain neuronal elements. How different waveform shapes can influence the modulatory effects of TMS remains to be seen. We made the strategic decision to constrain our analyses to widely used stimulus waveforms that are integrated into clinical TMS systems. This decision was made for two related

---

[33] Permeability and permittivity material constants are defined in relative terms (μ_r and ϵ_r) where $\mu = \mu_0\mu_r$ and $\epsilon = \epsilon_0\epsilon_r$.

reasons: 1) to design an approach that is clinically translatable and 2) to provide insights that directly impact the clinical implementation of TMS.

Comparison of Induced E-fields from Magnetic and Electrical Stimulation

Our results suggest that the E-field produced by an ECS electrode is not analogous to that produced by TMS. These E-fields were found to have substantial dissimilarities in terms of magnitude and spatial attributes. Additionally, magnetic induction gives rise to E-fields in intracellular space, which are not present during ECS due to high membrane resistance to current flow. Since ECS adds charge into extracellular space, electrical interactions with ion channels are extracellular in nature. Conversely, magnetic stimulation exerts an EMF on existing charge in both intracellular and extracellular space. By theoretical and finite element analysis, this study demonstrated that mechanisms of magnetic stimulation can be explained in terms of intracellular interactions (Figure 15 and Figure 16). This understanding of TMS mechanisms is consistent with findings from Day et al. (1989) that different modes of stimulation preferentially modulate different neural elements.

Our results also suggest that the spatial extent of stimulation from ECS electrodes is much more focal than that of TMS. The E-field magnitude from ECS is $\propto 1/R^2$ and as a result, the E-field is almost completely diminished at $R = 15\ \mathrm{mm}$ from the electrode. On the other hand, human TMS coils are much larger and the magnitude of the induced E-field is $\propto 1/R$. Neural activation via TMS seems to rely more on pyramidal cell structure and orientation whereas neural activation via ECS depends on absolute voltage and the spatial derivative of the E-field. Previous studies support this notion (Krieg et al., 2013; Opitz et al., 2011; Ruohonen & Karhu, 2010; Thielscher & Wichmann, 2009; Thielscher et al., 2011).

Development of Pyramidal Cell Model

We developed a novel approach to modeling the time-dependent response of a neuron to induced E-fields from any stimulation paradigm. A computational model of a pyramidal cell neuron from the dlPFC of a monkey (Amatrudo et al., 2012) was adapted to simulate the response of a cell to E-fields induced from TMS. Only one other study has been published utilizing a multicompartmental pyramidal cell model to simulate its response to TMS (Pashut et al., 2011). Pashut and colleagues simulate the cellular response to the E-field produced by a stimulating solenoid within a homogenous medium. Our study builds upon this approach by adding a human TMS coil model, time-dependent TMS stimulus waveform model, and pyramidal cell model with a threshold finder. Our computational modeling approach possesses the flexibility to simulate the response to any time-dependent stimulating E-field. It remains to be seen how the E-fields in the brain influence neuron response simulations.

The pyramidal cell model developed in this study is limited in that it does not account for the induction of non-uniform transmembrane potentials around the circumference of a membrane (Figure 17C). However, results from the cylindrical axon FEM suggest that this limitation is not detrimental to the neural response prediction. The resulting transmembrane potential from a TMS pulse has asymmetric characteristics around the membrane circumference at only the axon bend. This voltage differential around the membrane circumference was found to be insignificant compared to the net hyperpolarization (Figure 17B). Therefore, the induced potentials were assumed to have a uniform effect on ion channels around the circumference of the membrane.

Our results suggest that pyramidal cell sensitivity to a magnetic stimulus depends significantly on its structure. Simulations indicate that dendrites have differing susceptibilities to activation for differing stimulus waveforms. Dendrites extending from

the apical stem were sensitive to biphasic stimulation whereas basal dendrites were sensitive to monophasic stimulation (Figure 22B). Assuming activation occurs in the dendrites, the latency of soma depolarization would be a function of its length and time constant. Dendrites in pyramidal cells have lower length constants and slower time constants than other elements such as the soma, axon hillock, and axon. Perhaps the earlier I-waves from motor cortex TMS are related to activation of various dendritic branches, which are responsible for varying latencies of soma depolarization and thus earlier I-waves (Figure 21B & Figure 22).

We recognize that these model results depend on the surrounding E-field as described by Figure 9A. Based on the results, we nevertheless expect any neural element to have a susceptibility to activation that is dependent upon the stimulus.

We have presented a novel approach with the primary aim to define, describe, and model the physical and biophysical parameters at the interface of the neuron and a magnetic stimulus. With this model, our objective is to help elucidate possible mechanisms responsible for the variability of the physiological response during TMS. The results suggest that at least three interrelated factors contribute to the response variability of a single pyramidal cell:

1) The precise site(s) of activation depends on the *membrane potential* of the cell body, *stimulus intensity*, and *stimulus waveform*. Soma depolarization was found to depend on the collective responses of the neural elements branching from the cell body. Pyramidal cell dendrites show unique excitatory or inhibitory responses and vary in susceptibility to activation.
2) Cell body depolarization depends at least on the net excitatory contribution from connected neurites. It follows that excitation of the cell body occurs at irregular latencies as confirmed by our modeling results. The latency from suprathreshold

stimulation depends on the specific time and length constants of the excited elements and their distance away from the soma.

3) The spread of depolarization through the cell depends on the refractory state of each individual neural element. Our results show that the sites of activation are in refractory periods during action potential initiation in the soma, which leads to certain dendrites having immunity to the spread of action potentials through the cell.

TMS is a relatively mature intervention (>30yrs) in neuromodulation that requires further study to better understand mechanisms of activation on the cellular level. The modeling approach presented in this study offers versatility for experimentation in mechanistic research that would be impossible with current neuroimaging technology. Whether or not these results extend to other neurons, as they would reside in the cortex, remains to be seen.

This modeling study was limited to investigating the response of an isolated pyramidal cell. Future work might use this model to further test the hypothesis by integrating synaptic connections into the pyramidal cell model, which could provide insights into additional sources of variability during TMS. A strong case has been made for trans-synaptic stimulation during TMS, which is fundamental to the I-wave hypothesis and remains to be confirmed through validated models (Edgley et al., 1997; Nakamura et al., 1996).

CHAPTER 2

MODELING CHANGES IN MODULATORY EFFECTS IN THE HAND-KNOB OF MOTOR CORTEX FROM CHANGING COIL ORIENTATIONS

INTRODUCTION

Despite the overall promise of TMS as a neurophysiological tool, it is limited by considerable variability in physiological response within and among subjects. As a result, it is difficult to predict the response(s) to TMS on an individual subject basis. The variability in the physiological response to TMS could be due to a wide range of factors including coil placement relative to the head, the stimulation waveform (e.g. monophasic or biphasic) and the neurophysiological state of the subject (Jung et al., 2010). Our understanding of the effects of TMS is partly limited by the inability to quantitatively describe the effects and locations of stimulation both within cortex and deeper structures like white matter.

Currently, there is debate about the sites of neural modulation resulting from supra-threshold TMS. It is well accepted that pyramidal cells are one of the neural targets of TMS (Herbsman et al., 2009). Stimulation of pyramidal cells could occur within the soma, descending axon, or both (Di Lazzaro et al., 2004; Pashut et al., 2011). The neural response most likely varies relative to stimulation parameters. Evidence exists for pyramidal cells as the origin of direct-waves (D-waves), which elicit robust motor responses (such as muscle twitches) during motor cortex stimulation. Accordingly, the stimulation threshold for the D-wave is lower than that for indirect waves (I-waves) (Hern & Landgren, 1962; Terao & Ugawa, 2002). Excitation of white matter has been hypothesized to cause ascending and descending action potentials that innervate cell bodies and distal interneurons (B. J. Roth & Basser, 1990).

The mechanisms of stimulation outside of the motor cortex are mostly unknown since the vast majority of our knowledge has been gathered from electrophysiology recordings from descending corticospinal neurons and terminal muscles (Di Lazzaro et al., 2008). Describing the neural targets of TMS remains a challenge due to limitations in functional imaging and the inherent diffuseness of stimulation. Imaging modalities such as functional magnetic resonance imaging (fMRI) (Caparelli et al., 2010) and positron emission tomography (PET) (Krieg et al., 2013) have been employed for locating affected areas. However, functional imaging modalities lack the temporal resolution required to observe the immediate neuronal effects of TMS. TMS studies combined with electroencephalography (EEG) aim to examine the immediate responses of TMS, but are largely interrupted by the robust stimulation pulse artifact. Even with an absent artifact, the immediate neural response diffuses throughout the scalp and is mixed with corticocortical dynamics from large surrounding regions of cortex.

Computational models have been used to predict and visualize many types of neuromodulation therapy like DBS and direct current stimulation (Butson et al., 2007; Datta et al., 2009). Detailed models can provide imaging of dynamics that are impossible to record with neuroimaging modalities alone. Computational approaches are more frequently employed in neuromodulation because of their ability to make predictions and gain insight into mechanisms of modulation. Models for neuromodulation normally employ anatomical and functional imaging with finite element methods (FEM).

The large parameter space for TMS (stimulus intensity, pulse waveform, pulse frequency, coil geometry, coil placement relative to cortex, coil orientation, etc.) makes computational modeling an attractive approach for better understanding its effects. Past efforts to elucidate the effects of TMS have relied heavily on FEM (Chen & Mogul, 2009; De Lucia et al., 2007; Güllmar et al., 2010; Miranda et al., 2003; Opitz et al., 2011;

Rullmann et al., 2009; Silva et al., 2008). These studies have led to a number of hypotheses about the mechanisms for neuromodulation at the interface of the brain and the electromagnetic field elicited by TMS (Silva et al., 2008; Terao & Ugawa, 2002). Detailed computational models have confirmed that the effects of TMS depend strongly on non-homogenous properties of the brain and surrounding cerebrospinal fluid (Opitz et al., 2013). Even the morphology of the pial surface has significance pertaining to neuronal excitation during TMS, and estimating locations of activation requires realistic field calculations combined with detailed neural models (Opitz et al., 2011).

The fundamental goal of this project was to predict and visualize the neural targets of TMS within a target region of cortex on a subject-specific basis. A review of TMS literature indicates that the importance of the precise coil placement is underestimated (Hoogendam et al., 2010). The *motivation* for this study was to understand the effects of changing coil orientation on the targeted region of cortex. Our approach is similar to that of past models for TMS (Thielscher et al., 2011), where we integrate anatomical imaging data to generate a subject-specific finite element mesh of the whole head. Our method is *novel* because it integrates a subject-specific finite element model of the whole head with multicompartmental neuron models to predict the neural targets of single-pulse TMS. This novelty allows for investigation into our hypothesis that accurately predicting neural activation from TMS requires a subject-specific model. Our neuron model is an adaptation of a previously published multicompartmental model of a pyramidal cell (Amatrudo et al., 2012) (Figure 23C). The scope of this project is limited to the elicitation of D-waves by single-pulse TMS. Using this computational approach, we aimed to provide a basis to realize the immediate effects of TMS including 1) reasons for the variability in physiology response, 2)

diffuseness of excitation, and 3) sites of depolarization within cells across the targeted cortical region.

We designed our modeling process to be tightly integrated with TMS navigation systems, which provide image-guided placement of the coil relative to the subject's brain. We applied our model to assess neural response relative to changes in coil orientation as would be recorded by navigation systems.

For this study, we focused our attention on motor cortex stimulation due to its immediate measurable physiological response. Furthermore, complex cortical activity (e.g. D- and I-waves) can be observed using this approach (Day et al., 1989; Edgley et al., 1997).

METHODS

Our experimental approach was designed to achieve two primary objectives. First, a prediction of the electromagnetic field in the brain using a model that can easily accommodate changes in biophysical parameters and coil position without the need to re-create the FEM mesh. This prediction facilitates testing a wide range of material properties (e.g., tissue conductivity and non-homogeneity) and TMS parameters (coil position, orientation, stimulation waveform, etc.). Second, assess the effects of changes in these parameters on the activation of model pyramidal cell neurons in cortex. Simulating neuromodulation during TMS required the use of three primary model components:

1) Model of the figure-8 TMS coil to estimate the magnetic field produced during stimulation.

2) Subject-specific head FEM (Figure 23) to model the time-dependent electromagnetic field produced in the head. We employed a novel Fourier FEM solver to obtain the time-dependent electromagnetic solution within the head.
3) A population of cortical pyramidal cell model neurons that are oriented perpendicularly to the pial surface and are modulated during TMS.

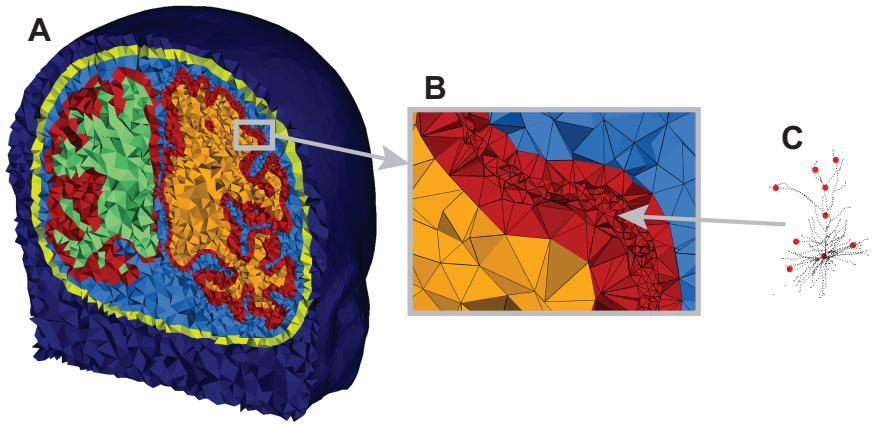

Figure 23 Finite Element Model. (A) A FEM head model was generated from an MRI and segmented into several tissue types. A coronal slice through the FEM is shown with colors indicating the different domains within the mesh: WM (orange), GM (red), CSF (light blue), skull (yellow), and scalp (blue). (B) Close-up of GM with high mesh density for in regions containing the pyramidal cell models. (C) Cell body of pyramidal cell neuron model (axon not shown). The black dots indicate biophysical compartments for simulating intracellular response and the red dots indicate the nodes of the cell that are represented in the mesh, which causes higher mesh density in areas of the GM where the neurons exist.

Figure-8 TMS Coil Field Model

The effects of TMS depend on both fixed and adjustable parameters. Fixed parameters include coil geometry and the number of coil windings. Adjustable parameters include the coil position, coil orientation (θ), stimulus intensity, and stimulus waveform. In order to increase computational efficiency we developed a novel technique that requires only the head to be included in the FEM mesh, which avoids meshing of the coil and surrounding air (Thielscher et al., 2011).

To avoid having to include magnetic induction sources within the mesh, we employed a custom figure-8 coil model based on x-ray measurements (Salinas et al.,

2007). It was designed[34] to analytically compute the magnetic vector potential (A-field, Wb/m) for FEM boundary conditions.

The coil orientation is defined as the angle between the coil handle and the interhemispheric fissure. This specific coil orientation is shown in Figure 24 and is defined as the 45º-coil orientation, which is typical for motor cortex stimulation. We adopted the orientation and coordinate frame from clinical neurophysiology.

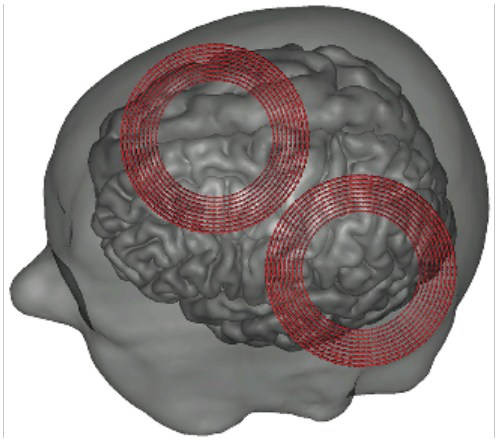

Figure 24 TMS Coil Model. The TMS coil is approximated by current dipoles that represent the wire windings; each red arrow represents a single dipole. This image shows the representation for a coil position of 45º above the hand-knob of the motor cortex.

Subject-Specific Finite Element Head Model

A subject-specific FEM was generated from an image volume acquired from a healthy adult subject. The whole-head T1 MR image was acquired on a 3T scanner at 0.86 x 0.86 x 1 mm voxel resolution (217 x 251 x 180 voxels). Individual tissue types were segmented from the high-resolution anatomical MRI volume using Brainstorm (Tadel et al., 2011) and FreeSurfer (Dale et al., 1999). The Iso2Mesh toolbox (Martinos Center for Biomedical Imaging, Massachusetts General Hospital/Harvard Medical School) was used with MATLAB (MathWorks Inc, Natick, MA) to generate a tetrahedral

[34] See Chapter 1, p. 42 for TMS coil model design methodology.

mesh of the head. “Typical” isotropic conductivity values were applied to the head model based on mean values from multiple studies (Wagner et al., 2004). Our subject-specific head model contains white matter (WM), gray matter (GM), cerebral spinal fluid (CSF), skull, and scalp with isotropic conductivities of 0.126, 0.276, 1.654, 0.010, and 0.465 S/m, respectively (Pashut et al., 2011; Thielscher et al., 2011). The head model was discretized into approximately 1.75 million tetrahedral elements.

The FEM method for electromagnetodynamics is well established (Bastos & Nelson, 2003). We employed the *Magnetic and Electric Fields* physics module within COMSOL Multiphysics version 4.3 (COMSOL Inc, Burlington, MA) to solve the electromagnetic fields within the conductive FEM. The electromagnetic field equations were solved using an FGMRES (Flexible Generalized Minimum RESidual) iterative solver.

In these experiments we specifically targeted the hand knob area of the motor cortex due to its common use in TMS research: this landmark is used for TMS approximating brain regions and finding tuning parameters such as resting motor threshold (RMT). The hand-knob is also used to measure changes in cortical excitability due to an immediately observable response (Day et al., 1989; Pascual-Leone et al., 1994; Stinear et al., 2009; Thickbroom et al., 2006; Vaalto et al., 2010). Our approach enables the FEM solver to converge toward the time-dependent electromagnetic field solution for any coil orientation and stimulation waveform using the same discretization. Ampere’s law with current conservation was applied to all domains within the model.

The time-dependent electromagnetic field produced by the TMS coil relative to the stimulus waveform by an adaptation of a time-dependent Fourier FEM solver (Butson et al., 2007)[35].

Neuron Model

We implemented a biophysically based model of a pyramidal cell located in cortex. We adapted a model originally created by Amatrudo et al. (2012) using the NEURON simulation environment (Yale, New Haven). This model was chosen based on the microstructure of a real pyramidal cell from layer 3 dorsolateral prefrontal cortex (dlPFC) in a rhesus monkey brain and its biophysical properties. This pyramidal cell model is made up of 1342 neuron compartments wherein biophysical properties are defined. We elected to employ a pyramidal cell model on the basis that pyramidal cells are one of the primary stimulation targets during TMS. The pyramidal cell model was adapted to include extracellular mechanisms in which the cell responds to an externally applied, time-dependent E-field (obtained from head FEM). We embedded a custom threshold stimulus finder, which searches for the minimum stimulation amplitude to depolarize the soma of the pyramidal cell. With this design, it is also possible to record the location of action potential initiation on the neuron and the time-dependent response of every compartment in the neuron model for any possible TMS waveform.

Cortex Model

We modeled a patch of cortex using replicates of the pyramidal cell and its axon. Axons of each replicate were modeled to simulate a realistic axons projecting normally from the gray matter and curving into the white matter. The pyramidal cell model was replicated approximately 2000 times within the gray matter in both the targeted and surrounding untargeted region of cortex (Figure 26). The targeted region is indicated by

[35] See Chapter 1, p. 45 for Fourier Solver design methodology.

the red surface and untargeted regions of the pial surface by the blue surface in Figure 25. The combined red and blue surfaces spread approximately 60 sq-cm. For each positioned neuron, the threshold stimulus was found for every tested coil orientation. Threshold stimuli were obtained by simulating neuron responses within the NEURON environment using a high-performance computing cluster (HPC) (Pére, MUGrid, Marquette University).

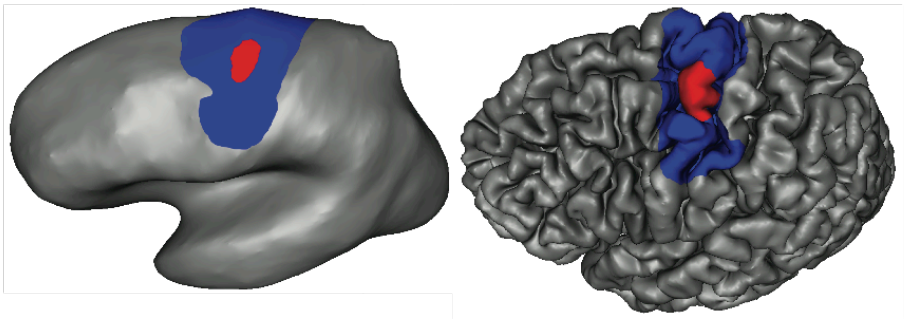

Figure 25 Cortical Target Region. The folded pial and unfolded (obtained from Freesurfer) pial surfaces are shown with the area being analyzed. Neurons were modeled underneath the cortical areas contained by the blue and red surfaces. The red area contains the hand-knob of the motor cortex, which is the target area. A total of 2000 neurons were modeled underneath the shown colored surfaces.

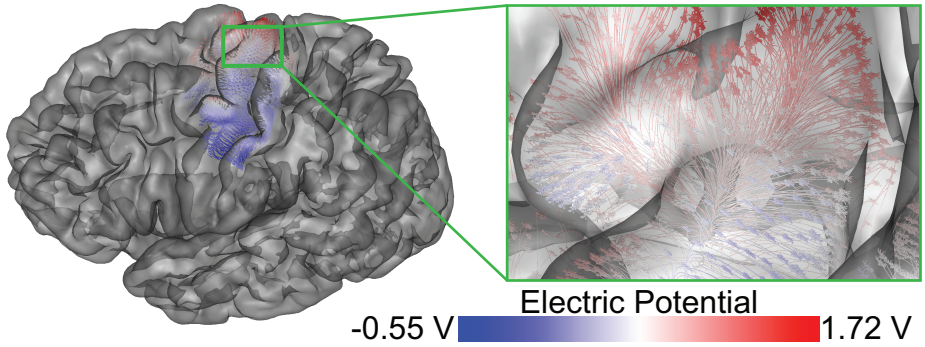

Figure 26 Pyramidal Cell Models in Cortex. Pyramidal cell models with axons are shown inside the transparent pial surface (2000 total neurons). The electric potential (V) solution from the -90º coil orientation is overlaid on the neurons for the purpose of example. Each pyramidal cell has a unique response to extracellular stimulation from TMS for all tested coil orientations.

The threshold stimulus provides a description of the “excitability” of corresponding pyramidal cells for any given coil location and orientation. Using this measure, as the threshold stimulus decreases, the excitability increases. We

constructed excitability maps using the threshold stimulus measure. A unique map was generated for each tested TMS coil orientation.

RESULTS

Our modeling approach provided E-field estimates more efficiently than traditional approaches that require the TMS coil to be included in the FEM mesh. The traditional approach requires an FEM mesh that encompasses the head, coil, and surrounding air space. We found that a mesh of this size requires >3 million elements, and a new mesh must be generated for every change in TMS coil location and orientation, a process that takes about 10 minutes on a high-end OSX workstation. We designed an equivalent model that requires only a single FEM mesh of the head with 1.5 million elements, and does not require a new mesh for each coil orientation. The major advantage to this approach is that we can much more easily accommodate changes in coil position, a capability that we believe is necessary for the model to be integrated with TMS navigation systems.

To test the accuracy of our novel approach, we constructed a traditional FEM mesh that contained a spherical model of the head, windings of the TMS coil, and surrounding air in a semi-infinite medium. We compared the electromagnetic solution from the traditional model to our new approach. The mean percent difference between the two solutions was found to be 0.41% with a standard deviation of 0.29%. The key efficiency improvement came from calculating the A-field, which is an intermediate representation of the magnetic field imposed on the head. However, this A-field is an additional step that is not required for the traditional model, so we next compared the amount of time required to solve the electromagnetic field equations using each approach on a quad-core OSX workstation with quad-core Xeon CPUs (2.66GHz). We

found that the traditional approach required about 1 hour to solve the E-field for each coil position. This amount of time was required to position the coil relative to the head in COMSOL, create the FEM mesh, and solve for the E-field. In contrast, our approach required about 13 minutes for each coil position and can be automated to solve for multiple coil positions. Using our approach, the FEM mesh was generated once for the head. The TMS coil position was determined using an ANT navigation system; this position data was fed into a custom MATLAB script that calculated the A-field (approx. 10 seconds). The A-field was used as a source boundary condition in COMSOL, which calculated the E-field (approx. 11 minutes). Hence, the additional time to calculate the A-field was offset by the savings in computational time provided by creating only a single FEM mesh.

We first assessed electric field magnitudes in the cortical target region as a function of coil orientation. Our results show subtle changes in E-field magnitude inside the targeted area and adjacent gyri as the coil angle θ was varied. The hand-knob gyrus contains the largest E-field magnitudes as θ increases from -15º to +45º. The largest E-fields within the targeted hand-knob were observed with coil orientations where the primary direction of the induced E-field is roughly perpendicular to the central sulcus (between -135º & -165º and between 15º & 45º) (Figure 27). Other coil orientations resulted in lower E-field magnitudes around the targeted region. E-field magnitudes within the white matter were found to be comparable to magnitudes observed in gray matter. Finally, the E-field magnitudes were identical for opposing coil orientations (e.g. 45º and -135º).

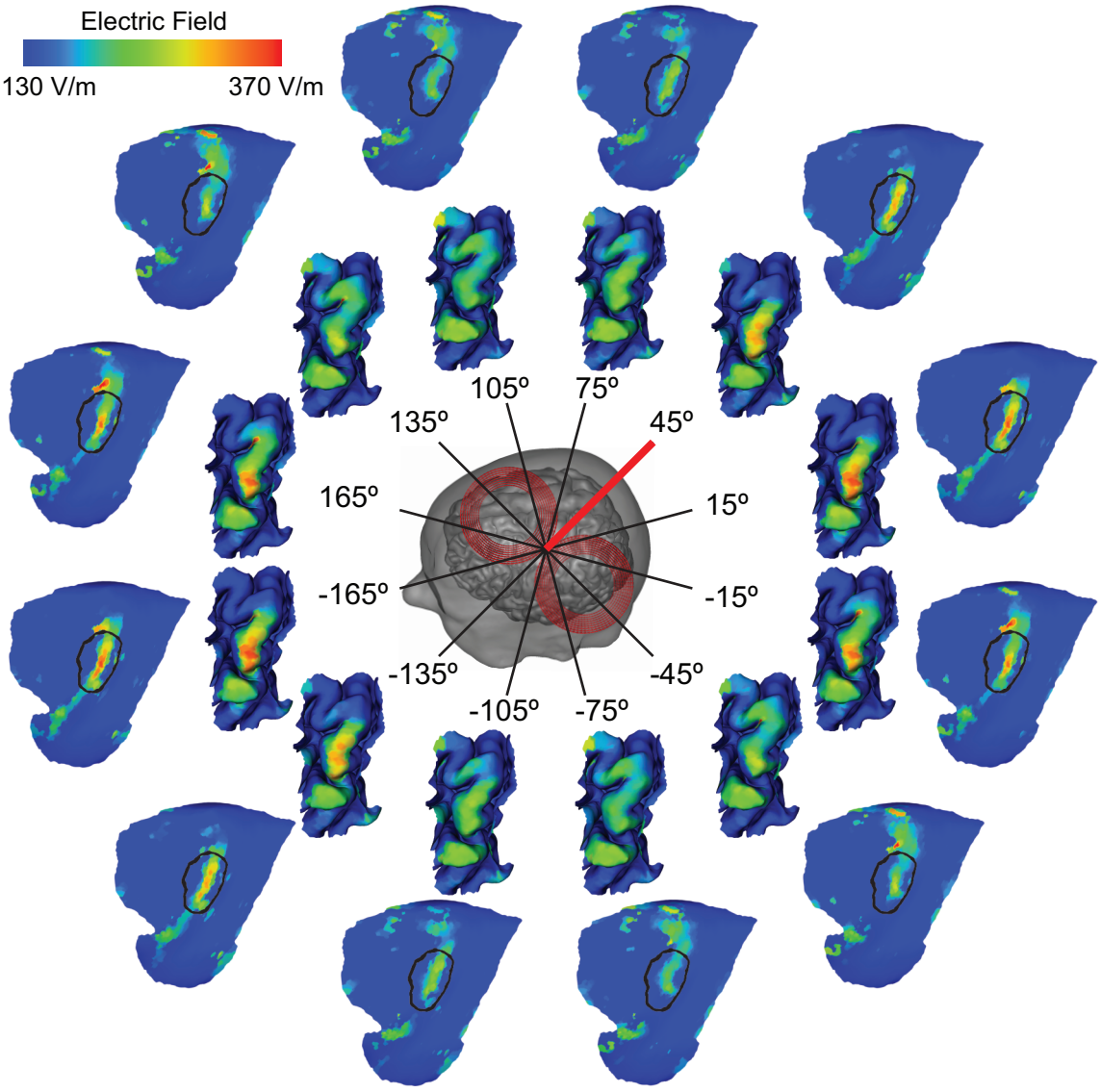

Figure 27 Electric Field Magnitude Maps Relative to Coil Orientation. Coil orientations are shown relative to the interhemispheric fissure. At 0º, the coil handle (black lines) is parallel to the interhemispheric fissure and facing posterior. The orientation of red TMS coil is indicated by the red line and is the most common coil orientation for motor cortex stimulation. Each coil orientation has 2 corresponding surfaces: 1) the folded pial surface containing the targeted and untargeted areas, and 2) the unfolded pial surface containing the exact same map as the folded pial surface. False color maps show the maximum E-field magnitude induced on the pial surface that results from the monophasic TMS pulse obtained from the FEM.

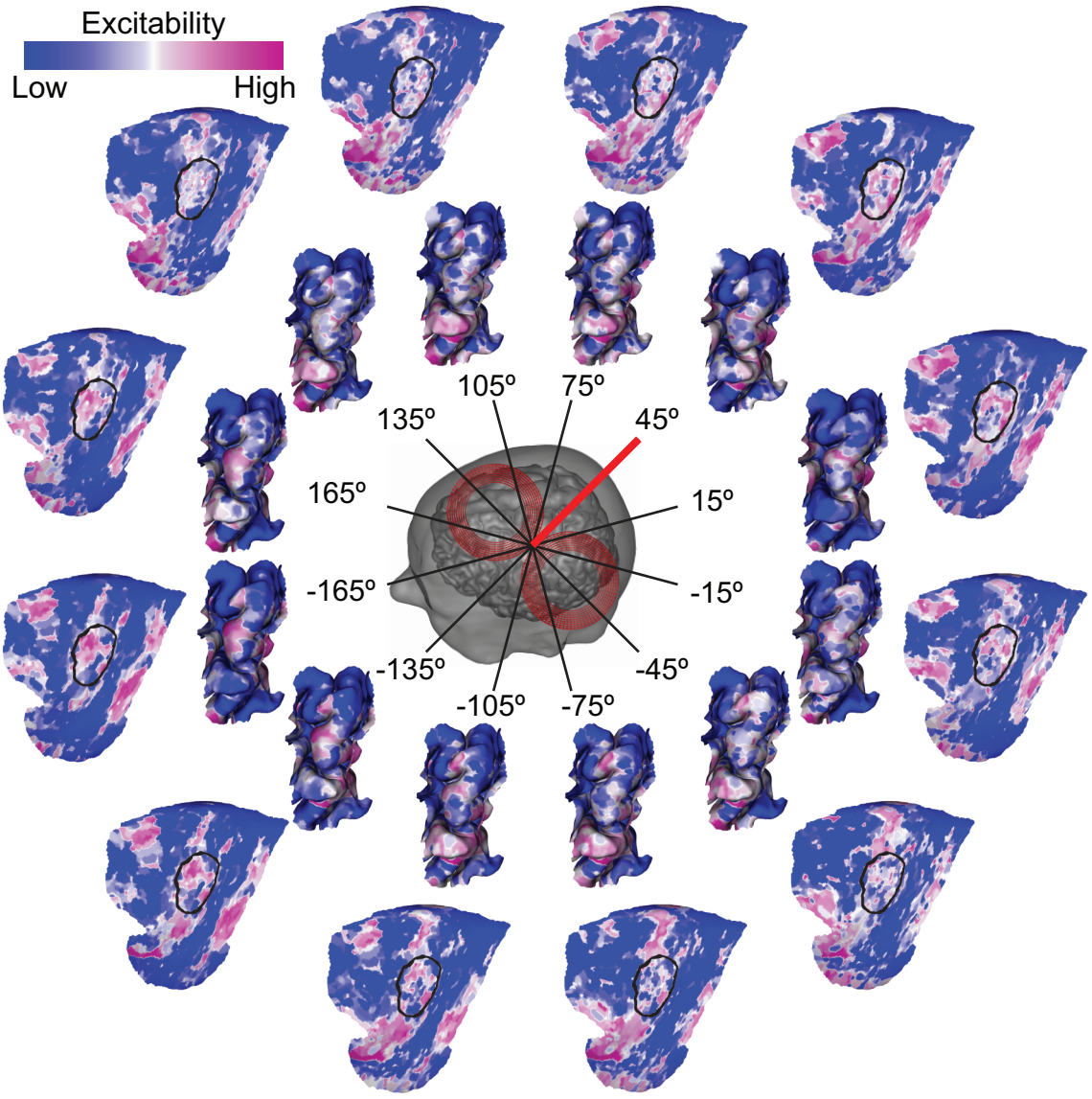

Figure 28 Activation Threshold Maps Relative to Coil Orientation. Coil orientations are shown relative to the interhemispheric fissure. At 0º, the coil handle (black lines) is parallel to the interhemispheric fissure and facing posterior. The orientation of red TMS coil is indicated by the red line and is the most common coil orientation for motor cortex stimulation. Each coil orientation has 2 corresponding surfaces: 1) the folded pial surface containing the targeted and untargeted areas, and 2) the unfolded pial surface containing the exact same map as the folded pial surface with a black outline of the hand-knob region of the motor cortex as shown in **Figure 26**. "Excitability" describes the stimulation (monophasic TMS pulse) threshold of the neuron directly underneath a given area of the surface. Areas in pink contained neuron models that possessed low stimulation thresholds, being more excitable than neurons located under blue areas that had high stimulation thresholds.

The electric potential solution was obtained via FEM. We then interposed the electric potential on pyramidal cell NEURON models replicated within the gray matter surrounding the targeted area (Figure 26). The electric potential was obtained from the

electromagnetic FEM solutions of each coil orientation. The minimum stimulus intensity required to depolarize the soma (or threshold stimulus) was found to measure the excitability of the pyramidal cells. Neurons that had low (below the mean) thresholds were deemed more excitable than areas with high (above the mean) thresholds. Threshold results are represented as a false color map of the pial surface that contained NEURON models directly underneath (Figure 28). Approximately 2000 neuron models were placed underneath the pial surface. Contrary to E-field maps, excitability maps between opposing coil orientations (180º difference) differed from each other.

Our results confirm past RMT measurements where the most robust motor response is observed when the coil is oriented at 45º (Figure 29). However, discontinuities exist between excitable areas at 45º and other orientations (Figure 28). Neurons within the hand-knob (Figure 25) have high thresholds for coil orientations between +75º and +135º.

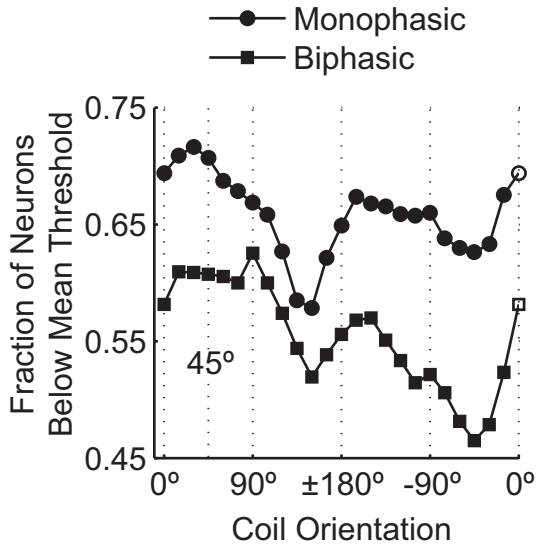

Figure 29 Threshold Stimuli for Monophasic and Biphasic Waveform. Fraction of neurons (out of 2000) for each coil orientation that have stimulation thresholds below the global mean threshold (the mean threshold of all neurons from every coil orientation and each TMS waveform), which we calculated from a total of 96,000 neurons. The biphasic and monophasic TMS waveforms were obtained from in-vitro recordings from the Magstim Rapid and Magstim 200, respectively. The empty markers on the right side of the plot are copies of the 0º quantities on the far left of the plot.

We compared monophasic and biphasic TMS waveforms delivered by stimulator units Magstim 200 and Magstim Rapid (Magstim Company Limited, Carmarthenshire, UK), respectively (Figure 29). We found that changes in coil orientation similarly affect thresholds for both monophasic and biphasic waveforms (Figure 29). Importantly, the biphasic waveform has a comparatively lesser activating effect on pyramidal cells than the monophasic waveform. However, there were exceptions to this general finding.

At 0º-coil orientation, low thresholds were observed in areas on the posterior side of the hand-knob gyrus. Orientations near 180º elicited low thresholds on the anterior side (Figure 28). This finding suggests that the location of maximum E-field is a coarse predictor of the location of stimulation from TMS. Electrophysiology studies (Butson et al., 2007) confirm that threshold values in the hand-knob are sensitive to coil orientation and not just positional placement over the scalp. Our results indicate that a 30º-coil orientation has the greatest excitatory effect whereas an orientation of 150° produces a threshold map with the fewest neurons below mean threshold (Figure 29).

For most neuron response simulations, supra-threshold stimulation elicited an action potential originating in the axon separated by a varying number of nodes of Ranvier from the hillock. Action potentials initiated deeper within the white matter or within gray matter, very close to or within the axon hillock. More than 5% of modeled neurons show initiation of two action potentials at different sites along the curved axon.

DISCUSSION

The fundamental goal of this project was to develop and test a methodology that would enable prediction and visualization of neural targets within a patch of cortex on a subject-specific basis. To achieve this goal, we developed a detailed subject-specific model that simulates the response of pyramidal cells in the motor cortex to TMS. We

build upon past models that have relied on FEM to compute E-fields (Chen & Mogul, 2009; De Lucia et al., 2007; Güllmar et al., 2010; Miranda et al., 2003; Opitz et al., 2011; Rullmann et al., 2009; Silva et al., 2008). Our aim was to use the E-field to realize the immediate effects of TMS including 1) reasons for the variability in physiology response, 2) span of excitation, and 3) sites of depolarization within cells in the targeted cortical region.

Non-magnetic forms of brain stimulation inject charge (current) into the brain (and then retrieve it), which gives rise to focal changes in voltage and causes activation of neural elements nearby. The electric field gradients elicited from TMS are comparatively less than those elicited from non-magnetic sources. Consequently, the effects of magnetic stimulation are a function of brain anatomy, especially the shape of neural elements. Our approach demonstrates that the use of neuron models and FEM provide insights into mechanisms of magnetic stimulation.

Numerous cell types exist in cortex, but we focused on synaptically isolated pyramidal cells, which are believed to mediate the direct response to TMS of motor cortex (Di Lazzaro et al., 2004; Herbsman et al., 2009; Pashut et al., 2011). Although synaptically isolated cells do not represent the full repertoire of the neural response, our approach is an important step in characterizing the cellular effects of TMS. In future work we will examine the neural response of synaptically connected circuits in cortex.

Our current model accounts for non-homogeneous, isotropic conductivities. Work is currently underway to employ MRI techniques such as diffusion-weighted imaging (DWI) to accurately assign appropriate material properties for each head segment. This approach would allow for the inclusion of anisotropic conductivities.

Importantly, our modeling results do not have explicit validation but are based on theoretical analysis. Our subject-specific model suffers from several limitations, but it

confirms physiological observations for motor cortex stimulation. Specifically, electrophysiology studies confirm that the most robust response is elicited with a coil-orientation that is roughly 45º (Kammer et al., 2007). Our model additionally confirms this physiological phenomenon by quantifying the overall effect of TMS relative to coil orientation (Figure 29).

We observed a strong correlation between coil-orientation and thresholds across the targeted region (Figure 29). However, individual maps (Figure 28) of local thresholds have complex features that make it difficult to draw broad conclusions about activated regions. Here, we expanded upon existing models for TMS by implementing neuron modeling, which has been more frequently used in neuromodulation over the last decade (Butson & McIntyre, 2005; Chaturvedi et al., 2010; Walsh & Pascual-Leone, 2005).

Previous studies have simplified the TMS pulse by modeling it as a single fundamental frequency (Thielscher et al., 2011). This simplification is valid for electromagnetic theory since permittivity values have negligible effects on the electric field during TMS. Our results indicate that this is an over-simplification of the waveform dynamics in simulating the response of neural elements (Figure 28). Our time-dependent model provides insight into the advantages or disadvantages of certain TMS waveforms. We have reported threshold maps for only the monophasic waveform (Figure 28), but we have shown comparisons between the effects of mono- and bi-phasic waveforms (Figure 29).

Our results suggest that when modeling TMS, close attention should be given to the orientation of neural elements, the morphology of the cortical surface, and coil geometry. We found that rotating the coil 15º caused changes in thresholds both inside and outside the target region, which suggests that locations of neural activation have an

acute sensitivity to coil position and orientation. The fraction of neurons below total-mean threshold (the mean from all coil-orientations combined) was quantified for each coil-orientation (Figure 29). These quantities suggest that a preferred coil-orientation for the hand-knob target exists (approx. 30º).

E-field maps indicate that focal stimulation of the hand-knob can be achieved with certain coil-orientations. With E-field alone, however, it is difficult to predict whether untargeted areas are being avoided. For example, E-field maps (Figure 27) show that coil-orientations between +75º and +135º would be ineffective in stimulating the hand-knob whereas orientations between 0º and 90º would be more effective. However, excitability maps (Figure 28) indicate that no coil-orientation focally stimulates the hand-knob region while avoiding other regions.

Excitability maps (Figure 28) from opposing (180º apart) coil-orientations have noticeable differences, which do not appear in E-field maps. This discrepancy demonstrates the importance of time-dependent modeling to assess neural responses in areas of interest. Excitability maps illustrate the complexity of TMS and the inherent difficulty there is in constraining stimulation. The corollary is that the E-field, though simpler, does not provide an accurate prediction of stimulated brain regions according to our model. Our modeling technique could also validate motor-mapping outcomes when dealing with large coil position datasets acquired from TMS navigation systems.

For each threshold map (Figure 28), we quantified the overall effect of TMS by counting the number of pyramidal cell neurons that had a threshold below the mean threshold (from all maps combined) (Figure 29). We recognize that this quantity is not a measure of the effectiveness of a certain TMS coil position since both targeted and untargeted areas are included in this quantification. Interestingly, this measure seems to coincide with the consensus in motor mapping applications: a coil angle near 45º elicits

robust responses in the hand-knob. However, the degree to which adjacent brain regions are affected seems significant, and our approach provides the means to test different coil geometries for stimulating specific neural structures while avoiding others. Lastly, broad threshold measures in Figure 29 suggest that the biphasic pulse has a lesser effect on pyramidal cell models underneath the coil for all orientations compared to the monophasic pulse for a given stimulus intensity. This dichotomy could possibly be explained in terms of the inherently greater E-fields induced by the monophasic waveform, but reasons for this remain to be investigated.

Our results suggest that small changes in TMS parameters can affect stimulation targets, and that these changes could result in variability in the location of energy delivery and the degree of neuromodulation within cortex. In addition, we have demonstrated that TMS navigation data combined with subject-specific modeling can be used to quantify the excitability of pyramidal cells around the targeted area. Our modeling approach enables the evaluation of a broad range of coil positions and orientations with only a single finite element mesh, which is advantageous when performing analysis on a per-pulse basis. Lastly, we found that accurately modeling the electromagnetic interactions within the brain requires close attention to 1) the geometry of the cortex and white matter surfaces, 2) the TMS parameters that are both fixed (coil winding geometry) and adjustable (coil position and orientation relative to the head), and 3) orientation of excitable neural elements in cortex and white matter.

CHAPTER 3

QUANTIFYING PHYSIOLOGICAL RESPONSE TO MOTOR CORTEX TMS

INTRODUCTION

TMS has the potential to become a widely used tool in neuromodulation for therapy, brain-mapping, screening, and neurorehabilitation purposes (Grefkes & Fink, 2011; Grefkes et al., 2010; Vaalto et al., 2010; Wagner et al., 2006, 2007). Our understanding of TMS and its effects have limited its utilization beyond research investigation (Thielscher et al., 2011). A great deal of effort has been invested in TMS research to arrive at a validated model for predicting targets of activation (Fox et al., 2004; Opitz et al., 2013). A primary motivator is that we currently lack a reliable model that is amenable to clinical use. Advancements in computational modeling have demonstrated it to be a viable means for TMS to transition into the clinical environment as reliable tool.

TMS modelers have acknowledged that changing the orientation of the coil will alter the primary induced E-field (Basser & Roth, 1991). As demonstrated in Chapter 2 of this study, changing the direction of the E-field changes the E-field magnitude within the brain, especially when oriented perpendicularly to the targeted gyrus. This phenomenon introduced researchers to the complex interactions during TMS that give rise to neural activation. As a result, a great deal of work has been invested in making geometrically accurate models of the head (Thielscher et al., 2011).

Early TMS models employed spherical geometries to estimate induced E-fields in the head from TMS via Maxwell's equations (Bohning et al., 1997; Tofts, 1990). In some sense, the TMS modeling community has advanced beyond employing E-fields as a

predictor of the target region. Although, E-fields are still remains the most important measure in many studies (Laakso et al., 2014; Wagner et al., 2006). The focus of TMS modeling has since shifted toward studying activation in terms of the E-field along hypercolumns, which have also been modeled by employing the activating function along hypothetical columns or axons emanating from white matter within the gray matter (Fox et al., 2004; Krieg et al., 2013; Thielscher et al., 2011). The most well-known model for predicting activation is the cortical column cosine (or C^3) model, which accounts for the E-field magnitude and the orientation of hypercolumns in the cortex (Fox et al., 2004). C^3 model predictions are based on the E-field component along the pial surface normal vector (hence the "cosine" in C^3). This model says activation occurs if the C^3 E-field is suprathreshold. This predictor and its respective variants have been standard in TMS modeling.

Almost all models for TMS research employ nonhomogenous finite (volume or boundary) element models for estimating induced E-fields (Chen & Mogul, 2009; Salinas et al., 2009). Few studies have developed models that account for the anisotropic conductivity of the head (De Lucia et al., 2007; Opitz et al., 2011). The spatially dependent conductivity within the brain is derived from diffusion coefficients obtained via diffusion weighted MRI (DWI) (Tuch et al., 2001).

Interestingly, the predictive power of TMS models is based on the presupposition that excitation *does* occur. In other words, models are able to predict possible locations of stimulation based on the presupposition that a suprathreshold E-field is induced. Unlike probabilistic models employed for DBS (Butson et al., 2007), models for TMS have not matured enough yet to enable predictions based on probabilistic approaches that regard precise stimulation parameters.

In this study, we present a multiscale, subject-specific modeling methodology with corroboration from physiology. We quantified the physiological response to motor cortex TMS using the MEP amplitude from FDI EMG. In this study, we report one subject from a population with corresponding subject-specific model predictions corroborated by physiology. Four *novel* contributions to neuromodulation research are presented in this study: 1) an anatomical and functional imaging based model of the whole head and excitable neural element within cortex and white matter, 2) predictions of specific sites of activation within gray and white matter, 3) quantitative description of the immediate neural response and extent of activation, and 4) physiological corroboration of model predictions. Our *motivation* for this study is that TMS is limited because of two unknown variables during stimulation: 1) the loci of activation during TMS and 2) the extent of modulatory effects proceeding from stimulation of neural elements in the brain.

METHODS

Motor Cortex Stimulation

Multiple subjects were enrolled for motor cortex TMS experimentation, but methods from one subject are reported in this study. Our goal was to develop a model corroborated by physiology; efficacy of intervention was not within the scope of this study. We specifically focused on the immediate neurophysiological effects from TMS, and constrained our human subject experimentation in four ways: 1) single-pulse TMS (less than 0.5 Hz), 2) motor cortex stimulation, 3) monophasic or biphasic stimulus only (Magstim Stimulator units), and 4) figure-8 coil.

First, MR images including a high-resolution (0.86 x 0.86 x 1 mm; 217 x 251 x 180 voxels) T1 anatomical scan and DWI were acquired of the whole head.[36] MRI scans were utilized in two ways: 1) to integrate with TMS navigation software for real-time anatomical targeting and 2) to construct a subject-specific head model medical imaging software and post-processing.

Second, motor cortex TMS was carried out for each subject. MR image volumes were loaded into TMS ASA navigation software (ANT Neuro, Enschede, Netherlands)[37] navigation software for targeting the hand-knob of the motor cortex. ANT Neuro TMS navigation was utilized to provide real-time anatomical targeting. The subject was equipped with bipolar surface EMG electrodes on the (right) arm contralateral to the targeted hemisphere. EMG electrodes were adhered to the FDI, bicep, tricep, and extensor indicis (EI) muscles. The head of the subject was registered with the image volume using TMS navigation. Specific landmarks according to the nasion coordinate system were used to register the head with the image volume: nasion, left pre-auricular, and right pre-auricular. The hand-knob of M1 was then identified within the image volume and 3D coordinates (nasion coordinate system) were logged into TMS navigation software for targeting purposes.

Third, the resting motor threshold (RMT) was obtained for both the biphasic and monophasic stimulus. The RMT was defined as the minimum stimulus intensity that elicits a visible involuntary hand twitch in at least 5 out of 10 trials. RMT was obtained using a coil orientation of 0º relative to the interhemispheric fissure (or PA). Angles were measured relative to the plane of the interhemispheric fissure where the coil handle

---

[36] See Appendix D, p. 168 for detailed description of MRI and DWI protocol.
[37] Advanced Source Analysis (ASA) software is developed by ANT Neuro for integration with TMS Navigation (http://www.ant-neuro.com/products/asa). See http://www.ant-neuro.com/products/tms-coil-navigation.

points posteriorly, and angles increase counter-clockwise from the perspective of the experimenter. We measured coil orientations according to this convention established for clinical use (Julkunen et al., 2009). The RMT for the monophasic (Magstim 200 Stimulator unit) and biphasic (Magstim Rapid Stimulator unit) stimulus were measured to be 40% and 55% of maximum stimulation intensity, respectively.

Fourth, single-pulse TMS was administered over the targeted area (hand-knob of M1) while simultaneously recording EMG according to protocol[38]. Four stimulation scenarios were carried out: 1) 110% RMT monophasic stimulation, 2) 140% RMT monophasic stimulation, 3) 110% RMT biphasic stimulation, and 4) 130% RMT biphasic stimulation. The MEP was acquired from the FDI EMG response. The immediate physiological response was quantified by the EMG amplitude of the MEP in FDI (units: mV; EMG response). This muscle was used to quantify the MEP due to the consistent triphasic shape of the FDI EMG waveform compared to other recorded muscle groups (Figure 33), and the FDI muscle represents a larger area of the hand-knob compared to the other recorded muscle groups. The EMG responses were acquired via *Spike2* (Cambridge Electronic Design)[39] system. Single pulses were delivered at less than 0.5 Hz. MEPs were acquired for multiple coil orientations ranging from -180º to 0º for two stimulation intensities (110% and 140% RMT). More than 300 stimuli were delivered, and their corresponding MEPs and coil placements relative to the head were acquired.

Data Analysis

Over 200 trials[40] were analyzed (approx. 100 trials were discarded due to TMS navigation errors or outliers), each having a unique coil placement and EMG response. Trials were separated into 13 stimulation groups according to similarities in coil

---

[38] See Experimental Procedures, pg. 27.
[39] Cambridge Electronic Design (CED) develops *Spike2* software.
[40] One trial is the evoked response from a single TMS pulse.

placement over the scalp. Each group contained a collection of trials that correspond to an identical stimulation waveform (monophasic or biphasic) and intensity (percentage of RMT). Each group contains similar coil orientations (approx. ±5º) and positions (maximum ±8 mm). The amplitude of the MEP in FDI was used to quantify the immediate physiological response (units: mV). The purpose of the data analysis was to obtain a measure of the immediate physiological response that describes the size of the population of recruited upper motor neurons within the hand-knob from a single TMS pulse. Our underlying assumption was that the amplitude of the MEP in FDI is directly proportional to the population size of pyramidal cells activated within the hand-knob.

The MEP from each group (13 total groups) of trials was averaged. The coil placement from each trial was reduced to a single coil position/orientation by satisfying least-squares criterion for 6 degrees of freedom (roll, pitch, yaw, and 3D spatial coordinates) through a custom-made iterative algorithm developed in m-script for use in MATLAB.

In summary, stimulation data were reduced to 13 *stimulus experiments*, which were employed for model validation by comparing model simulations with the physiological response. Each *stimulus experiment* is associated with a monophasic or biphasic stimulus waveform and a single unique coil position, coil orientation, mean MEP, and stimulation intensity.

Subject-specific Model

Our goal was to build a subject-specific model to enable estimation of electromagnetic fields occurring within the head for each *stimulus experiment*.[41] To accomplish this goal, we used the subject's MR image volumes (high resolution

[41] See Appendix C, p. 165 for flow diagram of model development.

anatomical MRI and DTI) and utilized open-source software packages[42] for volumetric image extraction, surface building, surface processing, and mesh discretization. TMS navigation data were used to extract coil placements to estimate the actual E-fields produced within the head for each *stimulus experiment*. The finite element method was employed to compute the electromagnetic fields produced by the coil during a single stimulus[43]. This subject-specific modeling approach entails the construction of a tetrahedral mesh of the segmented head volume as well as the application of nonhomogeneous anisotropic material properties measured from DWI.

Finite-Element Approach

A subject-specific, non-homogeneous, anisotropic FEM was generated from an image volume acquired from a healthy adult subject. Individual tissue types were segmented from the high-resolution anatomical MRI volume using Brainstorm (Tadel et al., 2011) and FreeSurfer (Dale et al., 1999). The Iso2Mesh toolbox (Martinos Center for Biomedical Imaging, Massachusetts General Hospital/Harvard Medical School) was used with MATLAB (MathWorks Inc, Natick, MA) to generate a tetrahedral mesh of the head. Specifically, CGal's mesh generator (Alliez et al., 2000) was employed to generate a sub-millimeter scale tetrahedral mesh from a volumetric image. Head segments of the scalp, skull, CSF, GM, and WM were included within the volumetric image and discretized within the mesh.

Following initial tetrahedral mesh generation, we prepared the mesh for inclusion of pyramidal cells and their descending axons using TETGEN (Weierstrass Institute for Applied Analysis and Stochastics, Berlin) to build a custom adaptive meshing algorithm

---

[42] FMRIB Software Library (FSL), Freesurfer, Brainstorm, Iso2Mesh (MATLAB toolbox), TETGEN, and Cgal Mesher.

[43] See Chapter 1, p. 33, for a description of the analytical coil model used to calculate the A-field produced by the figure-8 TMS coil for integration with an FEM.

in m-script, which increases the mesh density near the magnetic sources (TMS coil) and within the brain volume containing pyramidal cells. The final mesh contained 1.05 million tetrahedral elements.

Though neuron model resolution (μm scale) exceeds that of mesh resolution (mm scale), E-field gradients from TMS are so gradual (Figure 18, pg. 69) that the effect of mesh resolution on the solution becomes negligible at a limit (Eq. 27). In general, our adaptive meshing algorithm follows the rule,

$$\rho_{mesh} = \left(\frac{\nabla V}{\nabla V_{max}}\right) \cdot n \qquad \text{(Eq. 27)}$$

where ρ_{mesh} is linear mesh density at a mesh node, ∇V is the voltage gradient (or E-field), and n is the number of edge elements per millimeter (mm^{-1}). Using a 2D axisymmetric mesh of a circular TMS coil (D = 90 mm), we found that ∇V is negligibly affected (<0.1% difference) with $n > 0.5\ \mathrm{mm}^{-1}$ for high power frequencies within the TMS waveform spectrum. We employed a value of $n \approx 2\ \mathrm{mm}^{-1}$ for adaptive meshing within the tetrahedral head model.

The final head mesh was loaded into COMSOL and material properties were assigned. Relative permeability and permittivity were set to unity within all head segments. We assumed isotropic properties in materials other than the brain. Isotropic electrical conductivity was set to 0.465, 0.010, and 1.654 S/m for the scalp, skull, and CSF, respectively. Anisotropic conductivities within white and gray matter were extracted from the volumetric diffusion tensor image. FMRIB Software Library (FSL) (Jenkinson et al., 2012) was employed to process and extract diffusion tensors (FDT[44]), conduct volumetric registration with gray/white matter (FLIRT[45]), and apply conductivity tensors

[44] FMRIB's Diffusion Toolbox.
[45] FMRIB's Linear Image Registration Tool.

to tetrahedral elements of the mesh (Figure 31, *left*). Diffusion tensors were extracted using the FDT pipeline recommended by FMRIB, which includes functions for eddy current correction and diffusion tensor fitting within a brain volume.

Tuch et al. (2001) have shown that a diffusion tensor from a diffusion weighted MRI of the brain is linearly proportional to the estimate of the electrical conductivity tensor. The estimate of the conductivity tensor is obtained from the linear mapping,

$$\frac{\sigma}{d} = 0.844\ [\mathrm{S} \cdot \mathrm{s} \cdot \mathrm{mm}^{-3}] \qquad \text{(Eq. 28)}$$

where σ is the electrical conductivity (S/mm) and d is the diffusion coefficient (sq-mm/s). By definition, the diffusion coefficient is one-third the water particle velocity (v) times the mean free path (ℓ) (Graessner, 2011).

$$d = \frac{1}{3} v\ell \qquad \text{(Eq. 29)}$$

FEM Electromagnetic Field Solution

For each stimulus experiment, FEM boundary conditions were applied from analytical computations of the A-field carried out using a custom made figure-8 coil model[46] based on x-ray measurements by Salinas et al. (2007).

For each coil orientation, the frequency-dependent electromagnetic field solution was obtained via an iterative solver employed by COMSOL. We employed the magnetic and electric field (*mef*) physics interface within COMSOL, which solves the time-harmonic (Fourier domain) equation[47]

$$(j\omega\sigma - \omega^2\epsilon)\mathbf{A} + \nabla\times(\mu^{-1}\nabla\times\mathbf{A}) = \mathbf{J}_e = 0 \qquad \text{(Eq. 30)}$$

[46] See Chapter 1, p. 34.
[47] See Appendix A, p. 162 for a description of Maxwell's equations.

where ω is frequency, ϵ is permittivity, $\mathbf{A}$ is the A-field, μ is magnetic permeability, and $\mathbf{J}_e$ is the external current density. At the external boundary,

$$\mathbf{J} \cdot \mathbf{n} = 0 \qquad \text{(Eq. 31)}$$

where $\mathbf{n}$ is the surface normal vector at the boundary and $\mathbf{J}$ is current density. Throughout the conductive medium, current is conserved ($\nabla \cdot \mathbf{J} = 0$).

Using the Fourier Solver, the electromagnetic FEM solution was computed at 1024 frequencies within the TMS waveform spectrum. The discrete time-step was $\Delta t = 50\ \mu s$ and the frequency step was $\Delta f = 1/(2 \cdot 1024 \cdot \Delta t) = 49\ \text{Hz}$. The solutions at each frequency were then transformed into the time domain via the Fourier Solver[48].

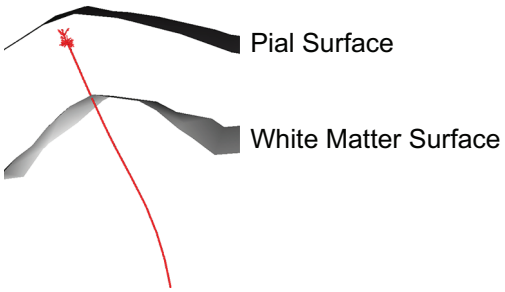

Figure 30 Sample Pyramidal Cell Neuron between Pial and White Matter Surface. One out of 6111 cells is shown oriented perpendicularly to the pial surface for exemplary purposes. Full axon is not shown.

Cortical Model

The pyramidal cell model (Amatrudo et al., 2012) was replicated 6111 times across the cortex within the hand-knob and surrounding areas. The population of pyramidal cells occupied 6454 sq-mm (64.54 sq-cm) of the pial surface. Cells were oriented perpendicularly to the pial surface, and their cell bodies were placed at a depth of 1.125mm (Figure 30). At this depth, the cell dendrites are approximately situated

[48] See Chapter 1, p. 35.

within Nissl stain layers I and II. From the soma to the tip of the highest dendrite measures 800 μm.

Axon Tractography Near Cortex

Axon tractography was performed using SCIRun's (SCI Institute, University of Utah, Salt Lake City) interface with Tend Fiber (TEEM[49]), which uses Westin's linear tensor-line algorithm (Westin et al., 2002). A point cloud was generated around the neuron cell bodies to provide seeds for the axon tractography algorithm. Fiber tracts were generated with the termination criteria that fibers must have minimum length of 20mm and FA must be >0.5. Connections were formed between the cell bodies and fiber tracts via a custom algorithm in m-script that employs Hermite splines[50]. This algorithm ensures that axon trajectories are void of sharp curves (Figure 31). All pyramidal cells in the population had axons 20 mm in length.

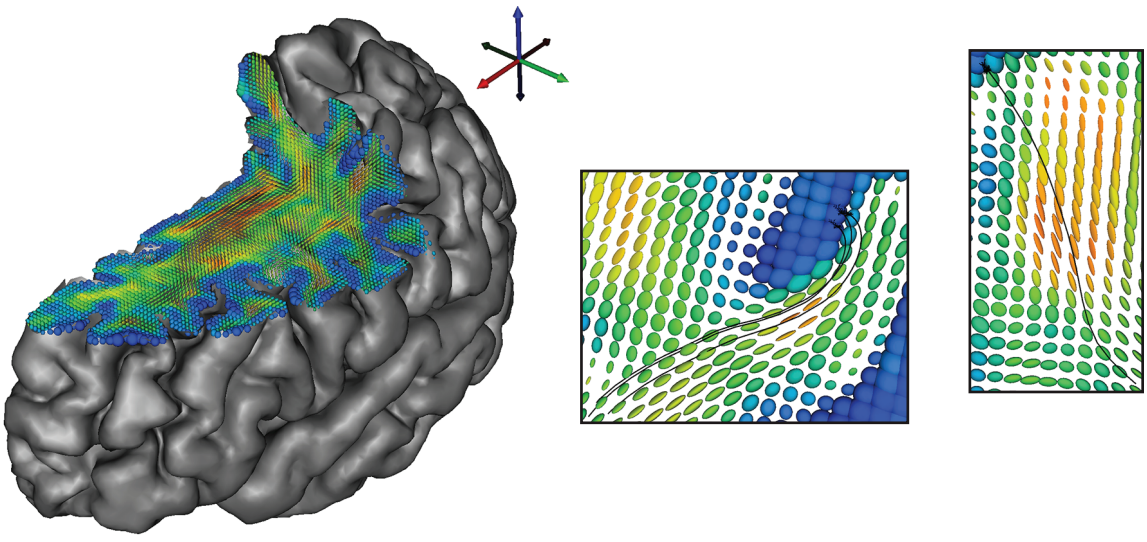

Figure 31 Use of DTI for Anisotropic Conductivity and Neuron Axon Tractography. (*Left*) Acquired DTI was applied to the 3D head model for the inclusion of anisotropic conductivity. (*Right*) Diffusion tensors were employed for axon tractography to construct descending axons from the pyramidal cell bodies. Four out of 6111 neurons are shown for the purpose of example.

---

[49] http://teem.sourceforge.net/

[50] A Hermite spline is a 3D spline generated from Hermite's polynomials, which requires the location and spline trajectory (vector) of two points.

Neuron Model Simulations

The time-dependent E-field solution (from the FEM) from each stimulus experiment was extracted and applied to each neuron compartment within the population (6111 neurons; 1342 compartments per neuron). Neuron responses from each stimulus experiment were simulated within the NEURON environment using HPCs (Pére, MUGrid, Marquette University; SCI Institute, University of Utah). For each stimulus experiment, we found the monophasic and biphasic threshold stimulus. The threshold stimulus is the minimum stimulus amplitude that results in depolarization of the soma. This quantity was employed as a measure of the excitability of a cell to TMS. The cellular response to the threshold stimulus was then simulated and exported for data analysis. Approximately 158,800 neuron model simulations were carried out (6111 neurons; 13 stimulus experiments; 2 stimulus waveforms).

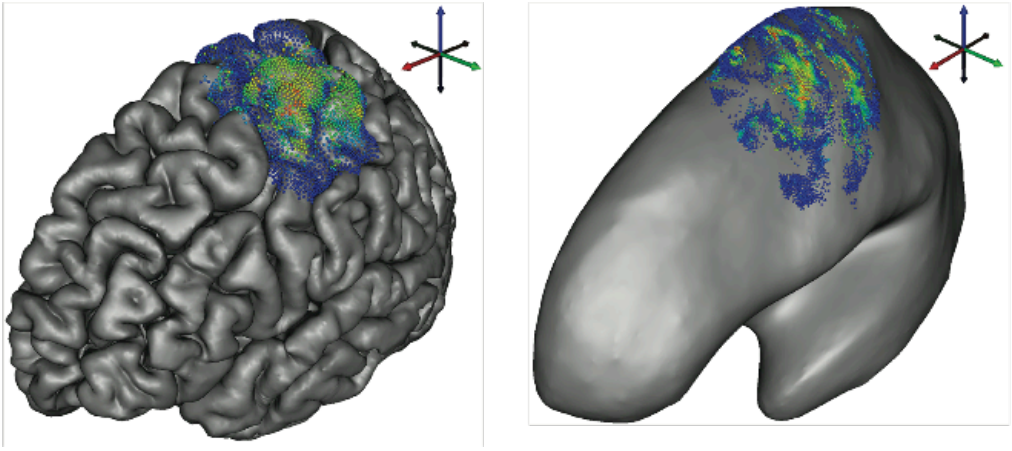

Figure 32 Example Data Maps on Folded and Inflated Pial Surfaces. (*Left*) A false color map of a sample data set is shown via surface nodes on the pial surface. A single node represents the pyramidal cell located directly underneath it within the grey matter. (*Right*) An identical data set on surface nodes of the inflated pial surface. Vacant blotches on the inflated pial surface are the result of the unequal surface mesh density due to the inflation of sulci where surface elements are denser. Experimental data are displayed in this manner throughout the study.

The intracellular response of each cell was analyzed and the site of action potential initiation at threshold was recorded. Neuron response data were organized

according to stimulus experiment. Our experimental results are presented as: surface node plots (Figure 32) and scatter plots.

Model Comparison with Electrophysiology

We compared model predictions with physiological responses from TMS of the hand-knob of human motor cortex. A well-established visualization methodology was employed to localize the hand-knob (Yousry et al., 1997). We compared the amplitude of the MEP (FDI EMG) elicited from TMS of the hand-knob with the threshold stimulus of pyramidal cells computed within the NEURON environment. Pyramidal cell thresholds were computed by simulating the response of the population of cells in the hand-knob for each stimulus experiment.

Model Corroboration

We compared the MEP amplitude with the model simulation for each modeled stimulus experiment and analyzed the threshold stimuli ($\boldsymbol{\nu}$, "*nu*") from neurons located only in the hand-knob of motor cortex (approx. 660 neurons; 1/10th of all models within the cortex) (Figure 38). Firstly, a threshold cut-off value ($\overline{\nu}$) was determined by a qualitative analysis of possible model predictions,

$$\overline{\nu} = k \cdot \mathrm{median}(\boldsymbol{\nu}_{\mathbb{U}}) \qquad \text{(Eq. 32)}$$

where $\boldsymbol{\nu}$ is the set of all threshold stimuli from all stimulus experiments ($\boldsymbol{\nu}$ has Poisson distribution properties). The constant, k $(0 < k \leq 1)$, was included in Eq. 32 to describe the stimulation intensity for the biphasic and monophasic waveform; k increases with increasing intensity. Secondly, the cortical area containing neurons where $\nu < \overline{\nu}$ was computed (each neuron makes up an average of 1.0562 sq-mm of pial surface),

$$A_{\nu<\overline{\nu}} \approx \mathrm{sum}(\boldsymbol{\nu}_{\mathrm{HK}} < \overline{\nu}) \cdot 1.0562\ \mathrm{mm}^2 \qquad \text{(Eq. 33)}$$

where $\boldsymbol{\nu}_{\mathrm{HK}}$ is an array of the threshold stimulus of every neuron in the hand-knob, the logical quantity is an array of ones and zeros, the summation is an integer value of the number of neurons having a threshold stimulus below $\bar{v}$, and the constant term is the average area of the pial surface occupied by a single neuron model. Lastly, the model prediction ($\mathcal{F}$) was computed as a function of $A_{\nu<\bar{v}}$,

$$\mathcal{F}(\boldsymbol{\nu}_{\mathrm{HK}}, \bar{v}) = wA_{\nu<\bar{v}} \quad \text{(Eq. 34)}$$

where $\mathcal{F}(\boldsymbol{\nu}_{\mathrm{HK}}, \bar{v})$ is a prediction of the FDI EMG amplitude and w is a weighting variable that contains statistical measures and a scaling factor.

$$w = \frac{10}{\mu_{\nu}\sigma_{\nu}^{2}} \quad \text{(Eq. 35)}$$

where μ_{ν} and σ_{ν}^{2} are threshold stimulus mean and variance of the population within the hand-knob. In this sense, w is a measure of the collective excitability of the hand-knob.

ν was assumed to be a measure of the excitability of the cell. The distribution of $\boldsymbol{\nu}$ conforms to a Poisson distribution [0,+∞] where σ increases with increasing μ. We elected to include a model weighting to tilt the prediction so that $\mathcal{F}(\boldsymbol{\nu}_{\mathrm{HK}}, \bar{v})$ is dependent not only upon $A_{\nu<\bar{v}}$, but also upon the distribution of $\boldsymbol{\nu}_{\mathrm{HK}}$.

Justification

Our approach is based on motor pool recruitment principle. Motor signals originate from upper motor neuron pools and terminate at muscles. It follows that the amplitude of the muscle EMG is proportional to size of the recruited motor pool (Fuglevand et al., 1993; Pascual-Leone et al., 1994; Yao et al., 2000). Based on this rationale, we elected to form model predictions according to the proportionality (cf. Eq. 34):

$$\mathcal{F}(\boldsymbol{\nu}_{\mathrm{HK}}, \bar{v}) \propto A_{v<\bar{v}} \qquad \text{(Eq. 36)}$$

RESULTS

Motor Cortex Stimulation

We found that EMG responses depend on coil orientation (Figure 39) and that EMG responses to have variable amplitudes throughout single trials with unchanging coil orientations (Figure 33). The EMG response in FDI maintained a consistent shape but other EMG responses exhibited diminished signal, with a low signal-to-noise (SNR) ratio.

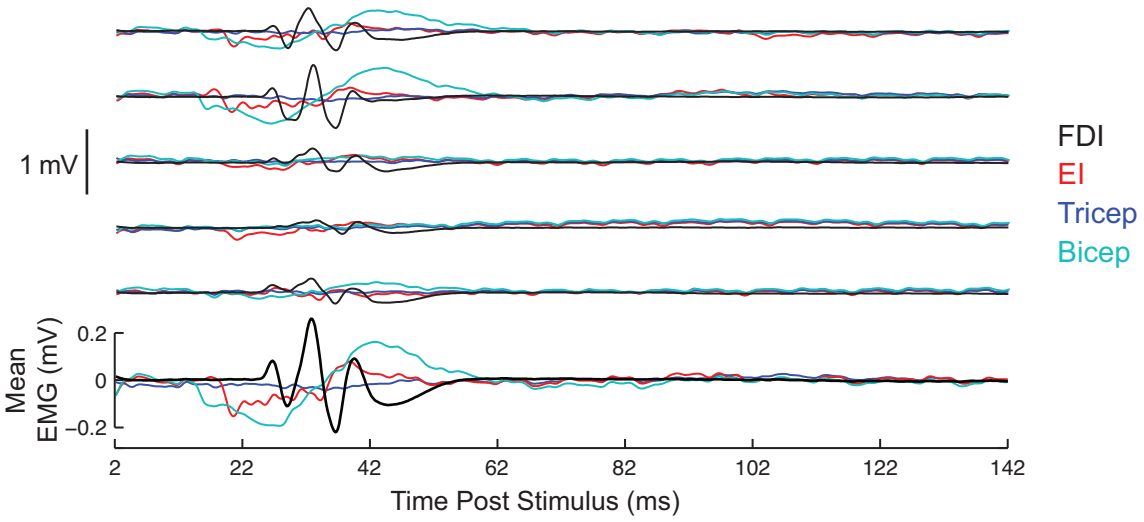

Figure 33 Sample Muscle EMG Responses and Their Time-triggered Average from Five Consecutive Stimuli. Sample traces of the EMG response of the first dorsal interosseus (FDI), extensor indicis (EI), tricep, and bicep immediately following TMS of the motor cortex are shown. Data are shown for five trials along with their mean EMG response. Time series data were filtered using a 750 Hz lowpass filter. The shape of the FDI trace conforms to those reported in previous publications.

Single-pulse TMS was administered over the hand-knob of motor cortex. To localize the hand-knob, we employed a well-established medical image visualization technique and validated this target by TMS navigation with simultaneous EMG. For almost all measured stimuli, post hoc analyses of coil placement data confirmed that the coil was placed in a manner that targeted the hand-knob (Figure 34). Coil placement

was such that the normal vector from the coil-plane intersected the hand-knob area. No correlation was found between pial surface targets and EMG response.

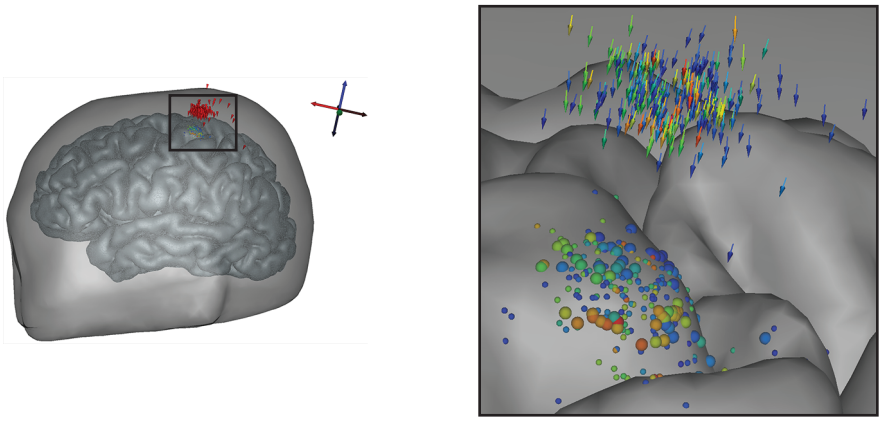

Figure 34 Coil Position During Recorded Stimuli. Delivered stimuli as shown from TMS navigation output in the form of cones in 3D space relative to the head. (*Left*) Red cones indicate normal vector projecting from the coil-plane toward the targeted area. (*Right*) Colored spheres indicate projections from the corresponding arrow vectors onto the cortical surface. Spheres (and arrows) are colored according to the robustness of the muscle EMG response. Spheres have been sized according to the stimulus amplitude. Data were analyzed for comparison with model predictions.

The EMG response amplitude increased with increasing stimulation intensity and varied with changes in coil placement. TMS navigation data were consistent with data obtained during experimentation. However, TMS navigation reported spatial locations inside the scalp in a consistent manner. To account for this offset, placements were moved outside of the scalp surface by translation along the line of the coil-plane normal vector. Coil placements were repositioned so that the coil-plane was raised a minimum of 2 mm from the scalp.

Subject-specific Model Results

E-field intensities and directions agreed with those from previously published anisotropic, non-homogenous conductivity models (Opitz et al., 2011). I found that both E-field intensity and direction were modulated within the targeted gyrus by changing coil orientation (Figure 35).

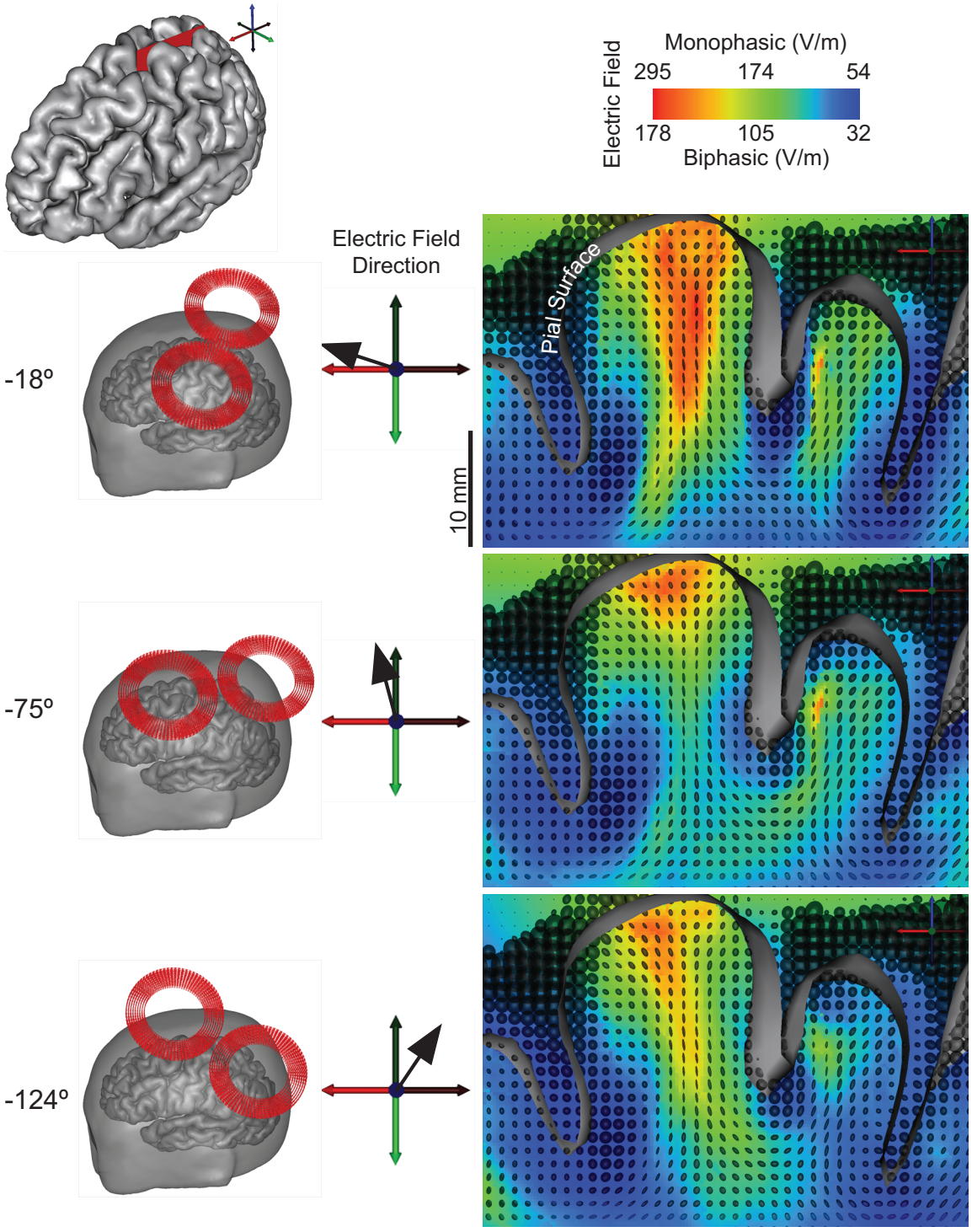

Figure 35 E-Field Within the Cortex for Three Coil Orientations. (*Top left*) The location of the data plane (*red*) relative to the pial surface is shown with the coordinate frame. E-field magnitude maps are shown at peak E-field during the stimulus pulse. Conductivity tensors are superimposed over E-field maps within the data plane. FEM results are shown for three stimulus experiments (*biphasic @ 130% RMT*). Coil placements are shown in the left panes with the primary direction of the induced E-field.

E-field magnitudes were computed at maximum output from the Magstim 200 (monophasic) and Magstim Rapid (biphasic) units. E-fields produced by the Magstim Rapid were found to be significantly less than those produced by the Magstim 200.

Our results suggest that at least 90% of the maximum E-field can be present at depths up to 25 mm within the targeted gyrus (measured from the pial surface) for coil placements where the induced E-field is normal to the central sulcus (Figure 35, *-18°*). Though these results seems contrary to Maxwell's equations ($\mathbf{E} \propto 1/R$), the induced B-field causes current to flow along a path that contains rapidly changing conductivities, which results in augmented E-fields at deeper levels. When the induced E-field is perpendicular to a gyrus, charge is induced at the boundary of the GM and CSF (Tofts, 1990) where there is a rapid change in conductivity. The E-field then gets deflected at these boundaries (on both sides of the gyrus). At first, this seems counter-intuitive since the A-field is not influenced by biological tissue, but the E-field is induced in a nonhomogeneous medium and current must be conserved ($\nabla \cdot \mathbf{J} = 0$). As a result, stray charge is induced where the conductivity changes along the electric current path. Therefore, the nonhomogeneities and anisotropies in CSF, GM, and WM cause the E-field to augment in the middle of a gyrus at a deeper level than expected. This phenomenon was not observed for coil orientations that do not induce current flow perpendicular to the targeted gyrus. E-fields that were induced parallel to the gyrus were less than those perpendicular to the gyrus at deeper levels because no significant changes in conductivity exist along the axis of the gyrus. The E-field magnitude was found to depend on its direction relative to the orientation of the targeted gyrus and its conductivity tensors (Figure 35 and Figure 36A). Both Figure 35 and Figure 36A show results within the same slice or data plane.

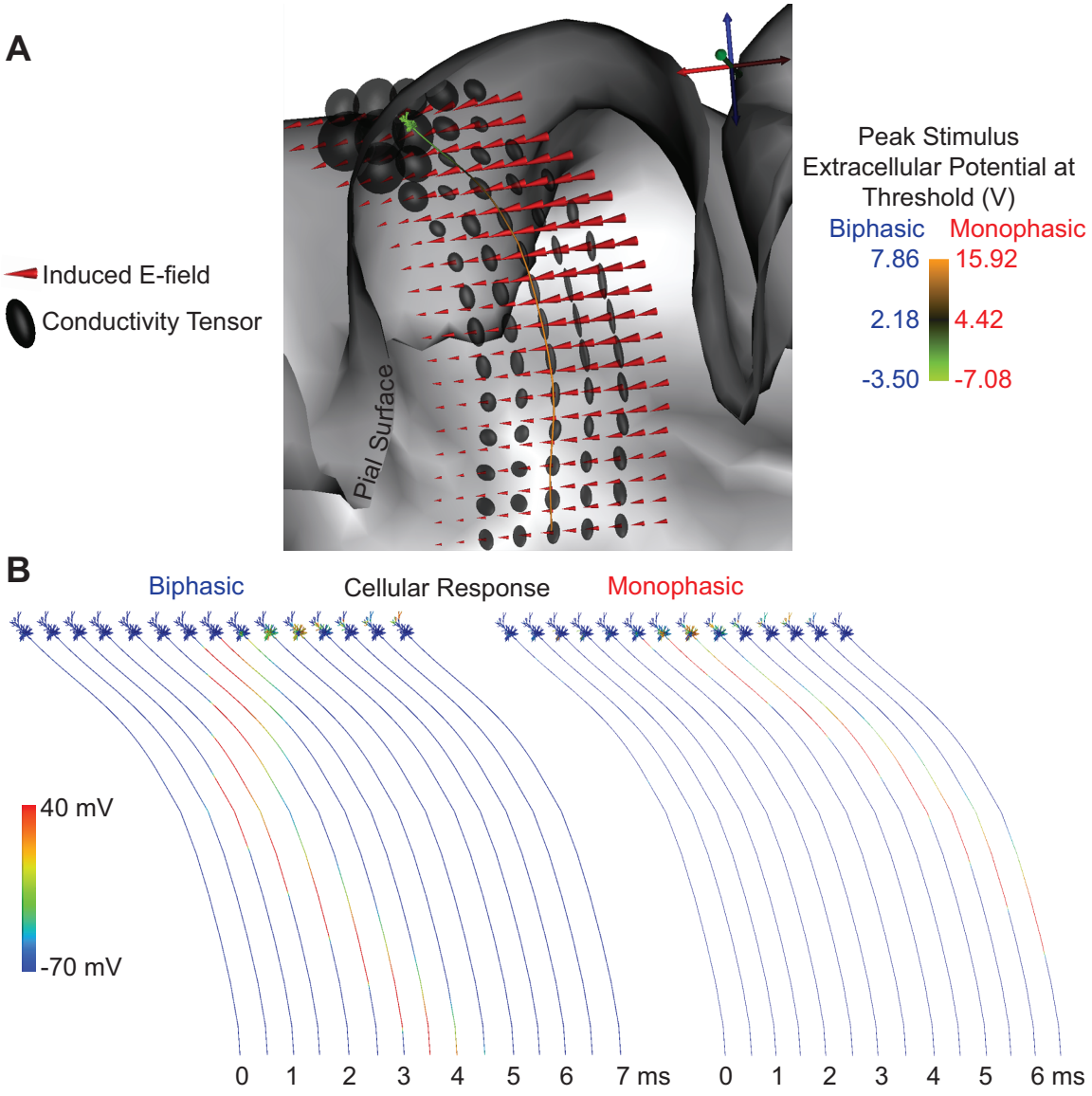

Figure 36 Sample Neuron Response. (*A*) The orientation of a sample pyramidal cell within the hand-knob is shown relative to the surrounding conductivity tensors and induced E-field. The neuron is colored according to **E**·*d***s** (voltage) along the axis of each neuron segment. The color bar is scaled to the threshold stimulus for both the monophasic and biphasic stimulus. (*B*) The corresponding response of the neuron to the threshold stimulus. Action potential originates within the axon and within the dendrites for the biphasic and monophasic threshold stimulus, respectively.

Our axon tractography method generated axons that are consistent with diffusion tensor directions (Figure 36A; cf. Figure 31). We simulated the response of a sample neuron at threshold for the monophasic and biphasic waveform stimulus (Figure 36B). At threshold, the monophasic stimulus produced a net hyperpolarization within the axon

while causing excitation within dendrites. Conversely, the biphasic stimulus elicited a depolarizing effect within the axon. Due to the direction of the induced E-field at stimulus onset, only the second phase of the biphasic waveform would cause depolarizing membrane currents.

Model Comparison with Electrophysiology

Simulations of the pyramidal cell response to magnetic stimuli were carried out for each stimulus experiment. We compared our model results with muscle EMG amplitudes in FDI. Only model neurons located within the hand-knob were scrutinized (Figure 38). For each stimulus experiment, $\mathcal{F}(\boldsymbol{\nu}_{\mathrm{HK}}, \bar{v})$ was calculated (Figure 39). k values (Eq. 32) were found to be directly proportional to stimulus intensity (Table 5) but less in magnitude for monophasic stimulation.

Table 5 *k* Constant for Model Prediction. Value of the constant (*k*) applied in Eq. **32** for predicting EMG amplitude in FDI.

	Biphasic Stimulus		*Monophasic Stimulus*	
Intensity (% RMT)	110	130	110	140
k	0.9	1.0	0.5	0.6

For all stimulus experiments, threshold stimuli of the monophasic pulse were generally less than those from the biphasic pulse (Figure 37).

Our computational model is amenable to time-dependent visualizations of population responses for stimulus experiments (Figure 38). The total surface area of the pial surface that contains modeled pyramidal cells was 6454 sq-mm (64.54 sq-cm). Of this area, the neurons within the hand-knob occupied 696 sq-mm (Figure 38).

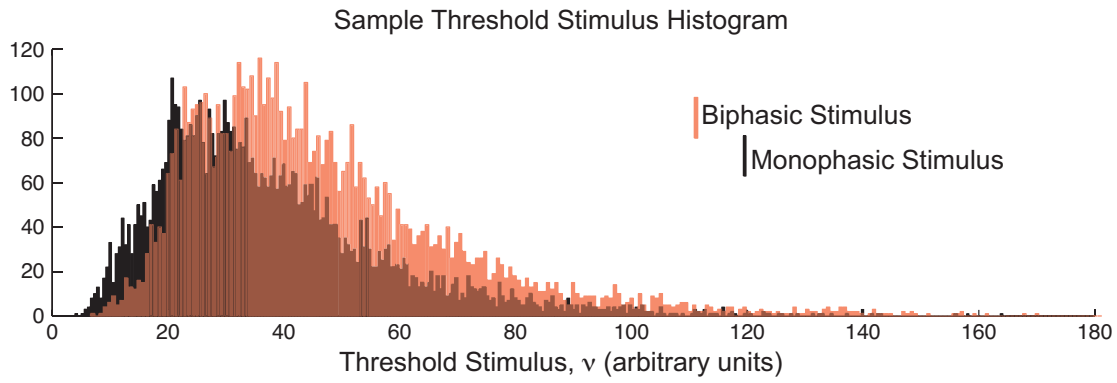

Figure 37 Histogram of Threshold Stimuli of Modeled Pyramidal Cells. A sample histogram from a stimulus experiment (*biphasic @ 130% RMT -18°*) is shown to demonstrate threshold stimulus distribution among pyramidal cell simulations. All 6111 pyramidal cell thresholds were placed in 300 bins according to threshold stimulus values.

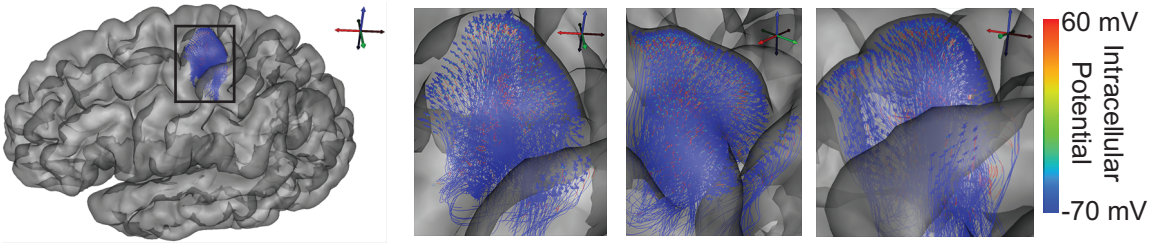

Figure 38 Pyramidal Cells Located Within the Hand-knob Area. Pyramidal cells within the hand-knob are shown colored according to intracellular potential @ t = 1ms post stimulus (*biphasic @ 130% RMT -18°*). The cells shown here occupy 696 sq-mm of the pial surface.

Model predictions ($\mathcal{F}(\boldsymbol{\nu}_{\mathrm{HK}}, \bar{v})$; Eq. 34) were found to follow the general trend of the FDI EMG amplitude with changing coil orientation (Figure 39). Predictions and electrophysiology were presented in terms of the coil orientation (rotation angle about the coil-plane normal vector), which is one of six degrees of freedom. It should be noted that minor differences in coil placement exist between stimulus experiments.

Using MATLAB, we employed a linear regression model fit and F-test to quantify model prediction strength (Figure 40); model predictions were corroborated by electrophysiology ($p < 0.0001$). The model cannot forecast (or quantify) the precise EMG amplitude so a validated model of the physics and physiology of TMS should supply a quantitative prediction that agrees with the physiological response measure (FDI EMG)

relative to changing stimulation parameters. We assumed that the robustness of the EMG response was proportional to the population size of recruited motor neurons. Model predictions poorly reflected lower EMG amplitudes (Figure 39), especially for those orientations <-135º. Conversely, the model predicted a slight change in mean EMG amplitude over a small coil orientation change (Figure 39, *biphasic @ 110% RMT*). Though coil orientations closest to 0º generally gave rise to robust physiological responses and $\mathcal{F}$ values, the model predicted an attenuated response from -80º to -15º for the *monophasic @ 110% RMT* stimulus experiments (Figure 39).

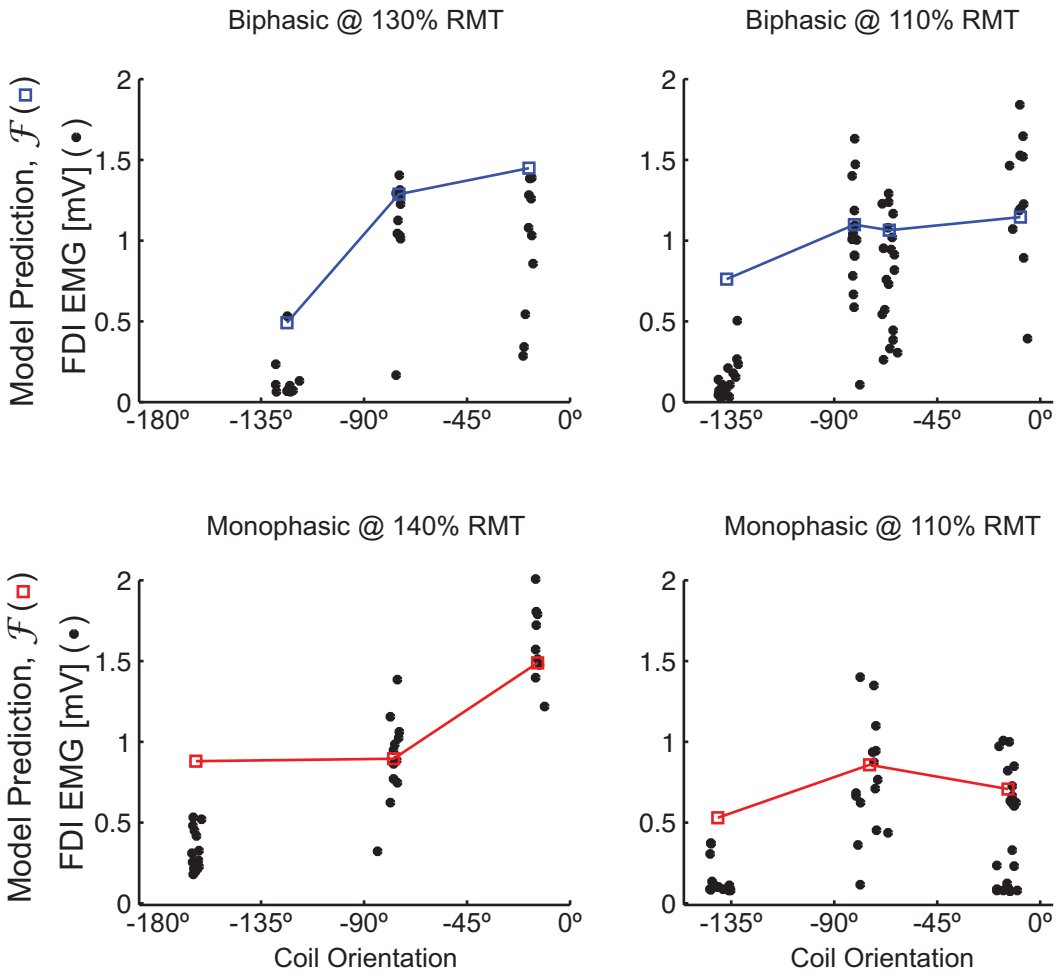

Figure 39 EMG vs. Coil Orientation Superimposed with Model Results. Muscle EMG (*black dots*) results are shown with model predictions (*colored squares*) for all orientation experiments. Biphasic and monophasic stimulus model predictions are shown in blue and red, respectively.

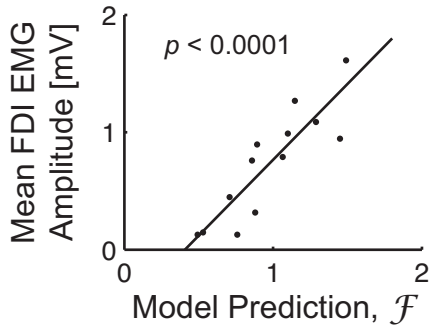

Figure 40 Linear Regression of Mean FDI EMG Amplitude vs. Model Predictions. The linear regression model is shown with F-test p-value to demonstrate model prediction significance.

Of the entire section of the modeled pial surface, a maximum area of 4000 sq-mm contains neurons having thresholds below $\bar{v}$ during monophasic stimulation and 3100 sq-mm during biphasic stimulation (Figure 41A).[51] Model simulations indicate a 1000 sq-mm ($A_{v<\bar{v}}$) difference in area of activation between -18º and -124º coil orientations for biphasic stimulation. We observed a strong correlation between EMG amplitude and $A_{v<\bar{v}}$ value within the hand-knob for biphasic stimulation (Figure 41A).

The threshold value, v, was employed as an excitability measure. The threshold stimulus maps (Figure 41B) were detailed and complex. Significant differences were apparent between biphasic and monophasic threshold maps. Similarly, threshold maps between -124º (Figure 41B, *left*) and -75º (Figure 41B, *middle*) showed substantial differences in excitability. Minor discrepancies were observed between -75º and -18º (Figure 41B, *right*) excitability maps. The excitability of neurons within the post-central gyrus had threshold values similar to those for neurons within the hand-knob (Figure 41B; *-18º*) for both biphasic and monophasic stimulation.

---

[51] In order to compare thresholds between monophasic and biphasic stimulation, we set $\bar{v}$ equal to $\mathrm{median}(\mathbf{v}_{\mathbb{U}})$. In other words, threshold stimuli below $\bar{v}$ are in the bottom 50% of $\mathbf{v}_{\mathbb{U}}$. Here, $\mathbf{v}_{\mathbb{U}}$ is a 158,886 element vector array (6111 neurons; 13 stimulus experiments; 2 waveforms). The specific (unitless) quantities of $\mathrm{median}(\mathbf{v}_{\mathbb{U}})$, $\mathrm{mean}(\mathbf{v}_{\mathbb{U}})$, and $\mathrm{STD}(\mathbf{v}_{\mathbb{U}})$ were 40.0, 45.0, and 24.1, respectively.

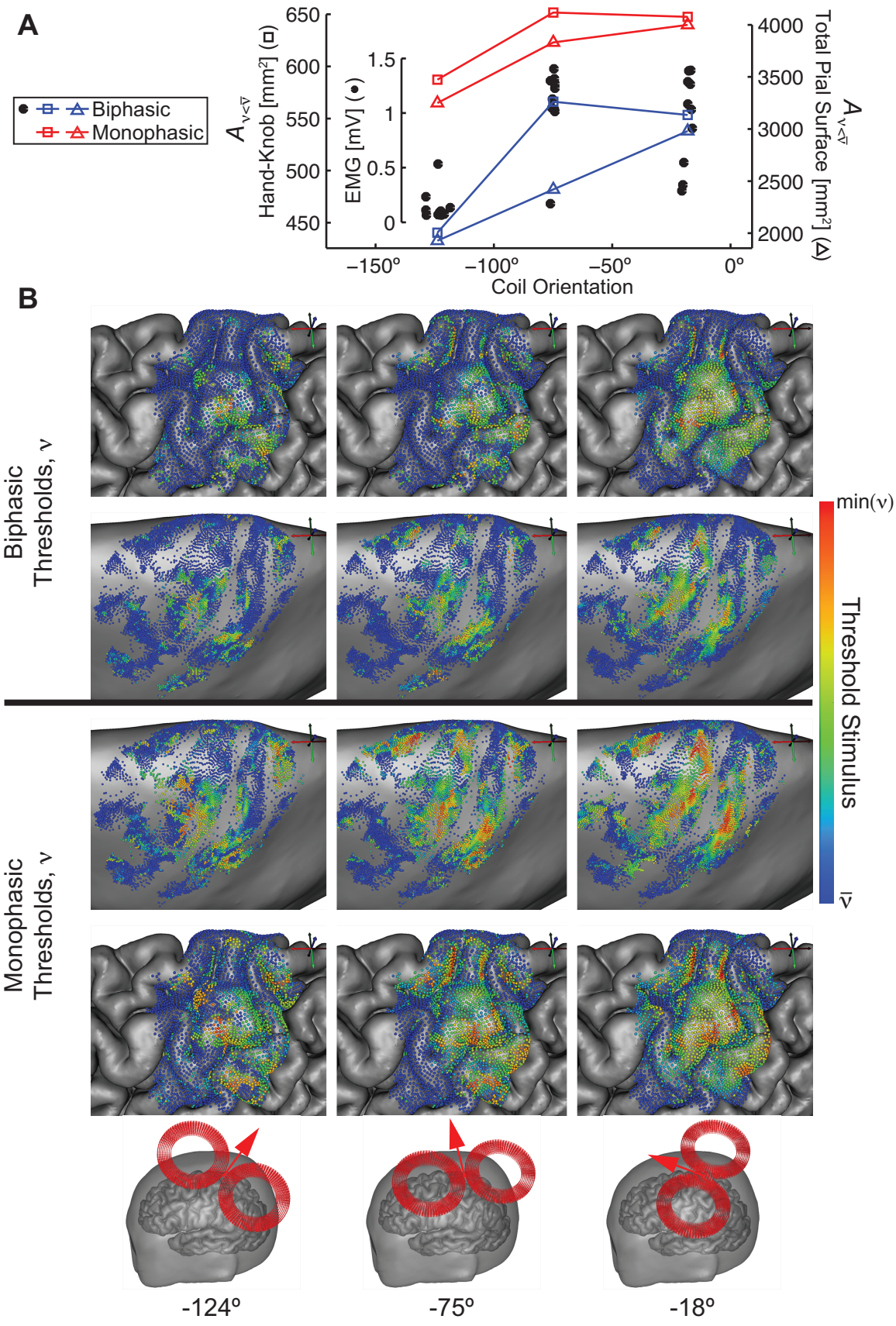
A
Biphasic
Monophasic
650
600
550
500
450
Hand-Knob [mm²] (□)
1.5
1
0.5
0
EMG [mV] (●)
4000
3500
3000
2500
2000
Total Pial Surface [mm²] (Δ)
−150°
−100°
−50°
0°
Coil Orientation
B
Biphasic Thresholds, ν
Monophasic Thresholds, ν
min(ν)
Threshold Stimulus
ν
-124°
-75°
-18°

Figure 41 Excitability Maps for Three Coil Orientations. (*A*) Surface area containing neurons with thresholds below $\bar{\nu}$ within the hand-knob and within the total analyzed surface is overlaid with EMG response amplitude in FDI. (*B*) Surface nodes represent neurons beneath the pial surface. Nodes are colored according to the threshold stimulus. Here, the threshold, ν, is employed as a measure of the excitability. In this sense, red nodes are neurons that were found to be most excitable (low thresholds) whereas blue nodes indicate neurons that were found to be least excitable (high thresholds). Nodes are shown on both the folded pial and inflated pial surface. (*Bottom*) Coil orientations corresponding to color maps are shown column-wise. Coil orientations correspond to model outcomes in (*A*). Arrows point in the direction of the induced E-field at the stimulus onset.

Sites of high excitability were found to be more sporadic with a -124º orientation. Our results suggest that it would be difficult to target the hand-knob while avoiding other areas using the figure-8 coil. Furthermore, excitability maps show complex details that depend on cell morphology.

We compared thresholds between monophasic and biphasic stimulation (Figure 42) and found the biphasic waveform to be more efficient than the monophasic waveform. The minimum slope of biphasic versus monophasic threshold (0.58) was found to be precisely the ratio between the induced E-field strength of biphasic and monophasic waveform (approx. 0.6:1) (Figure 42). Monophasic thresholds rarely defied this ratio:

$$\left|\mathbf{E}_{monophasic}\right| = 0.60 \cdot \left|\mathbf{E}_{biphasic}\right| \qquad \text{(Eq. 37)}$$

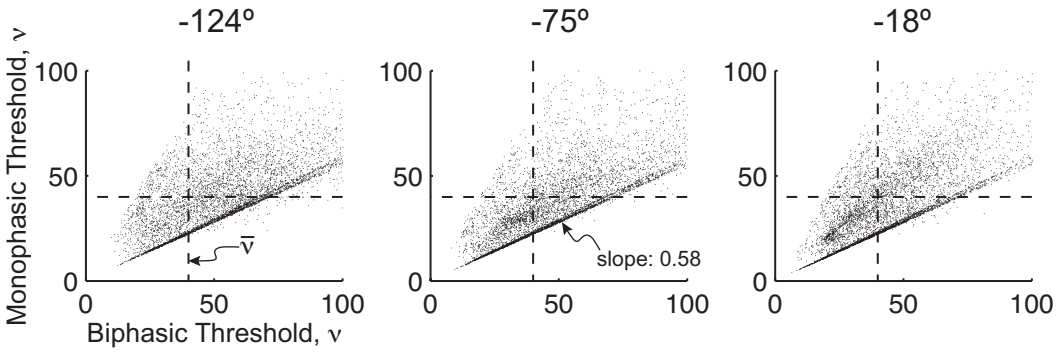

Figure 42 Monophasic Threshold vs. Biphasic Threshold. A comparison between thresholds from monophasic and biphasic stimulation is shown for all neurons for three stimulus experiments (*biphasic @ 130% RMT*). The dense data points have a slope that represents the E-field strength ratio of biphasic to monophasic stimulation.

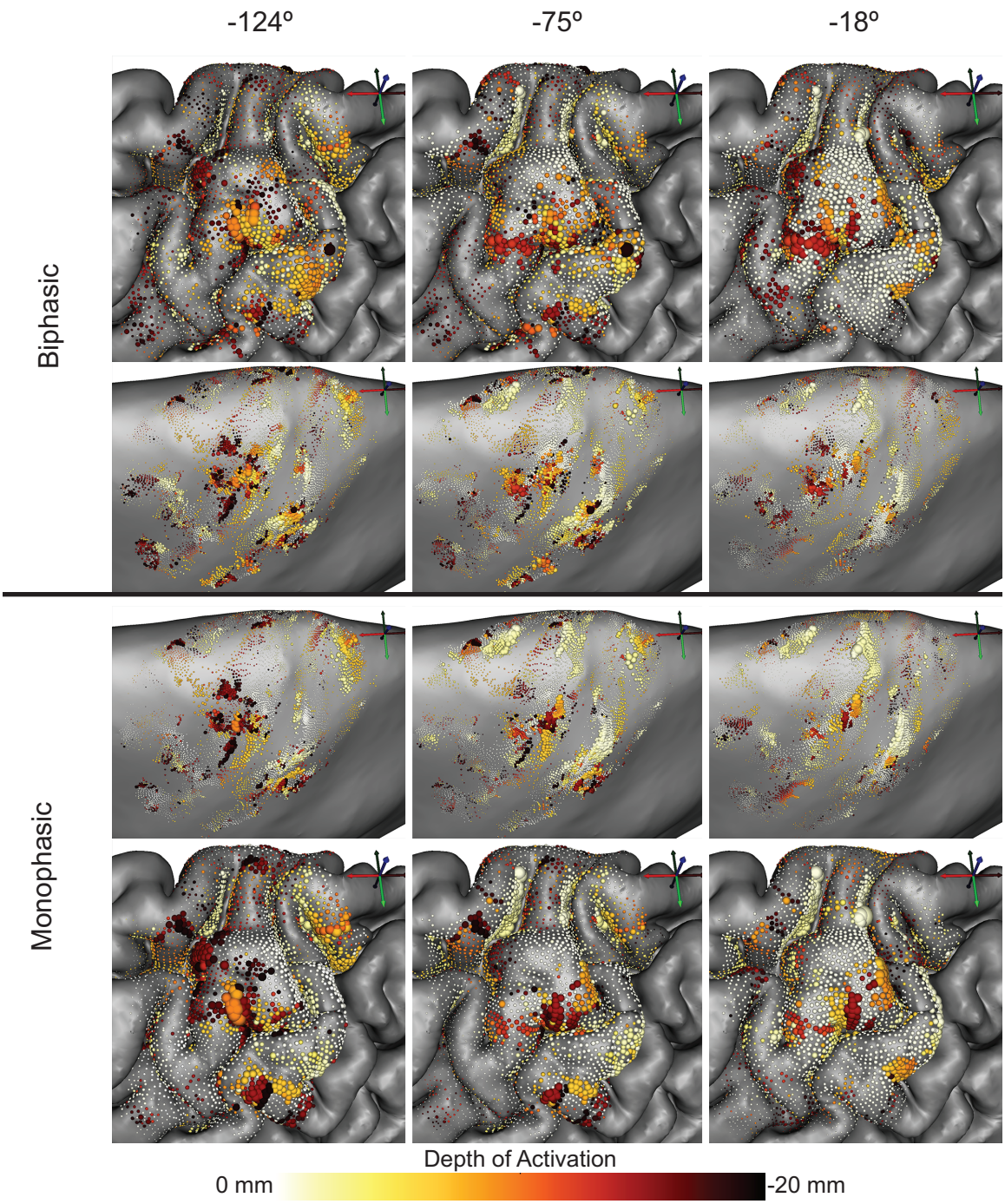

Figure 43 Pial Surface Maps of Depth of Activation. Each surface node represents a single neuron directly underneath the pial surface. Nodes are shown on both the folded pial and inflated pial surface. Nodes have been colored according to depth of activation relative to the pial surface. Node resizing was done to emphasize those neurons that were found to be more excitable, i.e., node size is inversely proportional to threshold (size $\propto 1/v$). In this sense, a large node indicates a *low* threshold stimulus. Surfaces are shown for both the biphasic and monophasic stimulus.

In contrast, biphasic thresholds often defied the ratio of Eq. 37, which suggests that E-field strength plays only a partial role in exciting pyramidal cells, but that the waveform is critical to the extent of stimulation.

We measured the depth of activation relative to the pial surface along the axis of the pyramidal cell and found that depths of activation from monophasic stimulation are shallower on average than those from biphasic stimulation (Figure 43). In general, the axon was more sensitive to the biphasic stimulus compared to the monophasic stimulus (Figure 43). Activation sites in the dendrites were more common from monophasic stimulation compared to biphasic stimulation. Similar to excitability maps, activation depth maps were found to be complex and detailed. Our results indicate that activation depths within the hand knob are deeper for -124º compared to -18º on average. However, depths increased from -124º to -18º within the sulcal wall on the posterior side of the hand-knob.

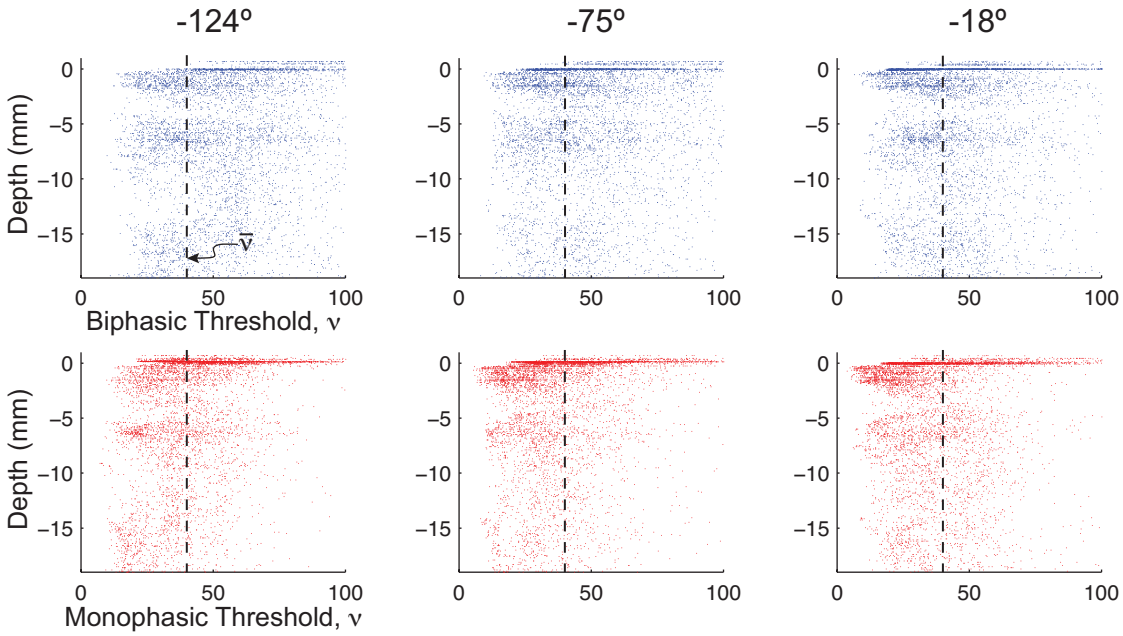

Figure 44 Depth of Activation vs. Threshold Stimulus. Scatter plots of the depth of activation relative to threshold stimulus (*blue*: biphasic; *red*: monophasic) for modeled neurons. Depth is shown relative to the soma (0 mm), which is positioned approximately 1.5 mm into the gray matter. Depth values below zero indicate axon activation and those above zero indicate activation in the ascending dendrites.

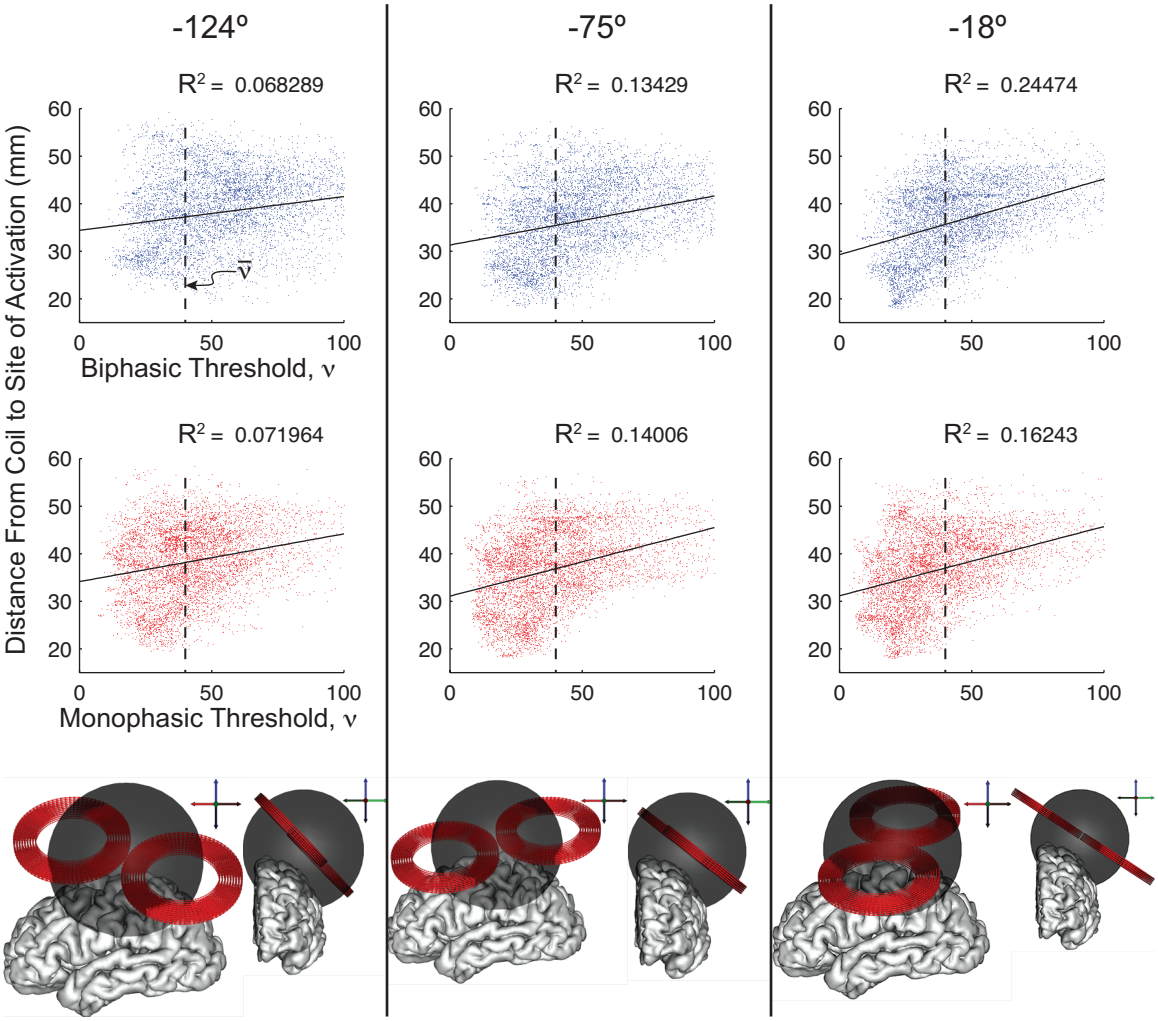

Figure 45 Distance from Coil to Point of Activation. Scatter plots portray distance from the center of the coil to the point of activation for three coil orientations from 130% RMT biphasic stimulus experiments. Model simulation results are shown for both the biphasic (blue) and monophasic (red) case. Coefficients of determination (R^2) are shown to demonstrate the lack of relationship between threshold stimulus and the reach of the coil. Here, $\bar{\nu}$ is the median ν of all plotted data points. (*Bottom*) A sphere illustrates the reach of the coil for each orientation. The radius of the sphere is equal to the maximum distance (54 mm @ -18º; 56mm @ -75º; 59 mm @ -124º) below $\bar{\nu}$.

The depth of activation showed no correlation with stimulus threshold (Figure 44). Interestingly, there was also no significant correlation between threshold and coil distance from activation site (Figure 45). Nevertheless, an increase in distance generally resulted in an increased threshold.

The dense cluster of points near 0 mm (Figure 44) indicates that many neurons are oriented within the gray matter in such a way that activation occurred within the axon

hillock. However, the 0 mm mark is an ambiguous reference point since basal dendrites also extend into this region. Threshold stimuli were found to be comparably larger when activation initiated within the dendritic tree (depth > 0 mm).

To illustrate sites of activation in the brain, we generated a point cloud of locations where action potentials initiated for two stimulus experiments (Figure 46; *biphasic @ 130% RMT, -124º & -18º*). Activation sites contained substantial discrepancies between waveform stimuli and coil orientation (Figure 46). Unintended activation sites (outside of hand-knob) were widespread. These results suggest that widespread untargeted cortical elements experience excitation at thresholds comparable to those within the hand-knob.

The coil orientation was found to have an influence on the latency of soma depolarization. The latest depolarizations resulted from activation at depths > 15 mm in the axon. Latencies in the mid range (2 ms < t < 6 ms) were found to be due to activation originating in dendrites or at various depths of the axon.

Depth of activation was related to the soma depolarization latency, except in the case of dendritic activation, and sites of activation within the white matter caused propagation of efferent and afferent action potentials. Model results show a 7 ms range of soma depolarization latency. It should be noted that the depolarization latency is not proportional to the latency of efferent signals that would be observed in the pyramidal tract because of the bidirectional propagation of action potentials when the axon is activated. For example, excitation in the axon could cause soma depolarization at the same latency resulting from dendritic excitation. The minimum latency was 0.6 ms. The earliest depolarizations resulted from activation of the axon hillock, which was more common at lower biphasic threshold stimuli. The monophasic stimulus caused no

activation in axon hillocks ($\nu > \bar{\nu}$ for latencies < 0.7 ms) for coil orientations of -75º and -18º (Figure 47, *bottom*).

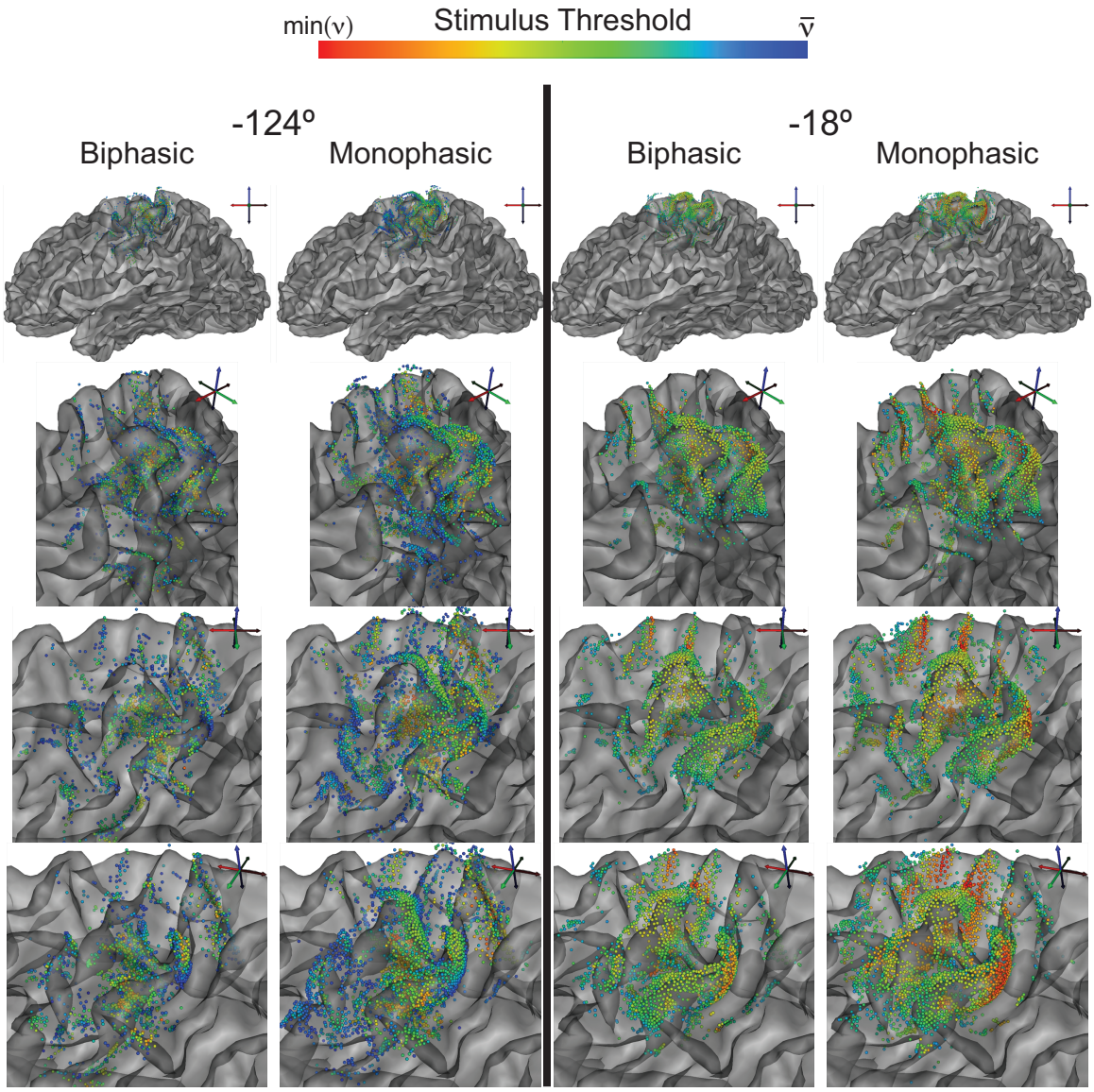

Figure 46 Sites of Action Potential Initiation. Sites where action potentials initiated are shown in the form of point clouds relative to the white matter surface. Point cloud nodes have been colored according to stimulus threshold. Nodes from neurons where $\nu > \bar{\nu}$ have been removed. Model simulation results are shown for two stimulus experiments (column-wise) for biphasic and monophasic stimuli.

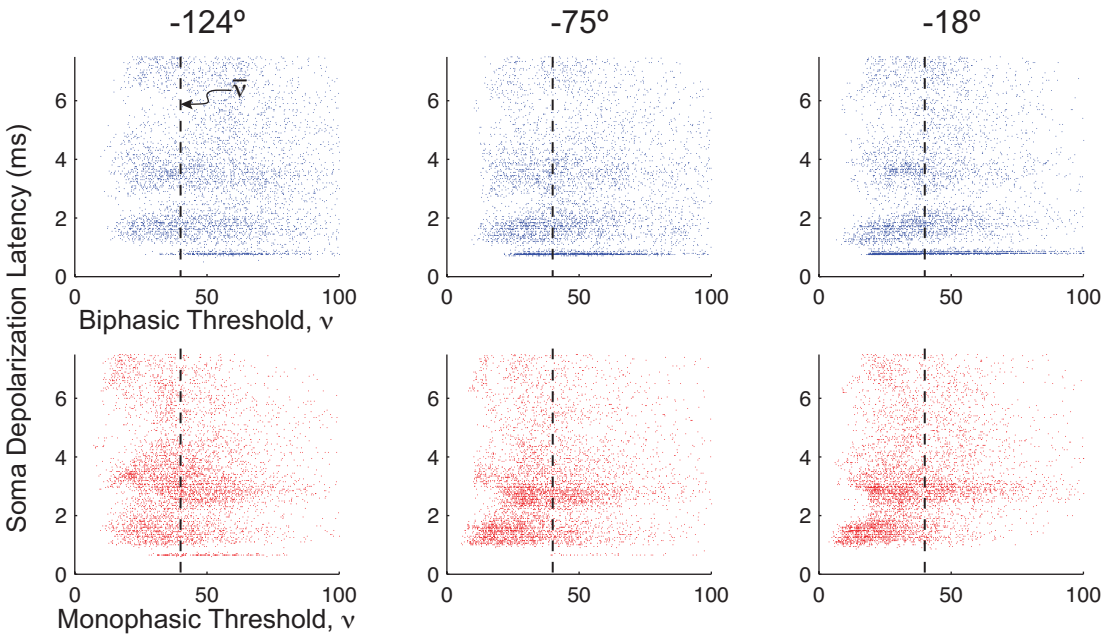

Figure 47 Latency of Soma Depolarization vs. Threshold Stimulus. Soma depolarization at threshold stimulus occurs at latencies as long as 8 ms.

We measured the effect of anisotropic conductivity on the threshold stimulus and found that fractional anisotropy (FA) has a minor influence on the threshold (Figure 48). Though insignificant, thresholds were found to generally decrease with increasing FA. However, it remains to be seen whether or not a change in tensor properties has a direct impact on the threshold. It would make sense that the conductivity along the principle eigenvector would influence the threshold since it is heavily dependent upon the axial E-field (Basser & Roth, 1991). Moreover, the axon tractography algorithm (Westin et al., 2002) we employed relies on the principle eigenvalue. Therefore, an increase in the principal eigenvalue along an axon would result in a compensatory decrease in the E-field.

Based on coefficients of determination (R^2), the threshold stimulus shows a small dependence upon E-field magnitude at the site of activation (Figure 49). The y-intercepts and slopes of linear trend lines (Figure 49) indicate that biphasic E-fields caused stimulation at lesser magnitudes compared to monophasic induced E-fields. Trend line

slopes were minimal for the -18º coil orientation, which corresponds to the stimulus experiment that yielded the most robust physiological response (Figure 39, *biphasic @ 130% RMT*). These results demonstrate that pyramidal cells are sensitive to directional and time-dependent properties of the induced E-field and *not* the E-field magnitude alone. Our results suggest that the E-field should not be the only consideration when predicting activation sites.

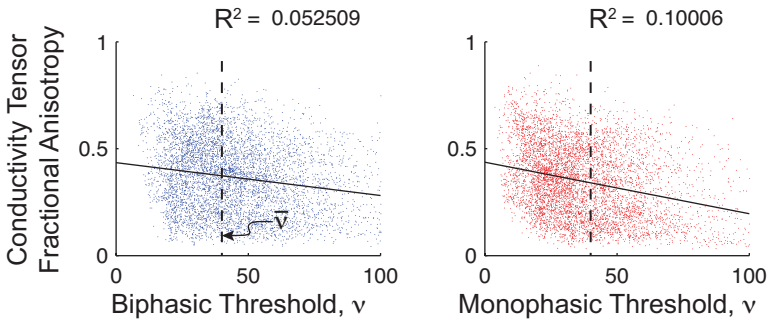

Figure 48 Conductivity Tensor Fractional Anisotropy at Activation Site vs. Threshold Stimulus. Threshold stimulus shows a minor dependence on FA value for all coil orientations. Model results from the 130% RMT stimulus experiment (-18º) are shown for both biphasic and monophasic stimuli. These data typify results from all stimulus experiments.

Finally, we compared predictions of pyramidal cell thresholds with predictions from the cortical column cosine (C^3) model (Figure 50). The C^3 model and its respective variants have been employed for predicting activation and comparison with physiology (Fox et al., 2004; Opitz et al., 2013). The C^3 model outcome measure is defined as the E-field component in the direction of cortical hypercolumns or the “effective E-field” ($\mathbf{E}_{\mathrm{eff}}$).

Our model predictions indicate weak correlations with the C^3 outcome measure. The correlation of the measure with monophasic thresholds was found to be greater, on average, than with biphasic thresholds. This relationship was most apparent for the -18º monophasic pulse. The C^3 model does not account for deeper sites of activation, which

is an important feature of our multiscale approach. These results suggest that the C^3 model is not a comparable representation of the pyramidal cell population model.

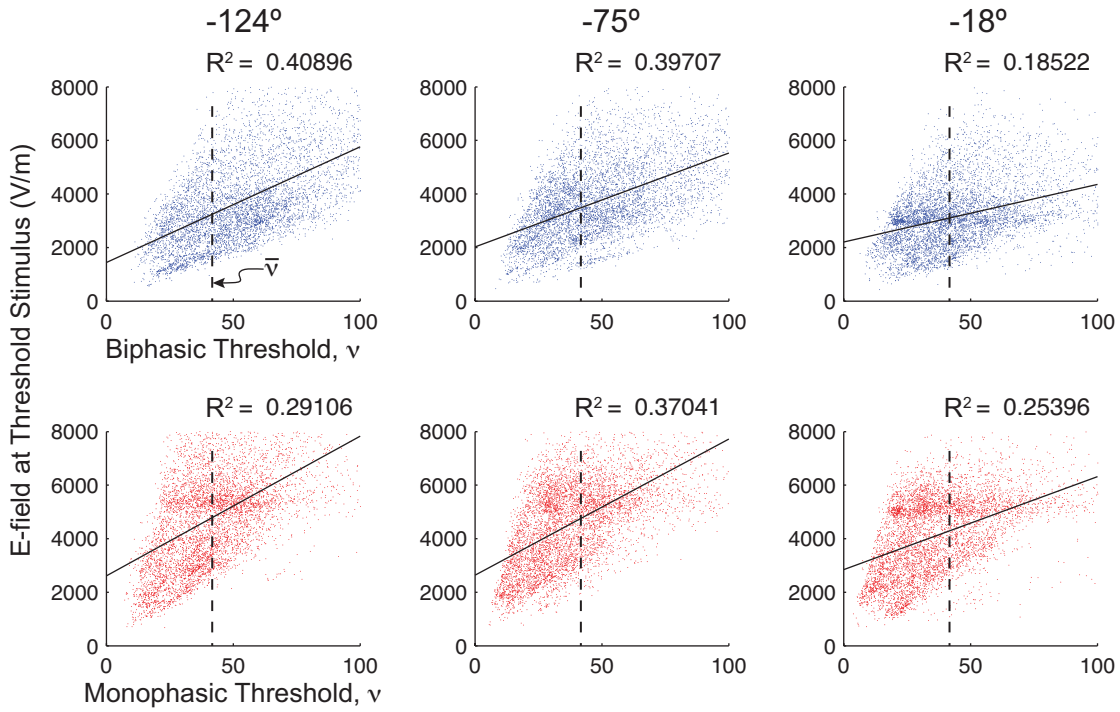

Figure 49 E-field Magnitude at Site of Activation vs. Threshold Stimulus. Magnitude of threshold E-field at activation site is shown relative to the stimulus threshold.

DISCUSSION

Motor Cortex Stimulation

Di Lazzaro et al. (2004) report observations that indicate the orientation of fibers in the hand-knob area is susceptible to stimulation from posterior-to-anterior (PA) current flow. The PA orientation corresponds to 0º for the figure-8 coil according to our angle convention. Both our model simulations and MEP recordings confirm this notion, which also seems apparent from previous studies (Sakai et al., 1997; Werhahn et al., 1994). Axon tractography within the hand-knob indicates that pyramidal cells are oriented in a way that favors depolarization during PA current flow from a monophasic stimulus.

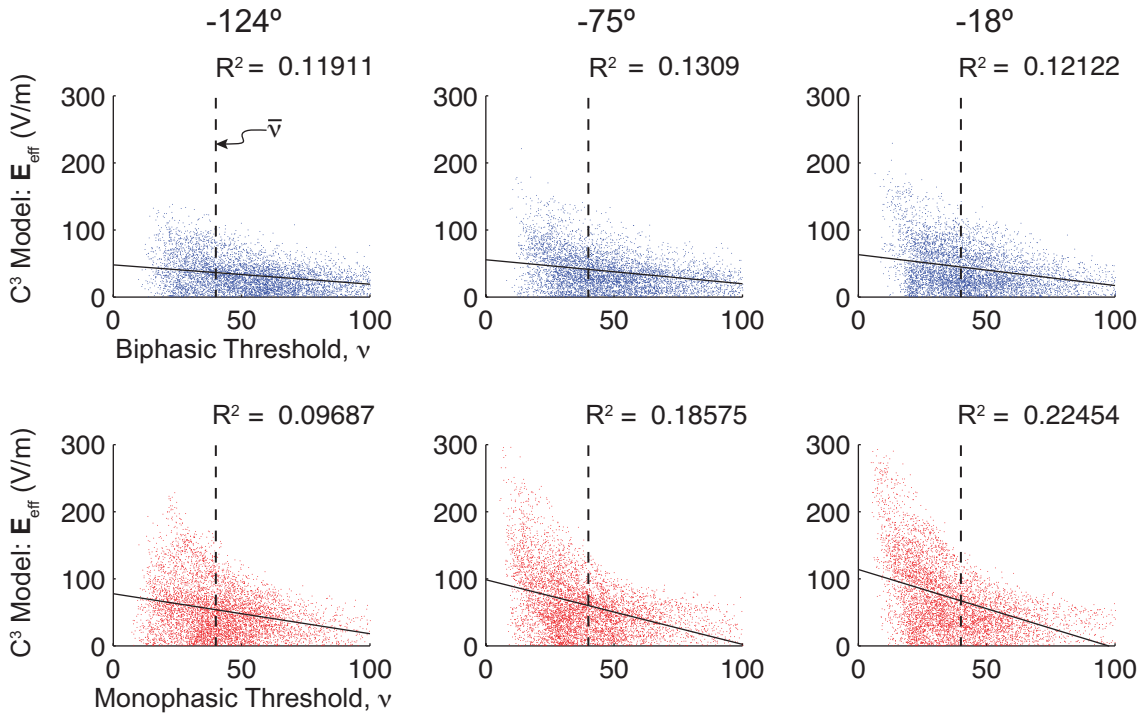

Figure 50 C^3 Model Measure vs. Threshold Stimulus. The cortical column cosine (C^3) model prediction is the "effective E-field" ($\mathbf{E}_{eff}$), which is equivalent to the component of the E-field in the direction of the extending apical dendrites or hypercolumns normal to the pial surface. Though all trend lines indicate negative slopes as expected, R^2 values indicate that the models are incompatible. Comparisons between the C^3 E-field and pyramidal cell thresholds are shown for the three stimulus experiments (*biphasic @ 130% RMT*).

We reported results from one of four subjects, and data between subjects contained no significant differences in the MEP variability. FDI EMG response latencies agreed with previous publications that reported latencies between 20 and 26 ms (Di Lazzaro et al., 2001; Sakai et al., 1997). This range of latencies appears in modeled stimulations (Figure 47). In fact, model predictions of depth of activation (Figure 44) and soma depolarization latency (Figure 47) corroborate observations by Di Lazzaro et al. (2001) and Sakai et al. (1997) who note an earlier latency of 4 ms with PA (0°) coil orientation compared to anterior-posterior (AP; 180°) coil orientation (using a monophasic stimulus). Figure 44 (*bottom*, *red*) illustrates a possible reason for this phenomenon. Model simulations indicate that a coil orientation of -124° (approx. AP)

tends to excite ($\nu < \bar{\nu}$) dendritic elements (depth > 0 mm) as opposed to the axon, whereas -18º results in a large number of neurons experiencing activation near the axon hillock or initial segment (-3 mm < depth < 0 mm). Later latencies would correspond to I-wave recruitment and earlier latencies to D-wave recruitment.

Our model expressed aspects of the EMG response variability through soma depolarization latency (Figure 47). A large sample of neurons showed latencies between 1 ms and 4 ms for a PA orientation (Figure 47, *bottom*, *right*) whereas an AP orientation (Figure 47, *bottom*, *left*) resulted in later, more sporadic response latencies. These results do not fully capture the latency that would be observed within the hand-knob. Conversely, it would be expected that early latencies would be observed with deep activation. More work is necessary to enable forecasting the response that would be observed in the medullary pyramid. Further investigation could be done to better understand recruitment size from stimulation and how it interacts with lower motor neurons in the brainstem.

Kammer et al. (2001) compared the effectiveness of the monophasic stimulus with the biphasic stimulus and found that the biphasic waveform achieves stimulation of the motor cortex more efficiently. Additionally, Kammer and colleagues found that the biphasic stimulus is more effective with an AP (180º) coil orientation. This technique utilizes the second, more powerful, phase of the waveform, which would then induce current in the PA direction. We did not observe this phenomenon during TMS of human motor cortex, but it might have been apparent had I employed coil orientations that exceed -180º (e.g., -200º). Model simulations supported the findings of Kammer et al. (2001) (Figure 49; cf. Figure 42). Though threshold stimuli were found to be generally lower for monophasic stimulation, the magnitude of the E-field at the stimulation site was found to be significantly less during biphasic stimulation, which is reflected by both the

slope and y-intercept of scatter plot trends in Figure 49. It remains to be seen how different waveforms influence various neural elements. Though the parameter space for waveform design is infinite, further research in waveform design could enable selective targeting of specific neural elements.

Cortical Model

We found the FEM to produce E-field estimates in agreement with previously published work. While these results suggest that anisotropic conductivity is a necessary model component (Figure 35), two published models have attempted to integrate DTI to model anisotropic conductivities of the head (De Lucia et al., 2007; Opitz et al., 2011). Electromagnetism theory requires the E-field to increase when the current flows in resistive directions. Apart from the inclusion of a DTI conductivity model, essential features in the E-field for predicting activation would be absent. Our model generated more detailed E-field estimates than isotropic modeling approaches (Chen & Mogul, 2009; Laakso et al., 2014; Salinas et al., 2009; Thielscher et al., 2011).

In a previous iteration of our head FEM[52], we employed an isotropic medium and found that the E-field estimate differs from that using an anisotropic medium, which shows that the E-field is more concentrated at depths up to 25mm within the targeted gyrus when current flow is induced perpendicularly to the targeted gyrus (Figure 35). This phenomenon affected neuron model simulations by a decrease in thresholds and deeper activation within the hand-knob (Figure 43). Our anisotropic FEM results confirm physiological observations that show an increase in D-wave recruitment during PA current flow compared to lateral-medial current flow (Dubach et al., 2004), and they provide an explanation for the effectiveness of PA current flow for exciting neurons in the

[52] See Chapter 2, p. 70.

hand-knob (Figure 46). The PA coil orientation has been a general guide for targeting the hand-knob, but now, through our subject-specific, anisotropic model, the effectiveness of PA current flow can be quantified and explained.

Neuron thresholds were computed relative to the actual stimulation intensity as would be dialed on either the Magstim 200 (monophasic) or Magstim Rapid (biphasic) stimulator units. Consequently, thresholds for the monophasic waveform were found to be typically lower. On the other hand, the peak E-field during the biphasic stimulus at threshold was found to be typically less than that of the monophasic pulse (Figure 49), which suggests that the biphasic waveform requires less energy to cause excitation of pyramidal cells, possibly due, in part, to the stimulus giving rise to bi-directional transmembrane fluctuations. Cell compartments influenced by the biphasic stimulus experience both hyperpolarization and depolarization. The depolarizing phase may be responsible for pushing the transmembrane potential above the threshold of the voltage-gated ion channels.

Our results suggest that the reach of TMS is uncorrelated with neuron thresholds (Figure 45). In other words, neurons that are closer to the TMS coil are *not* necessarily more susceptible to stimulation. For all tested coil placements, neuron stimulations indicated that neurons closest to the coil center have comparable thresholds to neurons at least 50 mm from the coil center.

Previous studies have modeled stimulation sites as a function of the E-field direction relative to hypercolumns or pyramidal cells in the cortex. Opitz et al. (2013) and Fox et al. (2004) surmise that activation sites can be explained in terms of the current flowing axially along hypercolumn orientations or in the direction of the principal eigenvector of the diffusion tensor (as from DWI). Laakso et al. (2014) generated a highly detailed FEM of the head and have similarly hypothesized that potential sites of

activation can be explained in terms of a cortical column cosine model. However, these models are limited to cortical E-fields. Our results suggest that no significant correlation exists between pyramidal cell activation thresholds and E-field direction along pyramidal cell orientation (Figure 50). Neurons within the hand-knob situated on the gyral crown were found to have similar thresholds to those with sharp bends situated within sulcal walls (Figure 41 & Figure 46). Additionally, neurons situation in gyral crowns were more prone to deeper (> 10 mm) activation. However, a general trend between pyramidal thresholds and the C^3 model was apparent in the case where the primary induced E-field is perpendicular to the central sulcus (Figure 50; *-18°*).

We compared the population response of neurons to FDI EMG amplitude, which does not fully represent the size of motor neuron recruitment in the hand-knob during in-vivo TMS. Perhaps model comparisons could be further validated by more thorough use of EMG responses throughout muscles. Model validations could be expanded as a function of multiple muscle EMG responses within the hand. If our modeling approach is further validated by a more sophisticated method, it may be possible, for example, to map the hand-knob with sub-millimeter resolution, and inferences can be made about network interactions using DWI. With advancements in the NIH Human Connectome[53] project (Setsompop et al., 2013), our approach could enable precise predictions of activated areas and provide new insights to better understand both the pathophysiology of neurological disorders and the extent of neuromodulation.

Model comparisons were limited in that a quantification of possible inhibitory responses is absent from the model. Were inhibitory neurons (or responses) adequately accounted for, the model prediction would inevitably change. More work is needed for

---

[53] A project funded by NIH with the overall aim to map the human brain (http://www.humanconnectomeproject.org/).

the development of these details. However, we elected to include a model weight (ω) to account for the net inhibitory response of the neuron population. Model weights quantify this measure in a coarse, non-specific manner, but the average response of neurons having a threshold (ν value) is greater than one standard deviation. Neurons with considerably high thresholds experience pronounced hyperpolarization in either dendritic branches or axon. We tried to capture this inhibitory effect through a model weight, which is a function of the inverted product of threshold mean (μ_ν) and variance (σ_ν^2) (Eq. 35). Hyperpolarizing responses are reflected in these statistical measures for a Poisson distribution. If model predictions ($\mathcal{F}(\boldsymbol{\nu}_{\mathrm{HK}}, \overline{\nu})$) were a function only of $A_{\nu<\overline{\nu}}$ (Eq. 33), which describes only the area of cortex containing neurons below $\overline{\nu}$ (Eq. 32), the distribution of ν is neglected. Model weights described distinguishing features between stimulus experiments. High σ_ν^2 and μ_ν indicated a net hyperpolarizing response within the neuron population. Conversely, low σ_ν^2 and μ_ν reflected a net depolarizing response of the neuron population. It is possible that the model weight provides a description of the recruited motor pool size within a cortex ROI (such as the hand-knob). The inclusion of a model weight resulted in modest, yet compensatory changes in the model prediction trend compared to a prediction that is restricted to the $A_{\nu<\overline{\nu}}$ value. Furthermore, the presence of a model weight resulted in a model prediction that was found to better describe the measured MEP.

Our results show that waveform shape design has significant implications in terms of stimulation efficiency and cortical sites of activation. Monophasic pulses seem to preferentially excite cells that are oriented such that only depolarization, not hyperpolarization, can occur. Our results suggest that a biphasic waveform would excite neurons in a similar manner as the monophasic pulse if the coil could be oriented in two opposing directions at once (e.g., 0º and 180º). Depending on the desired target, it

would be advantageous to consider waveform design. A target that includes a gyrus and adjacent sulci would be amenable to a biphasic stimulus. On the other hand, a monophasic stimulus would selectively target a neuron oriented in such a way that its apical dendrite is oriented *into* the induced E-field and its axon bends sharply into the white matter volume.

Though model predictions appear to support findings from previous studies and correlate with trends that follow observations from electrophysiology, our modeling approach contains limiting assumptions. Most simulated E-fields that cause excitation were unrealistic (Figure 49), a possible consequence of model limitations. We assumed that direct activation during TMS could be modeled by stimulating neurons at resting state, which is approximately -70mV for our pyramidal cell model. We also performed neuron simulations using an adaptation of well-established techniques in modeling DBS activation in axons (Butson et al., 2007; Chaturvedi et al., 2010; McIntyre et al., 2004). Both native and custom extracellular mechanisms were employed within NEURON to simulate pyramidal cell responses and determine their activation threshold stimulus. Further investigation into what an ion channel actually "sees" in adjacent extracellular and intracellular space during TMS could address the current model limitations.

Only one type of cell was used to compute estimates of the excitability of a large area of cortex (65 sq-cm of pial surface). Even though many types of cells experience effects from TMS, our cortical model is limited to clones of a single pyramidal cell. The size of this particular cell model is dwarfed by Betz cells,[54] which are almost certainly targets of D-wave and I-wave recruitment (Vaalto et al., 2010). It remains to be seen whether the cell type would significantly influence our model outcomes.

---

[54] Betz cells are prevalent gigantopyramidal cells in the primary motor cortex. They represent approximately 10% of the pyramidal cell population in the motor cortex. Some Betz cells have soma diameters of 100μm in the human motor cortex.

Precise origins of I-wave recruitment during TMS remain elusive. Our cortical model is limited to investigating D-wave recruitment, and perhaps the first and second I-waves (I1 and I2; between 3 and 5.5 ms). Our model simulations suggest that stimulation of pyramidal cells results in highly variable soma depolarization latencies, and latencies were modulated by changes in activation sites within the dendrites. Model simulations indicate a latency range of 6 ms, which covers the range of the first and second I-waves. However, I3 and I4 waves (6 to 9 ms) are beyond latencies observed in this model. Later I-waves are likely the result of afferent signals from interneurons impinging on pyramidal cells. More work would be necessary to include excitation of interneurons and the resulting excitatory post-synaptic potentials (EPSPs) or inhibitory PSPs (IPSPs) (Maier et al., 2002).

We found that quantifying the physiological response and predicting sites of activation to TMS would be impossible without a multiscale modeling approach due to the size of the TMS coil relative to the size of the neuron structures being stimulated. This dissertation work is the first to bring forth a validated model that incorporates subject-specific, multiscale, anisotropic features to predict the immediate effects and quantify the physiological response of single-pulse TMS. It has potential benefit by enabling the clinician to more precisely prescribe TMS treatment through means that are personalized to his/her patient and the researcher to further investigate the mechanisms of stimulation and better understand targets of activation under given stimulation parameters.

Variability During TMS

We have demonstrated through detailed multiscale modeling that variability in physiological response among subjects is likely due to a number of related factors. Firstly, this study and previously published studies have demonstrated that cortical

geometry influences the induced E-field. Secondly, model results were affected by diffusion coefficients obtained from DWI to model the anisotropic nature of the head. Thirdly, the shape of the pyramidal cell axon has an effect on the depth of activation or the "reach" of TMS. Fourthly, sites of activation at threshold stimulus were variable, even between neighboring neurons. Activation sites were found to vary between individual basal dendrites as well as dendrites extending from the apical branch. Lastly and perhaps most obviously, minor changes in coil orientation resulted in changes in model prediction and EMG response (see Figure 39, *top right*). These factors explain the variability between subjects, *not* within a single subject.

Unknown neural interactions, residual effects from previous stimuli, and refractory effects are undoubtedly contributing factors. To demonstrate the effect of the cell state on its excitability, we revisited the hypothesis set forth by Edgley et al. (1990, 1997). We varied the intracellular (or transmembrane) potential of the soma of two sample neurons exposed to E-fields from a random stimulus experiment (Figure 51). Depending on the site of activation, even an increase in transmembrane potential by 8 mV (via sub-rheobase current injection) can decrease the biphasic threshold stimulus by 45%. Depending on the neuronal target of stimulation, the cell state could influence its threshold stimulus. For example, the biphasic threshold changes equally for both *neurons 1 and 2* (Figure 51) because the site of activation is close to the soma within the axon. On the other hand, the monophasic stimulus causes excitation at a distant point within the axon in *neuron 2*, so the transmembrane potential has no effect on its threshold. For unknown reasons, the monophasic stimulus has a lesser effect on *neuron 1* than the biphasic stimulus. Additionally, the sensitivity of *neuron 1* to activation via monophasic stimulation varied with increasing transmembrane potential.

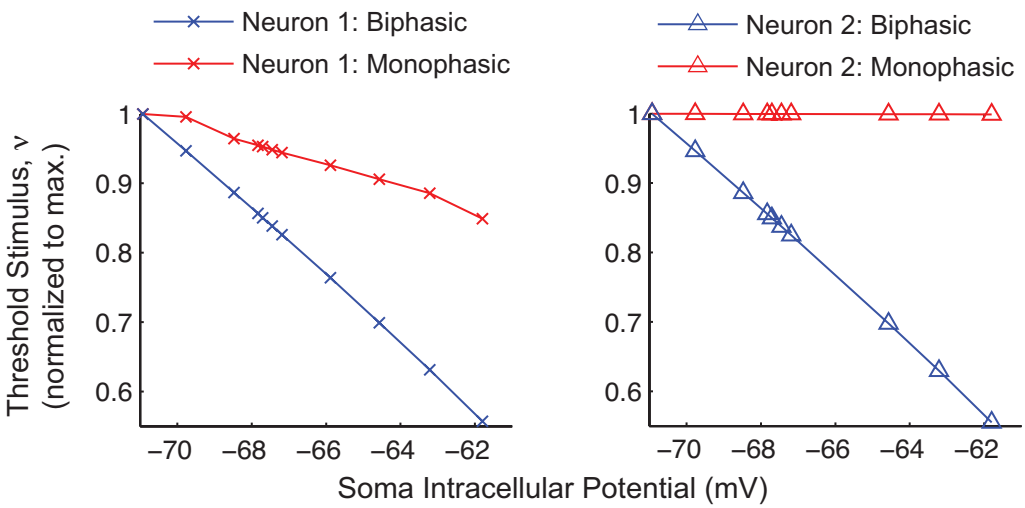

Figure 51 Threshold Stimulus vs. Soma Transmembrane Potential at Stimulus Onset. Threshold stimuli from two model neurons within the hand-knob were found with respect to varying transmembrane potentials at the stimulus onset. Variations in membrane potential substantially affect the biphasic threshold stimulus. The site of activation in *neuron 2* (*right*) via monophasic stimulus occurs deep enough within white matter that changes in soma membrane potential have no effect on threshold.

Thresholds from these two neurons suggest that the cell state plays an important role in its excitability from TMS. However, our approach cannot provide direct estimates of the response variability when the coil placement is unchanging between stimuli.

Burke et al. (1993) report corticospinal volleys from magnetic stimulus in anesthetized humans, and point out that I-waves could not be identified at intensities lower than D-wave threshold. Burke and colleagues found that when isoflurane is withdrawn, I-wave amplitude is dramatically augmented. Based on mechanisms of isoflorane (Hemmings et al., 2005), I-waves appear to originate from corticocortical interactions, which has become a frequently researched hypothesis. The robustness of EMG responses indicates D-wave recruitment, so it is unlikely that I-waves can influence the consistency of the immediate motor response from motor cortex stimulation. Nuclei in the brainstem may cause some of the variability during TMS. Brainstem activity indicates that it participates in performing anticipatory modifications (Drew et al., 2004). Perhaps the state of lower motor neurons affects the signal transmission from upper

motor neurons. Interestingly, the Burke et al. (1993) results appear to show increased variability in D-wave responses in the corticospinal tract when isoflorane was withdrawn, which suggests that an active brainstem could play an important role in the observed variability between TMS stimuli. Future investigations that study the response variability during TMS should include components that can compare activity of brainstem nuclei with the efferent D-wave.

FUTURE DIRECTIONS

Four important future directions or applications of our subject-specific multiscale modeling approach should be considered.

Firstly, the concept of a “dose” in neuromodulation remains to be quantified. Implanted devices deliver constant stimulation when turned on whereas TMS is administered periodically. In some cases, the physiological response is indistinguishable, especially in the case of depression. Do both TMS and a chronically implanted device issue the same “dose” of neuromodulation therapy? Perhaps there is measurable physiological quantity that describes changes in neural activity similar to what is observed during stimulation of the human motor cortex. When stimulation is delivered at even low frequencies, the MEP attenuates and its latency increases over time throughout stimulation. Since clinical TMS is normally carried out in some form of rTMS, the dosage quantity could perhaps be a measure of a difference in neural activity before and after treatment using functional imaging modalities (e.g., MEG). Another potential option is to explain TMS dosage in terms of the energy delivered to the CNS. Even so, this approach begs the question: what exactly is the “energy” and what are its units? This question is appropriate since the scientific community has rather painstakingly demonstrated that activation in the hand-knob, for example, does not depend only on the magnetic and electric energy delivered by the TMS unit. Nevertheless, this energy delivery concept does not necessarily simplify the TMS dosage problem. We propose using our subject-specific multiscale approach as a start. The model could be employed to quantify the “energy” on a per unit area (of pial surface) basis. Perhaps the model prediction quantity, $\mathcal{F}(\boldsymbol{\nu}, \bar{v})$, would provide a unitless prototype to quantify the dosage or energy delivered from TMS. Furthermore, our modeling approach is not limited to TMS, but is translatable across neuromodulation platforms. Its

translatability enables development of a reference point or “gold standard” of therapy. Due to the success of DBS for many disorders, it could be the most logical candidate to provide a reference point for defining the “dose” or “energy” unit.

Secondly, our method could enable prediction of stimulated areas for other neuromodulation paradigms such as tDCS, ECS, and ECT. For example, focal epilepsy resection surgeries employ implantable cortical electrode arrays to identify cortical areas contributing to seizures. Preoperative brain stimulation is carried out via the implanted electrode array. One by one, a suprathreshold stimulus is delivered from each electrode in the array while the corresponding physiological responses are observed. Electrodes that elicit observable spasms are recorded, and these electrodes provide a localization of malfunctioning brain tissue. This brain tissue is then identified by the surgeon, and is ultimately subject to resection. Our modeling approach could provide detailed information about the precise locations and spatial extent of neural activation by the preoperative electrodes and model could be employed to help reduce the possibility of surgical error resulting from using only electrode locations to infer the site and spatial extent of the malfunctioning neural tissue. Therefore, surgery could be performed after having gathered detailed information regarding the precise sites of neural elements to be resected. Further validation of the model is essential for it to be employed for such a serious operation.

Similarly, utilizing the model in conjunction with TMS could meet the need for a reliable, noninvasive, functional brain-mapping tool as an alternative to invasive approaches. Like most methods of neuromodulation, the site of modulation is often elusive. The multiscale approach presented in this work could provide the means to elucidate the site of modulation during TMS. Without information about stimulus targets during TMS, it will remain unfit as a brain-mapping tool. With further advancements, our

model could enable TMS to be reliably employed as an interface to the brain for use in functional brain-mapping. Since functional imaging modalities lack the time constant required to measure the immediate neural response from TMS, our approach would act as a neuroimaging method for brain-mapping.

Thirdly, by virtue of the time-dependent features of our modeling approach, the model could be employed to solve the forward problem for electrophysiology applications such as EEG or MEG. In other words, instead of modeling the effects of electrical stimulation on neural elements, the model could be employed to investigate the effect of various neural activities on electrophysiology transducers such as EEG electrodes or MEG SQUIDs (superconducting quantum interference device). Detailed electrophysiology recordings could be estimated by modeling the activity of a single pyramidal cell or a population of cells throughout a large area of cortex. This experiment could be performed using spatially dependent multicompartmental neuron models such as the pyramidal cell employed in this study. A detailed forward model could improve our understanding of signals recorded by SQUIDs or EEG electrodes. Both SQUIDs and EEG electrodes could be relatively manageable additions to our FEM approach for this forward problem.

Lastly, in regard to stimulation at the cellular level, two high-impact directions should be considered. First, our model has been built (or coded) in such a way that is amenable to experimentation with any cell model that is constructed within the NEURON environment. Comparing the threshold stimuli of the pyramidal neuron employed with that of other neurons could provide contrast information about the susceptibility of different cell types to excitation from electrical stimulation. As mentioned, the Betz cell would be an appropriate candidate for inclusion due to its potential increased susceptibility to excitation. Second, the NEURON simulation environment offers a high

degree of versatility for examining cellular dynamics, especially those arising from postsynaptic potentials. Further investigation is still necessary to test the I-wave hypothesis that corticocortical interactions between pyramidal cells and interneurons give rise to delayed volleys in the pyramidal tract. Postsynaptic potentials (and interneurons) could be included in our model to carry out investigation into this I-wave hypothesis. The current state of the model is limited to quantifying the susceptibility of pyramidal cells to excitation only, and little insight can be gained about the origin and behavior of I-waves. Interneurons that have postsynaptic inputs to pyramidal cells could be incorporated into the model to better understand the observed latencies of I-waves that follow motor cortex stimulation. A primary challenge of this endeavor would pertain to the placements and types of synaptic connections. How many synapses would be required? How many give rise to EPSPs? How many give rise to IPSPs? And, how would modulation be characterized in such a detailed model?

REFERENCES

Ahdab, R., Ayache, S. S., Brugières, P., Goujon, C., & Lefaucheur, J.-P. (2010). Comparison of “standard” and “navigated” procedures of TMS coil positioning over motor, premotor and prefrontal targets in patients with chronic pain and depression. *Clinical Neurophysiology*, *40*(1), 27–36. doi:10.1016/j.neucli.2010.01.001

Alliez, P., Rineau, L., Tayeb, S., Tournois, J., & Yvinec, M. (2000). 3D mesh generation. In *CGAL User and Reference Manual* (4.4 ed.). Board, CGAL Editorial.

Amatrudo, J. M., Weaver, C. M., Crimins, J. L., Hof, P. R., Rosene, D. L., & Luebke, J. I. (2012). Influence of highly distinctive structural properties on the excitability of pyramidal neurons in monkey visual and prefrontal cortices. *The Journal of Neuroscience*, *32*(40), 13644–60. doi:10.1523/JNEUROSCI.2581-12.2012

Arias-Carrión, O. (2008). Basic mechanisms of rTMS: Implications in Parkinson’s disease. *International Archives of Medicine*, *1*(1), 2. doi:10.1186/1755-7682-1-2

Awiszus, F., & Feistner, H. (1994). Quantification of D-and I-wave effects evoked by transcranial magnetic brain stimulation on the tibialis anterior motoneuron pool in man. *Experimental Brain Research*, *101*(1), 153–158.

Baker, S. N., Olivier, E., & Lemon, R. N. (1995). Task-related variation in corticospinal output evoked by transcranial magnetic stimulation in the macaque monkey. *The Journal of Physiology*, *488 (Pt 3*, 795–801.

Barker, A. T. (1999). The history and basic principles of magnetic nerve stimulation. *Electroencephalography and Clinical Neurophysiology*, *supp*(51), 3–21.

Barker, A. T., Jalinous, R., & Freeston, I. L. (1985). NON-INVASIVE MAGNETIC STIMULATION OF HUMAN MOTOR CORTEX. *The Lancet*, *325*(8437), 1106–1107. doi:10.1016/S0140-6736(85)92413-4

Basser, P. J. (1994). Focal magnetic stimulation of an axon. *IEEE Transactions on Bio-Medical Engineering*, *41*(6), 601–6. doi:10.1109/10.293248

Basser, P. J., & Roth, B. J. (1991). Stimulation of a myelinated nerve axon by electromagnetic induction. *Medical and Biological Engineering and Computing*, *29*(3), 261–268.

Bastos, Jp., & Nelson, S. (2003). *Electromagnetic Modeling by Finite Element Methods.* New York: Marcel Dekker, Inc.

Bickford, R., Guidi, M., & Fortesque, P. (1987). Magnetic stimulation of human peripheral nerve and brain: response enhancement by combined magnetoelectrical technique. *Neurosurgery*, *20*(1), 110–16.

Bohning, D. E., Pecheny, a P., Epstein, C. M., Speer, a M., Vincent, D. J., Dannels, W., & George, M. S. (1997). Mapping transcranial magnetic stimulation (TMS) fields in vivo with MRI. *Neuroreport*, *8*(11), 2535–8.

Bortolomasi, M., Minelli, A., Fuggetta, G., Perini, M., Comencini, S., Fiaschi, A., & Manganotti, P. (2007). Long-lasting effects of high frequency repetitive transcranial magnetic stimulation in major depressed patients. *Psychiatry Research*, *150*(2), 181–6. doi:10.1016/j.psychres.2006.04.010

Burke, D., Hicks, R., Gandevia, S., Stephen, J., Woodforth, I., & Crawford, M. (1993). Direct comparison of corticospinal volleys in human subjects to transcranial magnetic and electrical stimulation. *The Journal of Physiology*, 383–393.

Butson, C. R., Cooper, S. E., Henderson, J. M., & McIntyre, C. C. (2007). Patient-specific analysis of the volume of tissue activated during deep brain stimulation. *NeuroImage*, *34*(2), 661–70. doi:10.1016/j.neuroimage.2006.09.034

Butson, C. R., Cooper, S. E., Henderson, J. M., Wolgamuth, B., & McIntyre, C. C. (2011). Probabilistic Analysis of Activation Volumes Generated During Deep Brain Stimulation. *NeuroImage*, *54*, 2096–2104. doi:10.1016/j.neuroimage.2010.10.059

Butson, C. R., & McIntyre, C. C. (2005). Tissue and electrode capacitance reduce neural activation volumes during deep brain stimulation. *Clin Neurophysiol*, *116*(10), 2490–500. doi:10.1016/j.clinph.2005.06.023

Caparelli, E., Backus, W., Telang, F., Wang, G., Maloney, T., Goldstein, R., … Henn, F. (2010). Simultaneous TMS-fMRI of the Visual Cortex Reveals Functional Network, Even in Absence of Phosphene Sensation. *Open Neuroimaging Journal*, *4*(631), 100–110.

Carnevale, N., & Hines, M. L. (2006). *The NEURON Book*. Cambridge, UK: Cambridge University Press.

Chaturvedi, A., Butson, C. R., Lempka, S. F., Cooper, S. E., & McIntyre, C. C. (2010). Patient-specific models of deep brain stimulation: influence of field model complexity on neural activation predictions. *Brain Stimul*, *3*(2), 65–7. doi:10.1016/j.brs.2010.01.003

Cheeran, B., Koch, G., Stagg, C. J., Baig, F., & Teo, J. (2010). Transcranial magnetic stimulation: from neurophysiology to pharmacology, molecular biology and genomics. *The Neuroscientist : A Review Journal Bringing Neurobiology, Neurology and Psychiatry*, *16*(3), 210–21. doi:10.1177/1073858409349901

Chen, M., & Mogul, D. J. (2009). A structurally detailed finite element human head model for simulation of transcranial magnetic stimulation. *J Neurosci Methods*, *179*, 111–120. doi:10.1016/j.jneumeth.2009.01.010

Chronik, B., & Rutt, B. (2001). A Comparison Between Human Magnetostimulation Thresholds in Whole-Body and Head/Neck Gradient Coils. *Magnetic Resonance in Medicine*, *394*(February), 386–394.

Dale, A. M., Fischl, B., & Sereno, M. I. (1999). Cortical surface-based analysis: I. Segmentation and surface reconstruction. *Neuroimage*, *194*, 179–194.

Datta, A., Bansal, V., Diaz, J., Patel, J., Reato, D., & Bikson, M. (2009). Gyri-precise head model of transcranial DC stimulation: Improved spatial focality using a ring electrode versus conventional rectangular pad. *Brain Stimulation*, *2*(4), 201–207. doi:10.1016/j.brs.2009.03.005.Gyri

Davey, K. (2003). Modeling the effects of electrical conductivity of the head on the induced electric field in the brain during magnetic stimulation. *Clinical Neurophysiology*, *114*(11), 2204–2209. doi:10.1016/S1388-2457(03)00240-2

Davranche, K., Tandonnet, C., Burle, B., Meynier, C., Vidal, F., & Hasbroucq, T. (2007). The dual nature of time preparation: neural activation and suppression revealed by transcranial magnetic stimulation of the motor cortex. *The European Journal of Neuroscience*, *25*(12), 3766–74. doi:10.1111/j.1460-9568.2007.05588.x

Day, B. L., Dressler, D., Maertens de Noordhout, A., Marsden, C. D., Nakashima, K., Rothwell, J. C., & Thompson, P. D. (1989). Electric and magnetic stimulation of human motor cortex: surface EMG and single motor unit responses. *The Journal of Physiology*, *412*(1989), 449–73.

Day, B. L., Thompson, P. D., Dick, J. P., Nakashima, K., & Marsden, C. D. (1987). Different sites of action of electrical and magnetic stimulation of the human brain. *Neuroscience Letters*, *75*(1), 101–106. doi:10.1016/0304-3940(87)90083-8

De Lucia, M., Parker, G. J. M., Embleton, K., Newton, J. M., & Walsh, V. (2007). Diffusion tensor MRI-based estimation of the influence of brain tissue anisotropy on the effects of transcranial magnetic stimulation. *NeuroImage*, *36*(4), 1159–70. doi:10.1016/j.neuroimage.2007.03.062

Di Lazzaro, V., Capone, F., Apollonio, F., Borea, P. A., Cadossi, R., Fassina, L., … Ravazzani, P. (2013). A consensus panel review of central nervous system effects of the exposure to low-intensity extremely low-frequency magnetic fields. *Brain Stimulation*, *6*(4), 469–76. doi:10.1016/j.brs.2013.01.004

Di Lazzaro, V., Oliviero, A., Pilato, F., Saturno, E., Dileone, M., Mazzone, P., … Rothwell, J. C. (2004). The physiological basis of transcranial motor cortex stimulation in conscious humans. *Clinical Neurophysiology*, *115*(2), 255–266. doi:10.1016/j.clinph.2003.10.009

Di Lazzaro, V., Ziemann, U., & Lemon, R. N. (2008). State of the art: Physiology of transcranial motor cortex stimulation. *Brain Stimulation*, *1*(4), 345–62. doi:10.1016/j.brs.2008.07.004

Drew, T., Prentice, S., & Schepens, B. (2004). Cortical and brainstem control of locomotion. *Progress in Brain Research*, *143*, 251–261.

Dubach, P., Guggisberg, A. G., Rösler, K. M., Hess, C. W., & Mathis, J. (2004). Significance of coil orientation for motor evoked potentials from nasalis muscle

elicited by transcranial magnetic stimulation. *Clinical Neurophysiology*, *115*(4), 862–70. doi:10.1016/j.clinph.2003.11.033

Edgley, S., Eyre, J. a, Lemon, R. N., & Miller, S. (1997). Comparison of activation of corticospinal neurons and spinal motor neurons by magnetic and electrical transcranial stimulation in the lumbosacral cord of the anaesthetized monkey. *Brain*, *120 (Pt 5*, 839–53.

Edgley, S., Eyre, J., Lemon, R., & Miller, S. (1990). Excitation of the corticospinal tract by electromagnetic and electrical stimulation of the scalp in macaque monkey. *The Journal of Physiology*, (1990), 301–320.

Edwards, M. J., Talelli, P., & Rothwell, J. C. (2008). Clinical applications of transcranial magnetic stimulation in patients with movement disorders. *Lancet Neurology*, *7*(9), 827–40. doi:10.1016/S1474-4422(08)70190-X

Fox, P. T., Narayana, S., Tandon, N., Sandoval, H., Fox, S. P., Kochunov, P., & Lancaster, J. L. (2004). Column-based model of electric field excitation of cerebral cortex. *Human Brain Mapping*, *22*(1), 1–14. doi:10.1002/hbm.20006

Fregni, F., Simon, D. K., Wu, a, & Pascual-Leone, a. (2005). Non-invasive brain stimulation for Parkinson's disease: a systematic review and meta-analysis of the literature. *Journal of Neurology, Neurosurgery, and Psychiatry*, *76*(12), 1614–23. doi:10.1136/jnnp.2005.069849

Fuglevand, a J., Winter, D. a, & Patla, a E. (1993). Models of recruitment and rate coding organization in motor-unit pools. *Journal of Neurophysiology*, *70*(6), 2470–88.

George, M. S., Lisanby, S. H., & Sackeim, H. a. (1999). Transcranial magnetic stimulation: applications in neuropsychiatry. *Archives of General Psychiatry*, *56*(4), 300–11.

Graessner, J. (2011, January). Frequently Asked Questions : Diffusion-Weighted Imaging (DWI). *MAGNETOM Flash*, 84–87.

Grefkes, C., & Fink, G. R. (2011). Reorganization of cerebral networks after stroke: new insights from neuroimaging with connectivity approaches. *Brain*. doi:10.1093/brain/awr033

Grefkes, C., Nowak, D. a, Wang, L. E., Dafotakis, M., Eickhoff, S. B., & Fink, G. R. (2010). Modulating cortical connectivity in stroke patients by rTMS assessed with fMRI and dynamic causal modeling. *NeuroImage*, *50*(1), 233–42. doi:10.1016/j.neuroimage.2009.12.029

Güllmar, D., Haueisen, J., & Reichenbach, J. R. (2010). Influence of anisotropic electrical conductivity in white matter tissue on the EEG/MEG forward and inverse solution. A high-resolution whole head simulation study. *NeuroImage*, *51*(1), 145–63. doi:10.1016/j.neuroimage.2010.02.014

Hallett, M. (2000). Transcranial magnetic stimulation and the human brain. *Nature*, *406*(6792), 147–50. doi:10.1038/35018000

Hallett, M. (2007). Transcranial magnetic stimulation: a primer. *Neuron*, *55*(2), 187–99. doi:10.1016/j.neuron.2007.06.026

Hanajima, R., Ugawa, Y., Terao, Y., Enomoto, H., Shiio, Y., Mochizuki, H., … Kanazawa, I. (2002). Mechanisms of intracortical I-wave facilitation elicited with paired-pulse magnetic stimulation in humans. *Journal of Physiology*, *538*(1), 253–261. doi:10.1013/jphysiol.2001.013094

Hemmings, H. C., Yan, W., Westphalen, R. I., & Ryan, T. A. (2005). The General Anesthetic Isoflurane Depresses Synaptic Vesicle Exocytosis, *67*(5), 1591–1599. doi:10.1124/mol.104.003210.ceptors

Herbsman, T., Forster, L., Molnar, C., Dougherty, R., Christie, D., Koola, J., … Nahas, Z. (2009). Motor threshold in transcranial magnetic stimulation: the impact of white matter fiber orientation and skull-to-cortex distance. *Human Brain Mapping*, *30*(7), 2044–55. doi:10.1002/hbm.20649

Hern, J., & Landgren, S. (1962). Selective excitation of corticofugal neurones by surface-anodal stimulation of the baboon's motor cortex. *J. Physiol.*, 73–90.

Hernandez-Garcia, L., Hall, T., Gomez, L., & Michielssen, E. (2010). A numerically optimized active shield for improved transcranial magnetic stimulation targeting. *Brain Stimulation*, *3*(4), 218–25. doi:10.1016/j.brs.2010.05.001

Hodgkin, A. L., & Huxley, A. F. (1952). A quantitative description of membrane current and its application to conduction and excitation in nerve. *The Journal of Physiology*, *117*(4), 500.

Holsheimer, J., Dijkstra, E. a, Demeulemeester, H., & Nuttin, B. (2000). Chronaxie calculated from current-duration and voltage-duration data. *Journal of Neuroscience Methods*, *97*(1), 45–50.

Hoogendam, J. M., Ramakers, G. M. J., & Di Lazzaro, V. (2010). Physiology of repetitive transcranial magnetic stimulation of the human brain. *Brain Stimulation*, *3*(2), 95–118. doi:10.1016/j.brs.2009.10.005

Houdayer, E., Degardin, A., Cassim, F., Bocquillon, P., Derambure, P., & Devanne, H. (2008). The effects of low- and high-frequency repetitive TMS on the input/output properties of the human corticospinal pathway. *Experimental Brain Research*, *187*(2), 207–17. doi:10.1007/s00221-008-1294-z

Jalinous, R. (1998). *Guide to Magnetic Stimulation*.

Jenkinson, M., Beckmann, C. F., Behrens, T. E. J., Woolrich, M. W., & Smith, S. M. (2012). Fsl. *NeuroImage*, *62*(2), 782–90. doi:10.1016/j.neuroimage.2011.09.015

Julkunen, P., Säisänen, L., Danner, N., Niskanen, E., Hukkanen, T., Mervaala, E., & Könönen, M. (2009). Comparison of navigated and non-navigated transcranial magnetic stimulation for motor cortex mapping, motor threshold and motor evoked potentials. *NeuroImage*, *44*(3), 790–5. doi:10.1016/j.neuroimage.2008.09.040

Jung, N. H., Delvendahl, I., Kuhnke, N. G., Hauschke, D., Stolle, S., & Mall, V. (2010). Navigated transcranial magnetic stimulation does not decrease the variability of motor-evoked potentials. *Brain Stimulation*, *3*(2), 87–94. doi:10.1016/j.brs.2009.10.003

Kammer, T., Beck, S., Thielscher, A., Laubis-Herrmann, U., & Topka, H. (2001). Motor thresholds in humans: a transcranial magnetic stimulation study comparing different pulse waveforms, current directions and stimulator types. *Clinical Neurophysiology*, *112*(2), 250–8.

Kammer, T., Vorwerg, M., & Herrnberger, B. (2007). Anisotropy in the visual cortex investigated by neuronavigated transcranial magnetic stimulation. *NeuroImage*, *36*(2), 313–21. doi:10.1016/j.neuroimage.2007.03.001

Kleinjung, T., Eichhammer, P., Langguth, B., Jacob, P., Marienhagen, J., Hajak, G., … Strutz, J. (2005). Long-term effects of repetitive transcranial magnetic stimulation (rTMS) in patients with chronic tinnitus. *Otolaryngology--Head and Neck Surgery*, *132*(4), 566–9. doi:10.1016/j.otohns.2004.09.134

Kowalski, T., Silny, J., & Buchner, H. (2002). Current density threshold for the stimulation of neurons in the motor cortex area. *Bioelectromagnetics*, *23*(6), 421–8. doi:10.1002/bem.10036

Krames, E. S., Peckham, P. H., & Rezai, A. R. (Eds.). (2009). *Neuromodulation* (1st ed.). London: Elsevier Ltd.

Krieg, T. D., Salinas, F. S., Narayana, S., Fox, P. T., & Mogul, D. J. (2013). PET-Based Confirmation of Orientation Sensitivity of TMS-Induced Cortical Activation in Humans. *Brain Stimulation*, 1–7. doi:10.1016/j.brs.2013.05.007

Laakso, I., Hirata, A., & Ugawa, Y. (2014). Effects of coil orientation on the electric field induced by TMS over the hand motor area. *Physics in Medicine and Biology*, *59*(1), 203–18. doi:10.1088/0031-9155/59/1/203

Langguth, B., de Ridder, D., Dornhoffer, J. L., Eichhammer, P., Folmer, R. L., Frank, E., … Kleinjung, T. (2008). Controversy: Does repetitive transcranial magnetic stimulation/ transcranial direct current stimulation show efficacy in treating tinnitus patients? *Brain Stimulation*, *1*(3), 192–205. doi:10.1016/j.brs.2008.06.003

Maier, M. a, Armand, J., Kirkwood, P. a, Yang, H.-W., Davis, J. N., & Lemon, R. N. (2002). Differences in the corticospinal projection from primary motor cortex and supplementary motor area to macaque upper limb motoneurons: an anatomical and electrophysiological study. *Cerebral Cortex (New York, N.Y. : 1991)*, *12*(3), 281–96.

Mainen, Z. F., Joerges, J., Huguenard, J. R., & Sejnowski, T. J. (1995). A model of spike initiation in neocortical pyramidal neurons. *Neuron*, *15*(6), 1427–39.

Maks, C. B., Butson, C. R., Walter, B. L., Vitek, J. L., & McIntyre, C. C. (2009). Deep brain stimulation activation volumes and their association with neurophysiological mapping and therapeutic outcomes. *Journal of Neurology, Neurosurgery, and Psychiatry*, *80*(6), 659–66. doi:10.1136/jnnp.2007.126219

Malmivuo, J. a, & Plonsey, R. (1995). *Bioelectromagnetism - Principles and Applications of Bioelectric and Biomagnetic Fields*. New York: Oxford University Press.

McIntyre, C. C., Grill, W. M., Sherman, D. L., & Thakor, N. V. (2004). Cellular effects of deep brain stimulation: model-based analysis of activation and inhibition. *Journal of Neurophysiology*, *91*(4), 1457–69. doi:10.1152/jn.00989.2003

McRobbie, D., & Foster, M. a. (1984). Thresholds for biological effects of time-varying magnetic fields. *Clinical Physics and Physiological Measurement*, *5*(2), 67–78.

Merton, P. A., & Morton, H. B. (1980). Stimulation of the cerebral cortex in the intact human subject. *Nature*, *285*(5762), 227.

Miranda, P. C., Hallett, M., & Basser, P. J. (2003). The electric field induced in the brain by magnetic stimulation: a 3-D finite-element analysis of the effect of tissue heterogeneity and anisotropy. *IEEE Transactions on Bio-Medical Engineering*, *50*(9), 1074–85. doi:10.1109/TBME.2003.816079

Moisa, M., Pohmann, R., Ewald, L., & Thielscher, A. (2009). New coil positioning method for interleaved transcranial magnetic stimulation (TMS)/functional MRI (fMRI) and its validation in a motor cortex study. *Journal of Magnetic Resonance Imaging : JMRI*, *29*(1), 189–97. doi:10.1002/jmri.21611

Nagarajan, S. S., Durand, D. M., & Warman, E. N. (1993). Effects of induced electric fields on finite neuronal structures: a simulation study. *IEEE Transactions on Bio-Medical Engineering*, *40*(11), 1175–88. doi:10.1109/10.245636

Nakamura, H., Kitagawa, H., Kawaguchi, Y., & Tsuji, H. (1996). Direct and indirect activation of human corticospinal neurons by. *Neuroscience Letters*, *210*, 45–48.

Nitsche, M. a, & Paulus, W. (2009). Noninvasive brain stimulation protocols in the treatment of epilepsy: current state and perspectives. *Neurotherapeutics*, *6*(2), 244–50. doi:10.1016/j.nurt.2009.01.003

O'Reardon, J. P., Solvason, H. B., Janicak, P. G., Sampson, S., Isenberg, K. E., Nahas, Z., … Sackeim, H. a. (2007). Efficacy and safety of transcranial magnetic stimulation in the acute treatment of major depression: a multisite randomized controlled trial. *Biological Psychiatry*, *62*(11), 1208–16. doi:10.1016/j.biopsych.2007.01.018

Opitz, A., Legon, W., Rowlands, A., Bickel, W. K., Paulus, W., & Tyler, W. J. (2013). Physiological observations validate finite element models for estimating subject-specific electric field distributions induced by transcranial magnetic stimulation of the human motor cortex. *NeuroImage*, *81*, 253–64. doi:10.1016/j.neuroimage.2013.04.067

Opitz, A., Windhoff, M., Heidemann, R. M., Turner, R., & Thielscher, A. (2011). How the brain tissue shapes the electric field induced by transcranial magnetic stimulation. *NeuroImage*, *58*(3), 849–859. doi:10.1016/j.neuroimage.2011.06.069

Pascual-Leone, a, Valls-Solé, J., Wassermann, E. M., & Hallett, M. (1994). Responses to rapid-rate transcranial magnetic stimulation of the human motor cortex. *Brain*, *117 (Pt 4*, 847–58.

Pashut, T., Wolfus, S., Friedman, A., Lavidor, M., Bar-Gad, I., Yeshurun, Y., & Korngreen, A. (2011). Mechanisms of magnetic stimulation of central nervous system neurons. *PLoS Computational Biology*, *7*(3), e1002022. doi:10.1371/journal.pcbi.1002022

Recoskie, B. J., Scholl, T. J., & Chronik, B. a. (2009). The discrepancy between human peripheral nerve chronaxie times as measured using magnetic and electric field stimuli: the relevance to MRI gradient coil safety. *Physics in Medicine and Biology*, *54*(19), 5965–79. doi:10.1088/0031-9155/54/19/020

Reis, J., Swayne, O. B., Vandermeeren, Y., Camus, M., Dimyan, M. a, Harris-Love, M., … Cohen, L. G. (2008). Contribution of transcranial magnetic stimulation to the understanding of cortical mechanisms involved in motor control. *The Journal of Physiology*, *586*(2), 325–51. doi:10.1113/jphysiol.2007.144824

Ridding, M. C., & Rothwell, J. C. (2007). Is there a future for therapeutic use of transcranial magnetic stimulation? *Nature Reviews. Neuroscience*, *8*(7), 559–67. doi:10.1038/nrn2169

Riva-Posse, P., Sueng Choi, K., Holtzheimer, P. E., McIntyre, C. C., Gross, R. E., Chaturvedi, A., … Mayberg, H. S. (2014). Defining Critical White Matter Pathways Mediating Successful Subcallosal Cingulate Deep Brain Stimulation for Treatment-Resistant Depression. *Biological Psychiatry*, 1–7. doi:10.1016/j.biopsych.2014.03.029

Rossi, S., Hallett, M., Rossini, P. M., & Pascual-Leone, A. (2009). Safety, ethical considerations, and application guidelines for the use of transcranial magnetic stimulation in clinical practice and research. *Clinical Neurophysiology*, *120*(12), 2008–39. doi:10.1016/j.clinph.2009.08.016

Rossini, P. M., & Rossi, S. (2007). Transcranial magnetic stimulation: diagnostic, therapeutic, and research potential. *Neurology*, *68*(7), 484–8. doi:10.1212/01.wnl.0000250268.13789.b2

Rotem, A., Neef, A., Neef, N. E., Agudelo-Toro, A., Rakhmilevitch, D., Paulus, W., & Moses, E. (2014). Solving the orientation specific constraints in transcranial

magnetic stimulation by rotating fields. *PloS One*, *9*(2), e86794. doi:10.1371/journal.pone.0086794

Roth, B. J., & Basser, P. J. (1990). A model of the stimulation of a nerve fiber by electromagnetic induction. *Biomedical Engineering, IEEE Transactions on*, *37*(6), 588–597.

Roth, Y., Amir, A., Levkovitz, Y., & Zangen, A. (2007). Three-dimensional distribution of the electric field induced in the brain by transcranial magnetic stimulation using figure-8 and deep H-coils. *Journal of Clinical Neurophysiology*, *24*(1), 31–8. doi:10.1097/WNP.0b013e31802fa393

Roth, Y., Pell, G. S., Chistyakov, A. V, Sinai, A., Zangen, A., & Zaaroor, M. (2014). Motor cortex activation by H-coil and figure-8 coil at different depths. Combined motor threshold and electric field distribution study. *Clinical Neurophysiology*, *125*(2), 336–43. doi:10.1016/j.clinph.2013.07.013

Roth, Y., & Zangen, A. (2014). Deep TMS: Method and clinical results. *Magnet*.

Rullmann, M., Anwander, a, Dannhauer, M., Warfield, S. K., Duffy, F. H., & Wolters, C. H. (2009). EEG source analysis of epileptiform activity using a 1 mm anisotropic hexahedra finite element head model. *NeuroImage*, *44*(2), 399–410. doi:10.1016/j.neuroimage.2008.09.009

Ruohonen, J., & Ilmoniemi, R. J. (1999). Modelling of the stimulating field generation in TMS. *Electroencephalography and Clinical Neurophysiology*, *supp.*(51), 30–40.

Ruohonen, J., & Karhu, J. (2010). Navigated transcranial magnetic stimulation. *Clinical Neurophysiology*, *40*(1), 7–17. doi:10.1016/j.neucli.2010.01.006

Säisänen, L., Könönen, M., Julkunen, P., Määttä, S., Vanninen, R., Immonen, A., … Mervaala, E. (2010). Non-invasive preoperative localization of primary motor cortex in epilepsy surgery by navigated transcranial magnetic stimulation. *Epilepsy Research*, *92*(2-3), 134–44. doi:10.1016/j.eplepsyres.2010.08.013

Sakai, K., Ugawa, Y., Terao, Y., Hanajima, R., Furubayashi, T., & Kanazawa, I. (1997). Preferential activation of different I waves by transcranial magnetic stimulation with a figure-of-eight-shaped coil. *Experimental Brain Research*, *113*(1), 24–32.

Salinas, F. S., Lancaster, J. L., & Fox, P. T. (2007). Detailed 3D models of the induced electric field of transcranial magnetic stimulation coils. *Physics in Medicine and Biology*, *52*(10), 2879–92. doi:10.1088/0031-9155/52/10/016

Salinas, F. S., Lancaster, J. L., & Fox, P. T. (2009). 3D modeling of the total electric field induced by transcranial magnetic stimulation using the boundary element method. *Physics in Medicine and Biology*, *54*(12), 3631–47. doi:10.1088/0031-9155/54/12/002

Salinas, F. S., Szabó, C. Á., Zhang, W., Jones, L., Leland, M. M., Wey, H.-Y., … Narayana, S. (2011). Functional neuroimaging of the baboon during concurrent image-guided transcranial magnetic stimulation. *NeuroImage*, *57*(4), 1393–1401. doi:10.1016/j.neuroimage.2011.05.065

Sampson, S. M., Rome, J. D., & Rummans, T. a. (2006). Slow-frequency rTMS reduces fibromyalgia pain. *Pain Medicine (Malden, Mass.)*, *7*(2), 115–8. doi:10.1111/j.1526-4637.2006.00106.x

Siebner, H. R., Bergmann, T. O., Bestmann, S., Massimini, M., Johansen-Berg, H., Mochizuki, H., … Rossini, P. M. (2009). Consensus paper: combining transcranial stimulation with neuroimaging. *Brain Stimulation*, *2*(2), 58–80. doi:10.1016/j.brs.2008.11.002

Silbert, B. I., Gibbons, J. T., Cash, R. H. F., Mastaglia, F. L., & Thickbroom, G. W. (2010). Modulation of corticomotor excitability by an I-wave intervention delivered during low-level voluntary contraction. *Experimental Brain Research*. doi:10.1007/s00221-010-2473-2

Silva, S., Basser, P. J., & Miranda, P. C. (2008). Elucidating the mechanisms and loci of neuronal excitation by transcranial magnetic stimulation using a finite element model of a cortical sulcus. *Clinical Neurophysiology*, *119*(10), 2405–13. doi:10.1016/j.clinph.2008.07.248

Stillings, D. (1971). The first use of electricity for pain treatment. *Medronic Archive of ElectroStimulation*.

Stinear, C. M., Barber, P. A., Coxon, J. P., Verryt, T. S., Acharya, P. P., & Byblow, W. D. (2009). Repetitive stimulation of premotor cortex affects primary motor cortex excitability and movement preparation. *Brain Stimulation*, *2*(3), 152–62. doi:10.1016/j.brs.2009.01.001

Tadel, F., Baillet, S., Mosher, J. C., Pantazis, D., & Leahy, R. M. (2011). Brainstorm: a user-friendly application for MEG/EEG analysis. *Computational Intelligence and Neuroscience*, *2011*, 879716. doi:10.1155/2011/879716

Terao, Y., & Ugawa, Y. (2002). Basic mechanisms of TMS. *Journal of Clinical Neurophysiology*, *19*(4), 322–43.

Thickbroom, G. W., Byrnes, M. L., Edwards, D. J., & Mastaglia, F. L. (2006). Repetitive paired-pulse TMS at I-wave periodicity markedly increases corticospinal excitability: a new technique for modulating synaptic plasticity. *Clinical Neurophysiology : Official Journal of the International Federation of Clinical Neurophysiology*, *117*(1), 61–6. doi:10.1016/j.clinph.2005.09.010

Thielscher, A., Opitz, A., & Windhoff, M. (2011). Impact of the gyral geometry on the electric field induced by transcranial magnetic stimulation. *NeuroImage*, *54*(1), 234–43. doi:10.1016/j.neuroimage.2010.07.061

Thielscher, A., & Wichmann, F. a. (2009). Determining the cortical target of transcranial magnetic stimulation. *NeuroImage*, *47*(4), 1319–30. doi:10.1016/j.neuroimage.2009.04.021

Tofts, P. S. (1990). The distribution of induced currents in magnetic stimulation of the nervous system. *Physics in Medicine and Biology*, *35*(8), 1119–28.

Trebbastoni, A., Raccah, R., de Lena, C., Zangen, A., & Inghilleri, M. (2013). Repetitive Deep Transcranial Magnetic Stimulation Improves Verbal Fluency and Written Language in a Patient with Primary Progressive Aphasia-Logopenic Variant (LPPA). *Brain Stimulation*, *6*(4), 545–53. doi:10.1016/j.brs.2012.09.014

Tuch, D. S., Wedeen, V. J., Dale, a M., George, J. S., & Belliveau, J. W. (1999). Conductivity mapping of biological tissue using diffusion MRI. *Annals of the New York Academy of Sciences*, *888*, 314–6.

Tuch, D. S., Wedeen, V. J., Dale, a M., George, J. S., & Belliveau, J. W. (2001). Conductivity tensor mapping of the human brain using diffusion tensor MRI. *Proceedings of the National Academy of Sciences of the United States of America*, *98*(20), 11697–701. doi:10.1073/pnas.171473898

Vaalto, S., Säisänen, L., Könönen, M., Julkunen, P., Hukkanen, T., Määttä, S., & Karhu, J. (2010). Corticospinal output and cortical excitation-inhibition balance in distal hand muscle representations in nonprimary motor area. *Human Brain Mapping*, *000*(July). doi:10.1002/hbm.21137

Wagner, T., Fregni, F., Eden, U., Ramos-Estebanez, C., Grodzinsky, A. J., Zahn, M., & Pascual-Leone, A. (2006). Transcranial magnetic stimulation and stroke: a computer-based human model study. *NeuroImage*, *30*(3), 857–70. doi:10.1016/j.neuroimage.2005.04.046

Wagner, T., Valero-Cabre, A., & Pascual-Leone, A. (2007). Noninvasive human brain stimulation. *Annual Review of Biomedical Engineering*, *9*, 527–65. doi:10.1146/annurev.bioeng.9.061206.133100

Wagner, T., Zahn, M., Grodzinsky, A. J., & Pascual-leone, A. (2004). Three-Dimensional Head Model Simulation of Transcranial Magnetic Stimulation, *51*(9), 1586–1598.

Walsh, V., & Pascual-Leone, A. (2005). *Transcranial Magnetic Stimulation: A Neurochronometrics of Mind*. MIT Press.

Warman, E. N., Grill, W. M., & Durand, D. (1992). Modeling the effects of electric fields on nerve fibers: determination of excitation thresholds. *IEEE Transactions on Bio-Medical Engineering*, *39*(12), 1244–54.

Werhahn, K., Fong, J., Meyer, B.-U., Priori, A., Rothwell, J. C., Day, B. L., & Thompson, P. D. (1994). The effect of magnetic coil orientation on the latency of surface EMG and single motor unit responses in the first dorsal interosseous muscle. *Electroencephalography and Clinical Neurophysiology*, *93*(2), 138–146.

Westin, C.-F., Maier, S. E., Mamata, H., Nabavi, a, Jolesz, F. a, & Kikinis, R. (2002). Processing and visualization for diffusion tensor MRI. *Medical Image Analysis*, *6*(2), 93–108.

Williams, J. a, Imamura, M., & Fregni, F. (2009). Updates on the use of non-invasive brain stimulation in physical and rehabilitation medicine. *Journal of Rehabilitation Medicine*, *41*(5), 305–11. doi:10.2340/16501977-0356

Wyckhuys, T., De Geeter, N., Crevecoeur, G., Stroobants, S., & Staelens, S. (2013). Quantifying the Effect of Repetitive Transcranial Magnetic Stimulation in the Rat Brain by μSPECT CBF Scans. *Brain Stimulation*, *6*(4), 554–62. doi:10.1016/j.brs.2012.10.004

Yao, W., Fuglevand, R. J., & Enoka, R. M. (2000). Motor-Unit Synchronization Increases EMG Amplitude and Decreases Force Steadiness of Simulated Contractions. *Journal of Neurophysiology*, *83*, 441–452.

Yousry, T. a, Schmid, U. D., Alkadhi, H., Schmidt, D., Peraud, A., Buettner, A., & Winkler, P. (1997). Localization of the motor hand area to a knob on the precentral gyrus. A new landmark. *Brain*, *120 (Pt 1*, 141–57.

Appendix A

The following are Maxwell's equations and general field equations for application the Fourier (frequency) domain. The following equations were implemented for electromagnetic field calculations by the TMS figure-8 coil model and subject-specific FEM.

The magnetic vector potential ($\mathbf{A}$) is related to the current dipole ($\mathbf{Q}$) by

$$\mathbf{A} = \frac{\mu_0 \mathbf{Q}}{4\pi R} \qquad \text{(Eq. A.1)}$$

where μ_0 is the magnetic permeability of free space, and R is the distance from $\mathbf{Q}$ to any point in space. The magnetic field ($\mathbf{B}$) is related by the A-field by

$$\mathbf{B} = \nabla \times \mathbf{A} \qquad \text{(Eq. A.2)}$$

The magnetically induced E-field is described by

$$\mathbf{E} = -\nabla \Phi - \frac{d\mathbf{A}}{dt} \qquad \text{(Eq. A.3)}$$

where the scalar potential, Φ, results from charge distribution due to model boundaries and dielectric effects. The E-field is related to the B-field by

$$\nabla \times \mathbf{E} = -\frac{\partial \mathbf{B}}{\partial t} \qquad \text{(Eq. A.4)}$$

The electric displacement ($\mathbf{D}$) field follows Gauss' law

$$\nabla \cdot \mathbf{D} = \rho \qquad \text{(Eq. A.5)}$$

where ρ is the charge density. It follows that the B-field be conserved.

$$\nabla \cdot \mathbf{B} = 0 \qquad \text{(Eq. A.6)}$$

The equation of continuity for current density ($\mathbf{J}$):

$$\nabla \cdot \mathbf{J} = -\frac{\partial \rho}{\partial t} \quad \text{(Eq. A.7)}$$

The current density follows

$$\mathbf{J} = \sigma \mathbf{E} \quad \text{(Eq. A.8)}$$

where σ is the electric conductivity. FEM software (COMSOL) employed in this study solves the time-harmonic (Fourier domain) equation

$$(j\omega\sigma - \omega^2\epsilon)\mathbf{A} + \nabla\times(\mu^{-1}\nabla\times\mathbf{A}) = \mathbf{J}_e = 0 \quad \text{(Eq. A.9)}$$

where ω is the frequency, ϵ is the permittivity, and $\mathbf{J}_e$ is the external current density. From $\mathbf{A}$, the E-field and electric potential can be obtained from Eq. A.3. For TMS applications,

$$\nabla \cdot \mathbf{J} = 0 \quad \text{(Eq. A.10)}$$

Appendix B

The following is a derivation of the strength-duration curve for magnetic stimulation. This approach is a well established one, and it is used especially in magnetic stimulation of tissue by eddy currents from the switching on and off of gradient coils in MRI (Hemmings et al., 2005). This derivation has been modified specifically for stimulation from TMS rather from MRI gradient coils, which produce highly uniform B-fields relative to TMS. The mean E-field magnitude during supra-threshold stimulation is defined as

$$\overline{|\mathbf{E}|}_s \equiv \frac{1}{\tau}\int_0^{\tau} |\mathbf{E}(t)|\, dt \geq |\mathbf{E}|_{rh}\left(1+\frac{\tau_c}{\tau}\right) \quad \text{(Eq. A.11)}$$

where $|\mathbf{E}(t)|$ is the magnitude of the E-field in time throughout the duration of the stimulus τ, $|\mathbf{E}|_{rh}$ is the minimum E-field magnitude to cause activation at constant . As previously shown, the E-field at any point in space having a distance r from the coil is a function of the coil current.

$$\mathbf{E} = -\frac{d\mathbf{A}(r)}{dt} \propto -\frac{dI_{coil}}{dt} \quad \text{(Eq. A.12)}$$

where $\mathbf{A}(r)$ is a function of position and represents the contributions of the A-field and scalar potential ($\nabla\Phi$) to the E-field the magnetic vector potential. Inserting Eq. A.12 into Eq. A.11 yields

$$\int_0^{\tau} \frac{dI_{coil}}{dt}\, dt \geq \left(\frac{dI_{coil}}{dt}\right)\tau + \left(\frac{dI_{coil}}{dt}\right)\tau_c \quad \text{(Eq. A.13)}$$

$$\Delta I_s \geq \left(\frac{dI_{coil}}{dt}\right)_{min}\tau + \Delta I_{min} \quad \text{(Eq. A.14)}$$

where the coil current rise ΔI_s is required cause stimulation over a time τ. Here, ΔI_{min} is the minimum current step at the upper limit of dI_{coil}/dt required to cause stimulation. The

bracketed term in Eq. A.14 is the minimum rate of change of the coil current at the upper limit of I_{coil} required to cause stimulation. The chronaxie can be determined directly from the minimum threshold parameters (Drew et al., 2004).

$$\tau_c = {\Delta I_{min}}\Big/{\frac{dI_{coil}}{dt}} \qquad \text{(Eq. A.15)}$$

Appendix C

The model construction flow diagram is shown on the following two pages. This flow diagram is presented to provide an illustration of the general flow of data to arrive at a subject-specific multiscale model. Furthermore, this diagram illustrates that our model is a product of the work of many other scientists who developed software enabling the construction of this model.

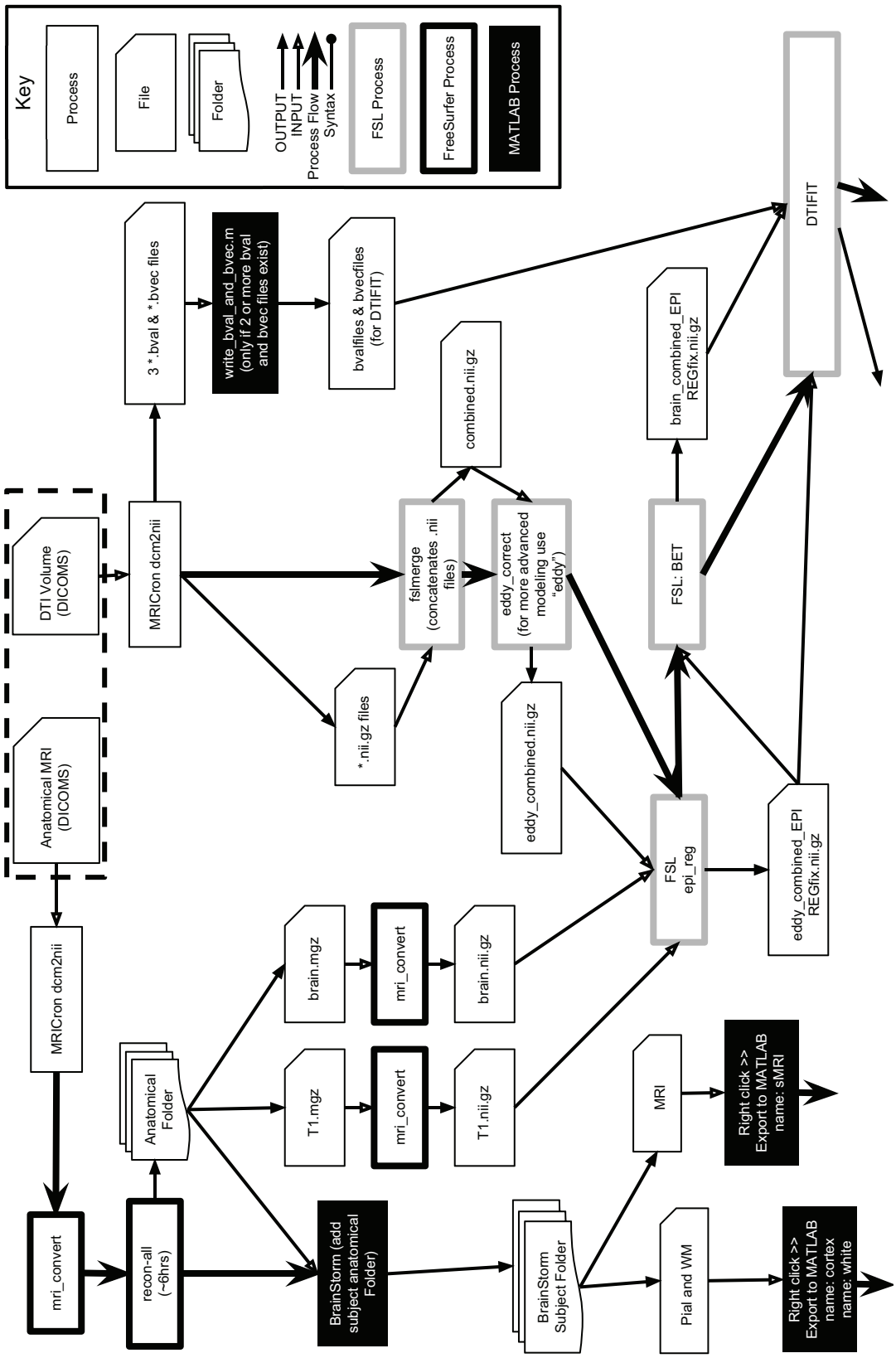
Key
Process
File
Folder
OUTPUT
INPUT
Process Flow
Syntax
FSL Process
FreeSurfer Process
MATLAB Process
DTI Volume (DICOMS)
Anatomical MRI (DICOMS)
MRICron dcm2nii
3 *.bval & *.bvec files
write_bval_and_bvec.m (only if 2 or more bval and bvec files exist)
bvalfiles & bvecfiles (for DTIFIT)
DTIFIT
combined.nii.gz
brain_combined_EPI REGfix.nii.gz
fslmerge (concatenates .nii files)
eddy_correct (for more advanced modeling use "eddy")
FSL: BET
*.nii.gz files
eddy_combined.nii.gz
FSL epi_reg
eddy_combined_EPI REGfix.nii.gz
brain.mgz
mri_convert
brain.nii.gz
T1.mgz
mri_convert
T1.nii.gz
Anatomical Folder
MRI
Right click >> Export to MATLAB name: sMRI
mri_convert
recon-all (~6hrs)
BrainStorm (add subject anatomical Folder)
BrainStorm Subject Folder
Pial and WM
Right click >> Export to MATLAB name: cortex name: white

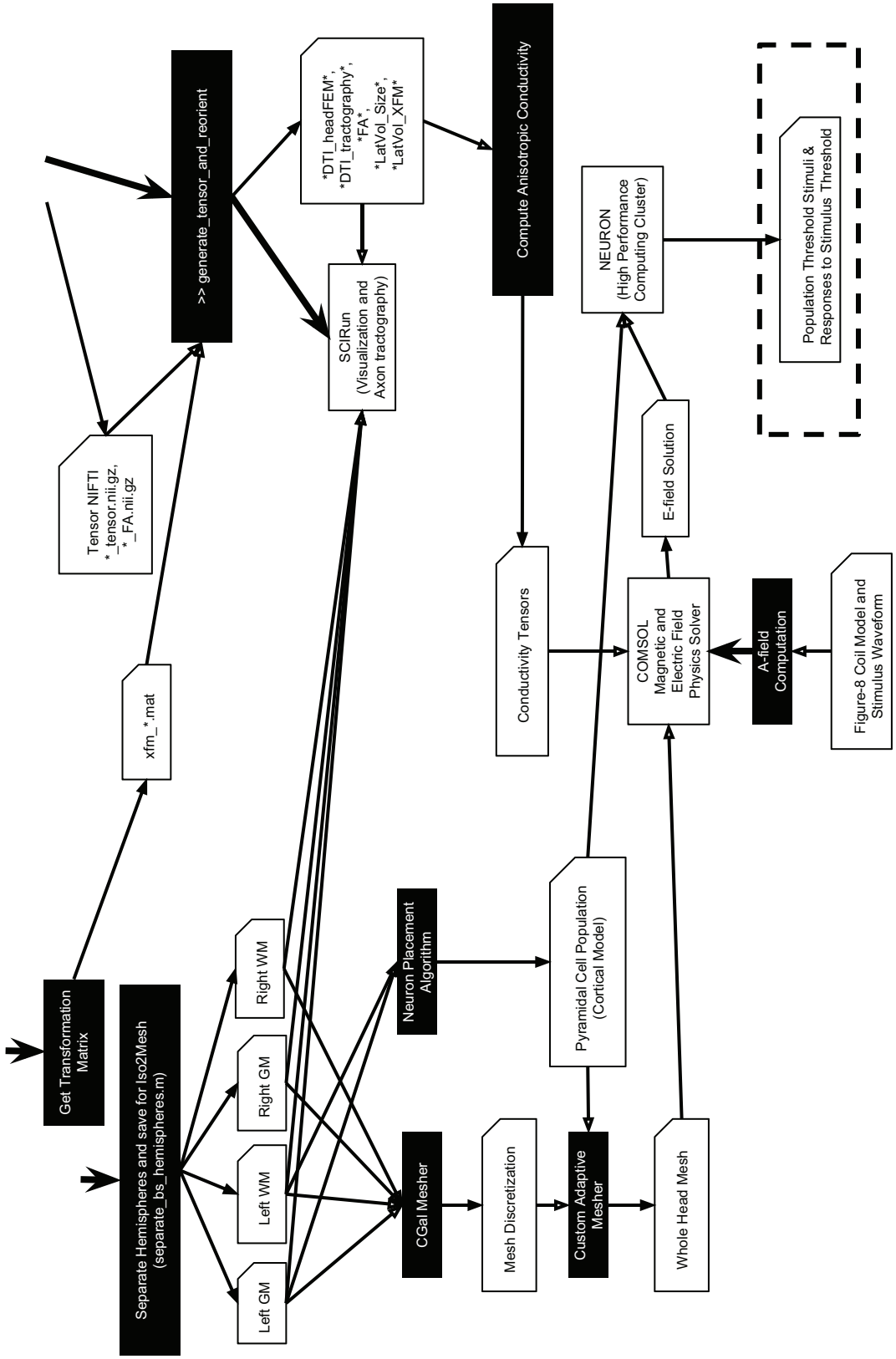
Get Transformation Matrix
Separate Hemispheres and save for Iso2Mesh (separate_bs_hemispheres.m)
Left GM
Left WM
Right GM
Right WM
xfm_*.mat
Tensor NIFTI *_tensor.nii.gz, *_FA.nii.gz
>> generate_tensor_and_reorient
DTI_headFEM, *DTI_tractography*, *FA*, *LatVol_Size*, *LatVol_XFM*
SCIRun (Visualization and Axon tractography)
Compute Anisotropic Conductivity
NEURON (High Performance Computing Cluster)
Population Threshold Stimuli & Responses to Stimulus Threshold
E-field Solution
Conductivity Tensors
COMSOL Magnetic and Electric Field Physics Solver
A-field Computation
Figure-8 Coil Model and Stimulus Waveform
Neuron Placement Algorithm
Pyramidal Cell Population (Cortical Model)
CGal Mesher
Mesh Discretization
Custom Adaptive Mesher
Whole Head Mesh

Appendix D

The following medical image protocol is chronologically enumerated. Full image acquisition time was approximately 30 minutes.

1. Scan #1: 3 plane localizer scan; scan time 45 sec; FOV: 24; slice thickness: 10 mm; 5 mm spacing, matrix 256-by-128, 1NEX, no. slices: 13.
2. Scan #2: Spoiled Gradient (SpGr); scan time 8 min 10 sec; TE-min full TR -9.7, prep time 450 ms, Flip angle 12, FOV: 22, slice thickness: 1.0, no. slices: 180, matrix: 256-by-224, phase FOV: 0.80, frequency direction: AP.
3. Scan #3: High order shim; calibration scan; no images saved.
4. Scan #4: EPI; scan time: 8 min. TE: 25, TR: 2 sec; Flip angle: 77; FOV 22, thickness: 4mm, 32 slices, no. of excitations: 1; reps: 240, matrix 64-by-64, frequency direction: right-to-left.
5. Scan #5: DTI; scan time: approx. 8mins; run once; TE: min, TR: min; FOV: 256 mm; slice thickness: 2.0; in plane resolution: 2 mm; align slices AC-PC, collect as many to cover whole brain, matrix 128-by-128, no. of excitations: 1; b-value: 900; diffusion tensor; no. of diffusion directions: 60; disable twice refocusing.

Subject: Fw: Permission Request
Date: Thursday, November 13, 2014 at 3:07:16 AM Central Standard Time
From: Permissions (sent by Gemma Alaway <Gemma.Alaway@iop.org>)
To: Goodwin, Brian
CC: Lex, Sherri, butson@sci.utah.edu

Dear Dr Goodwin,
Thank you for your request to reproduce IOP Publishing material
We are happy to grant permission for the use you request of figure 5 of Phys Med Biol. 2007;52(10):2879---92. doi:10.1088/0031--- 9155/52/10/016. on the terms set out below.

Conditions
Non-exclusive, non-transferrable, revocable, worldwide, permission to use the material in print and electronic form will be granted subject to the following conditions:
· Permission will be cancelled without notice if you fail to fulfil any of the conditions of this letter.
· You will make reasonable efforts to contact the author(s) to seek consent for your intended use. Contacting one author acting expressly as authorised agent for their co-authors is acceptable.
· You will reproduce the following prominently alongside the material:
o the source of the material, including author, article title, title of journal, volume number, issue number (if relevant), page range (or first page if this is the only information available) and date of first publication. This information can be contained in a footnote or reference note; or
o a link back to the article (via DOI); and
o if practical and IN ALL CASES for works published under any of the Creative Commons licences the words "© [insert rightsholder]. Reproduced by permission of IOP Publishing. All rights reserved"
· The material will not, without the express permission of the author(s), be used in any way which, in the opinion of IOP Publishing, could distort or alter the author(s)' original intention(s) and meaning, be prejudicial to the honour or reputation of the author(s) and/or imply endorsement by the author(s) and/or IOP Publishing.
· Payment of £0 is received in full by IOP Publishing prior to use.

If you have any questions, please feel free to contact our Permissions team at permissions@iop.org. I should be grateful if you would acknowledge receipt of this email.

Kind regards,
Gemma

Please note: We do not usually provide signed permission forms as a separate attachment.

Please print this email and provide it to your publisher as proof of permission.

Gemma Alaway
Rights & Permissions Adviser
IOP Publishing
Temple Circus, Temple Way, Bristol
BS1 6HG, UK
Direct line +44 (0)117 930 1146
ioppublishing.org